Virginia Sea Grant Program

Research Division
Virginia Polytechnic Institute and State University
Blacksburg, Virginia 24061

PROPERTIES OF OCEANIC MANGANESE NODULE FIELDS RELEVANT TO A REMOTE ACOUSTICAL SENSING SYSTEM

by

Kenneth David Smith

VPI-SG-81-13

VPI-Aero-123

May 1981

This work is a result of research sponsored by NOAA Office of Sea Grant, Department of Commerce, under Grant No. NA81AA-D-00025 and the Virginia Sea Grant Program through Project No. R/OE-1. The U. S. Government is authorized to produce and distribute reprints for governmental purposes notwithstanding any copyright notation that may appear hereon.

ACKNOWLEDGMENTS

Special thanks go to my committee chairman, Dr. K. Sundkvist, for his help and guidance during the course of this research, and for his many helpful suggestions in preparation of this publication. Thanks are also due to Dr. A. H. Magnuson and Dr. D. Rooney for their suggestions and various contributions to this work.

TABLE OF CONTENTS

LIST OF FIGURES AND TABLES

FIGURE PAGE

TABLE PAGE

LIST OF SYMBOLS

a	nodule radius
$\overline{a^n}$	average of the nth power of the radius
$\bar{a}^n$	nth power of the average radius
b	Rayleigh parameter
C	wave speed
C_L or C_o	longitudinal wave speed
C_T	transverse wave speed
d	distance through nodule specimen
E	modulus of elasticity
$E(r,r_i)$	wave propagation function
$f(R)$	radial distribution function
G	shear modulus of elasticity
$g(s_i,\omega)$	scattering strength function
$\bar{g}$	size averaged scattering strength
$h_n^{(2)}(kr)$	spherical Hankel function
I_o	incident wave intensity
I_s	scattered wave intensity
j_n	spherical Bessel function
k	wavenumber, ω/C
M_w	wet nodule mass
M_d	dry nodule mass
N	total number of nodules
n_i	number of nodules in interval i

n_n	Neumann function
p	total pressure
p_a	incident pressure amplitude
p_I	incident pressure
p_S	scattered pressure
$P_n(\cos\theta)$	Legendre polynomial
$\langle p \rangle$	configurational average of p
$p^i(r_i)$	external pressure field to scatterer i
$Q(\ )$ or $q(\ )$	probability functions
r	vectorial radius
s	scattering parameter
t	time
V	volume
$Y_{m,n}(\theta,\psi)$	spherical harmonic
γ	nodule porosity
$\Gamma(\nu)$	Gamma function
θ,ψ	coordinate angles
ρ_e	elastic material density
ρ_o	fluid medium density
ρ_d	dry nodule density
ρ_w	wet nodule density
ρ_{sm}	solid material density
$\hat{\rho}$	nodule number density
σ	scattering cross section
ω	incident wave frequency

Chapter I

INTRODUCTION

The mining of manganese nodules from the ocean floors has recently become economically competitive with land mining operations because of newly developed deep sea mining techniques and equipment. Principal metals which may be recovered from the nodules are copper, cobalt, and nickel (though several other desirable elements are present and recoverable in smaller amounts).

Vast areas of the ocean floors must be surveyed and cataloged with the goal of isolating potential mining sites. These sites must contain a sufficient abundance of nodules for economic gain, and the nodules must conform to certain size limitations imposed by the type of mining equipment used. For areas in which these goals are met, further evaluation of the site as a mining resource may then be required by way of grab samples or box cores for determining nodule assay (mineral content).

An ongoing NOAA Sea Grant project begun in March of 1980 at VPI&SU in Blacksburg, Virginia is concerned with speeding up, and therefore lowering the cost of, the initial prospecting operation (which at present is painfully slow and expensive), through the development of a remote acoustic sensing system. This thesis results from the examination of acoustical properties of manganese nodules and some physical characteristics of nodule fields (size distributions and spatial configurations) performed in support of the Sea Grant project. Specifically, longitudinal and transverse wave speeds were measured through typical Pacific and Atlantic Ocean manganese nodules. A function representing the distributions of nodule floor plane, cross-sectional areas in several nodule fields was determined. Transforms were developed from that areal distribution function to relate the averages of radii to various powers. Spatial distributions were treated only superficially and several generalized observations noted.

Presently, in situ inspection is the only way to determine if a particular bottom site contains a sufficiently high areal weight density (weight of nodules per unit bottom area) and meets the size limitations necessary for mining operations. A deep tow sled must be lowered two to three miles to the ocean floor carrying equipment that can examine the ocean bed. Such equipment might include lights and cameras (McFarland 1980) for a photographic recording or side-scan sonar (Speiss 1980) for an acoustic image recording. Lights and cameras must be close to the bottom (within about 10 meters) in order to allow illumination of the bottom and resolution of individual nodule outlines. Side-scan sonar utilizes ultrasonic frequencies (100kHz and higher) to obtain detailed pictures of nodule sites with high resolution. However, over large distances severe attenuation of such high frequency signals becomes a limiting deployment factor, requiring that the ultrasonic source and receiver be located close to the ocean bottom also (within 50 meters or so).

The survey ship must tow the equipment sled at a very slow speed to ensure that the sled remains at a stable attitude and height above the ocean floor. The magnitude of this problem is more readily appreciated when one considers the enormous lengths of cable required to reach from ship to sled. Other factors contributing to the currently slow surveying problem are the time consuming equipment lowering from surface to bottom (and the subsequent raising), and the inaccessibility of the equipment for possible maintenance or quick-fix procedures.

The mining companies can usually determine by visual inspection of the photographic or acoustic images whether or not a nodule site contains sufficient areal weight density. In some cases of marginal abundance, photographic analysis may be required to determine more exactly the areal weight density, since the mining companies will certainly have some cut-off limit in mind for a profit margin. The limit would vary with current ore market prices but Frazer (1977) has indicated an average weight density of at least $10 kg/m^2$, dependent upon the local nodule assay. Photographic analysis may be quite a time-consuming procedure depending upon the degree of accuracy required. McFarland (1980) has presented more information on photographic analysis methods and some recently proposed improvements.

The undesirable aspects associated with present prospecting techniques are summarized below:

1) Excessively low surveying (towing) speeds.
2) Time consuming equipment drops.
3) Inaccessible equipment packages.
4) Possibly time-consuming photo analysis for marginal areal weight density sites.

One approach to remedy these problems attempts to correlate nodule abundance to the bottom transparent layer thickness (bottom sedimentary layer thickness) (Mizuno 1976). This idea arose from weak correlations between the two variables noticed in seismic reflection records. More recently however, negative results have been indicated in high nodule abundance areas (Moritani 1979). The correlation does not appear to be consistent enough or quantitative enough to adopt as a surveying technique.

Indeed, prospecting processes available at present are very time consuming and costly. An alternative prospecting method is therefore desirable. The remote acoustic sensing system mentioned above is outlined in a Sea Grant proposal entitled Acoustic Sounding for Manganese Nodules (Magnuson and Sundkvist 1979). 'Remote' here implies a system operating from on or just beneath the water surface, eliminating the two to three mile equipment drop to the ocean floor. The system hardware, mounted on a 'fish' towed behind a surveying vessel, would allow much higher surveying speeds (Figure 1). The system would send an acoustic pulse down to the ocean floor and receive the return signal as is commonly done in depth sounding work. Unlike depth sounding however, the return signal's pulse shape and variation with output frequency must be analyzed in order to determine what has been encountered by the incident signal at the ocean floor. Specifically, are nodules present in the insonified area? If so, what is the areal weight density and the average nodule size?

The second chapter examines the proposal's operational aspects which allow for the remote sensing for manganese nodules. It is sufficient to say here that it is the frequency dependence of the scattered return signal from the nodules that is the key to the success of the project. To be able to infer information about the presence of nodules from this returned signal, one must be equipped with an extensive knowledge of the interaction of the incident acoustic wave with the nodules on the ocean bottom. The analytical tools required to interpret the return signals have been (and are being) developed by other investigators, and the major points of their acoustical scattering analyses are presented in Chapter III.

The basic components of the physical system are the nodules, the sediment on which they rest, and the acoustic plane wave which is directed at both of the former. It is assumed that there is no acoustic interaction between the sediment and the nodules (see Figures 2 & 3). That is, the total scattered field equals the scattered field from the nodules plus the reflected field from the sediment (if any). (The sediment-nodule interaction may be taken into account at a later date but its consideration is not warranted at this initial level of analysis.) Reflection from a flat plane is rather elementary: the reflected acoustic intensity is proportional to the incident intensity by a reflection coefficient which is independent of frequency. In fact, the acoustically transparent sediment layer on which the nodules are typically found will give only a very weak response. The difficulty arises in relating the scattered field to nodule size and abundance.

Chapter III begins with the analysis of an individual nodule insonified by a plane wave. The general problem is posed as an elastic sphere surrounded by liquid and solutions are obtained in terms of acoustical pressures. In particular, the scattered wave pressure is sought as a function of incident pressure amplitude and frequency, nodule radius, and nodule density and wave speeds. A measure of the scattering capability of a nodule is presented by way of the scattering cross section function. This analysis requires a quantitative knowledge of the acoustical velocities in manganese nodules (both compressional and shear wave speeds) and of the wet density of manganese nodules. Measurement of the wave speeds (not now found in the literature) is described in Chapter IV. Chemical and physical properties of manganese nodules are found in various sources (Gladsby 1977, Greenslate 1977).

The response of many nodules insonified together is examined next. We may either assume that each nodule of some large group acts independently (and the total response is the summation of each individual nodule response to the incident wave), or that there is an acoustic interaction between the nodules (in which case the total response is not simply the summation of individual nodule responses). The former case is a valid approximation of sparsely distributed fields where the nodules are separated by many average nodule diameters. However, for closely packed nodule distributions, the second, more general case for acoustic interaction must be considered. Both cases are studied.

The multiple scattering analyses require knowledge of the nodule field size distributions. 'Size distribution' can mean any of the group of distributions actually sought - the radius, radius squared, and radius cubed distributions (in general, the radius to any power distribution may be required). Size distributions were obtained by studying nodule cross-sectional area distributions of nodule fields from ocean floor photographs. An analysis of size distributions in manganese nodule fields is contained in Chapter V.

For densely packed systems, we must make use of spatial or radial distributions, i.e., a measure of the distances separating nodules. Consideration of the spatial distribution accounts for the effect on the scattered field from a nodule because of the proximity of its neighbors. Spatial distributions are only briefly examined in Chapter VI. Utilization of information obtained from them is limited in this report, because the theory has not been sufficiently developed at this time.

The physical characteristics of nodules and nodule fields required for use in the theoretical analyses and of major concern to this thesis then, are:

1) Longitudinal (compressional) and transverse (shear) wave speeds in the nodules (required at all levels of analysis).

2) Area distribution functions (required for the multiple scattering analyses).

3) Spatial distribution functions (required for the multiple scattering analysis of densely packed nodule fields).

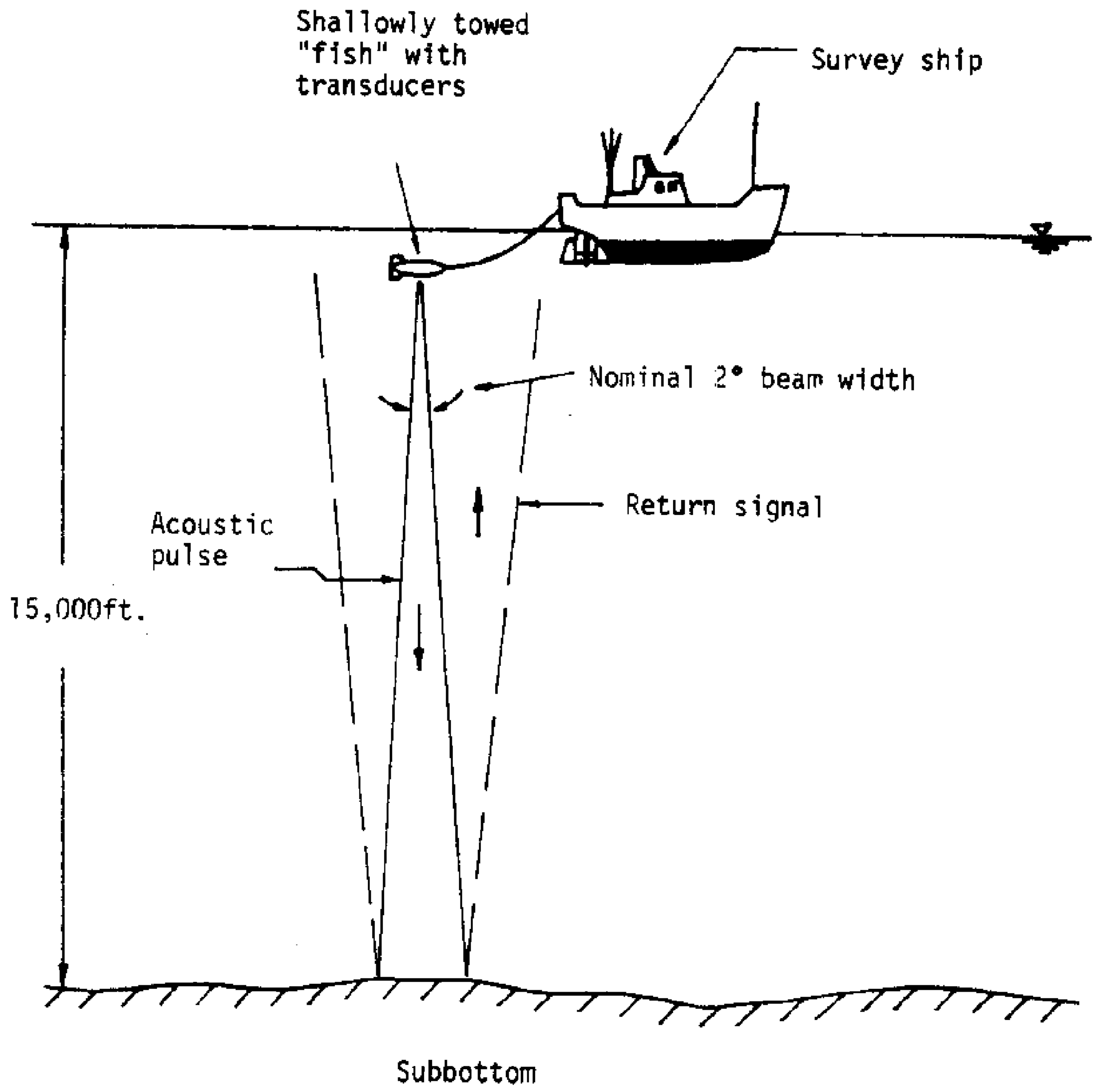

Figure 1. Proposed Prospecting System

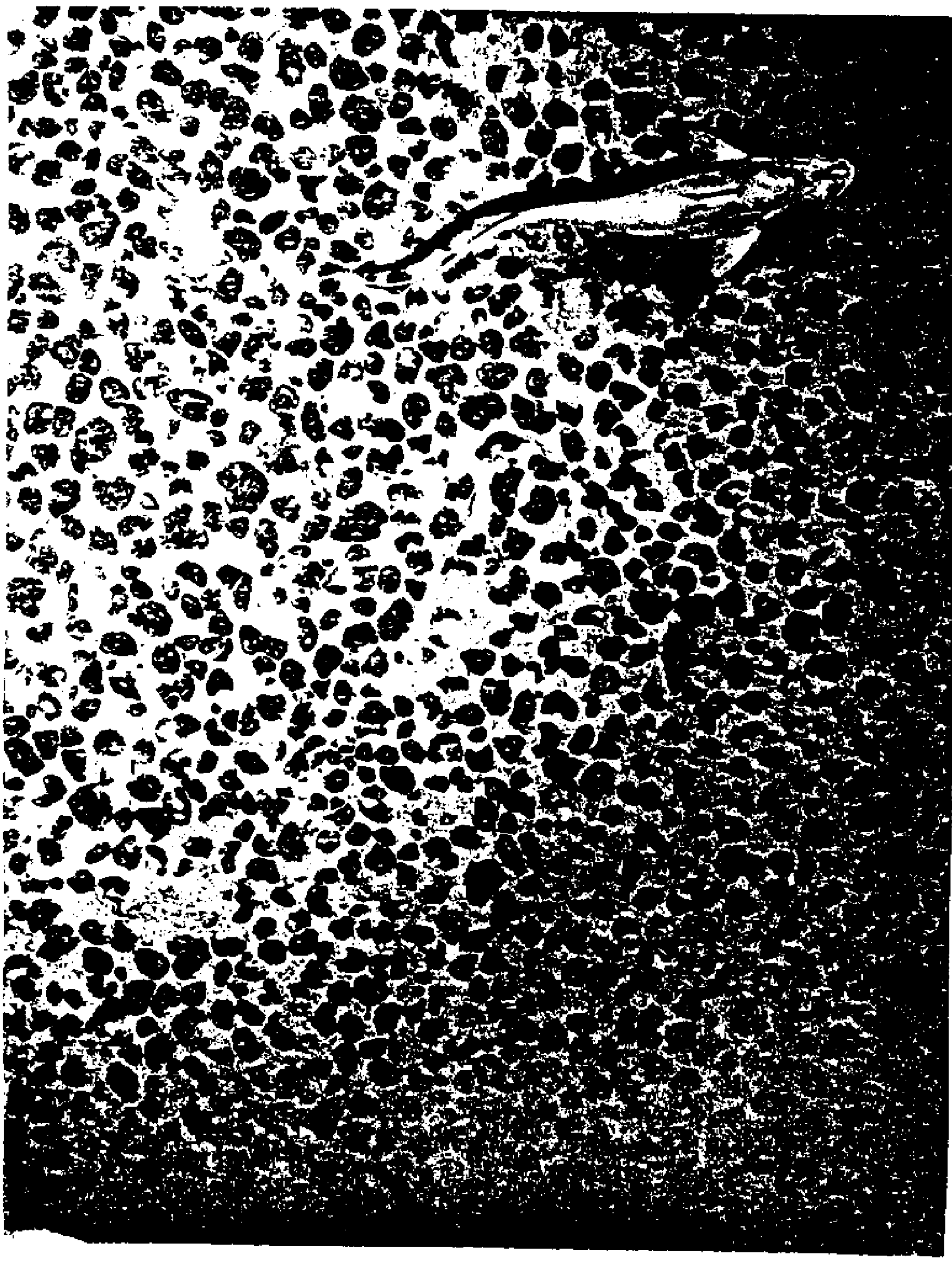

Figure 2. **Photograph of Typical Manganese Nodule Field in Pacific**
(Courtesy of Deepsea Ventures, Inc.)

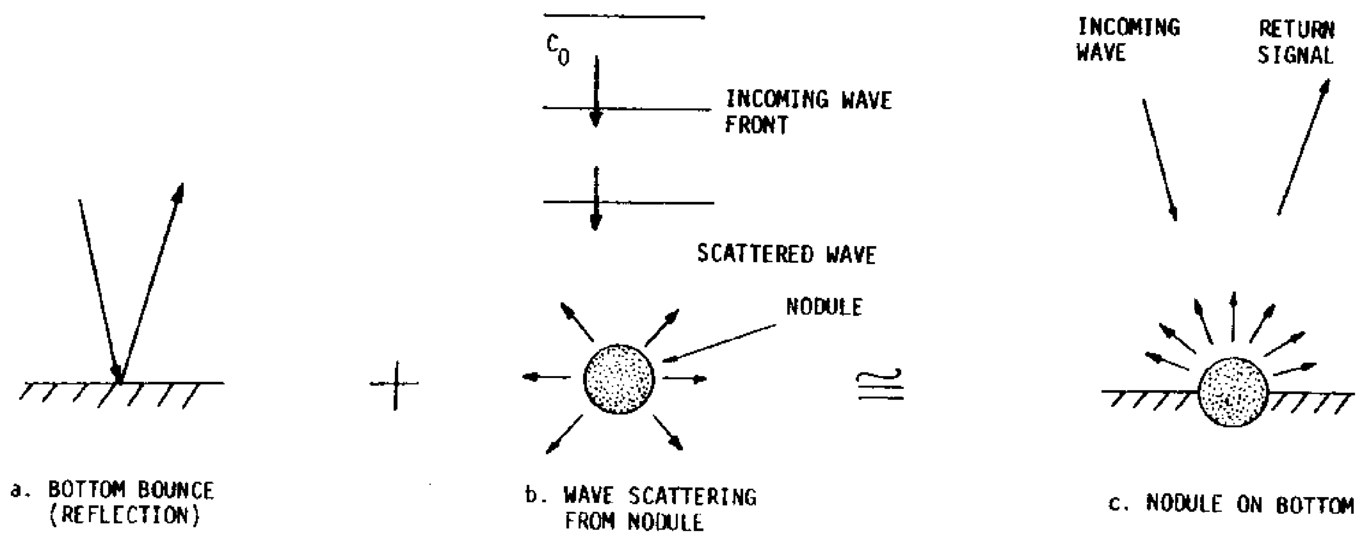

Figure 3. Simplified Nodule - Sediment Interaction

Chapter II

BASIS OF THE SEA GRANT PROPOSAL

Deepsea Ventures, Inc. (Gloucester Point, Va.) has verbally reported on the results of using their FADS (Finite Amplitude Depth Sounding) system with a CESP (Correlation Echo Sounding Processor) unit, both of which are products of Raytheon, over ocean floors with and without manganese nodules. Soft ocean bottoms containing manganese nodules caused an increase in the return signal strength compared to soft bottoms without nodules. But they were unable to distinguish between a soft ocean bottom with nodules and a hard ocean bottom without nodules, both of which returned increased signal strengths. If, however, an analysis of the frequency dependence of the return signal had been performed, the difference in the signals might well have been determined. (The above by private communication with W. Siapno, Director of Marine Science, Deepsea Ventures Inc., in Gloucester Point, Va.)

In general, the acoustic response to an incident plane wave on a field of scatterers will approach the shape of one of the curves in Figure 4. The strength of the return (for a given average scatterer radius a) is indicated by position along the ordinate (vertical) axis while the incoming acoustic signal frequency ω varies along the abscissa (horizontal) axis. The acoustic signature of some scatterer may be plotted on these axes. For Rayleigh scattering (incoming wavelength large compared to nodule radius), the response exhibits a frequency to the fourth power dependence. For geometrical scattering (incoming wavelength small compared to nodule radius), the response is more or less frequency independent. We will term the frequency where the response changes from Rayleigh scattering to geometrical scattering as the break frequency. The result of increasing the average nodule diameter in the field, but maintaining a constant nodule concentration, shifts the curve and the break point to the left (Figure 4a). The result of increasing the nodule concentration for a fixed average diameter is an elevation of the signature (Figure 4b).

These relations are the basis of this Sea Grant project. The steps for determining nodule site information from the operational point of view might be:

1) Locate rounded scatterers on the ocean bottom by the low frequency dependence.

2) Determine average scatterer diameter by the break frequency.

3) Determine the number density (number per unit area) of the nodules by the strength of signal or break level.

4) Calculate areal weight density from number density and size averaged individual scattering cross sections.

Figure 4 indicates the general shape expected for acoustic signature of manganese nodule deposits. Actually, the region between Rayleigh scattering and geometrical scattering is a resonance region, and the transition is not at all as smooth as indicated in Figure 4. Figure 5 more accurately shows the onset of the resonance region. These plots were derived analytically by Ma (1981) for an elastic sphere (approximating a manganese nodule) and for a fluid sphere (for comparison). The scatter strength dependence on the radius in the resonance region is not simple (as in the Rayleigh range).

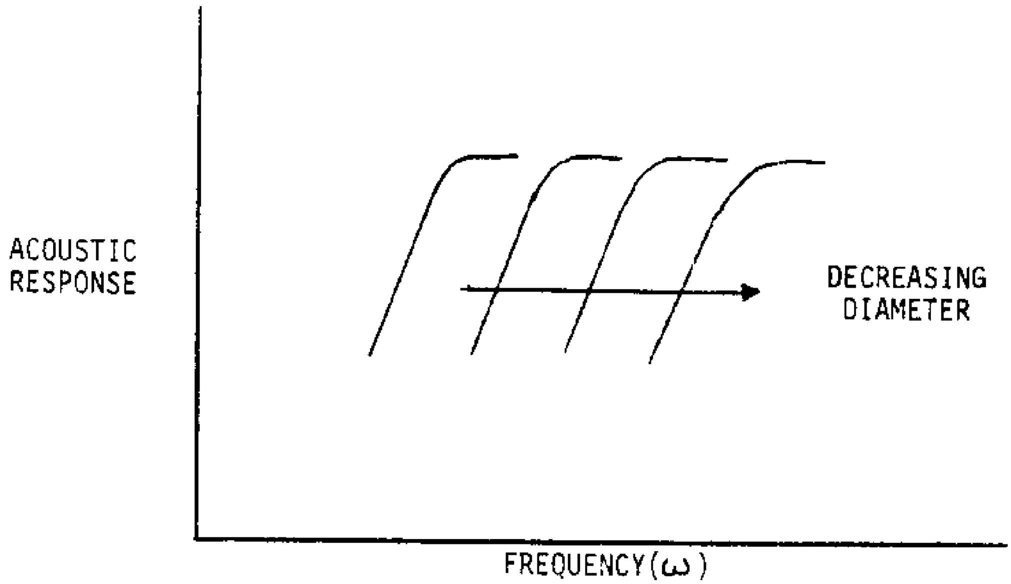

a. VARIATION WITH MEAN NODULE DIAMETER FOR DEPOSITS WITH SAME NUMBER DENSITY

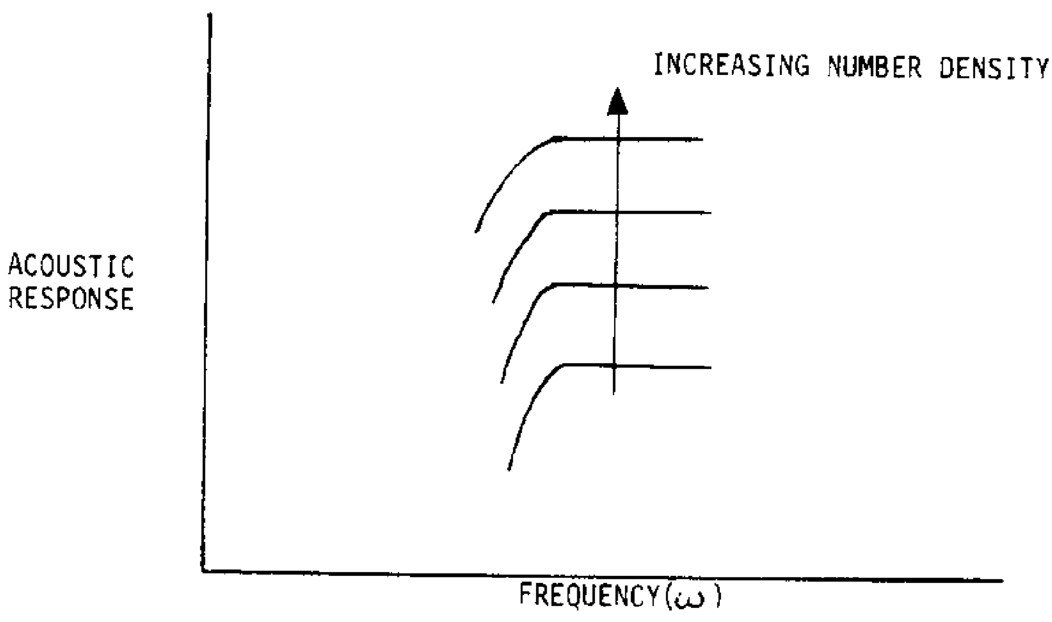

b. VARIATION WITH NUMBER DENSITY FOR FIXED MEAN DIAMETER OF NODULES

Figure 4. Acoustic Signature Trends for Nodule Deposits

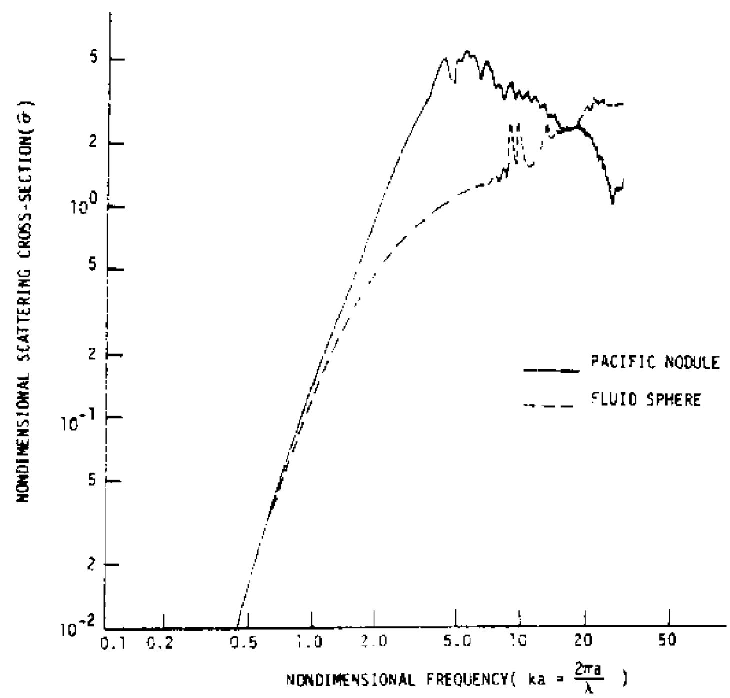

Figure 5. Scattering Strength vs. Frequency for Single Nodule

Chapter III

ACOUSTIC SCATTERING FROM MANGANESE NODULES

Throughout the analytical work outlined in this chapter the nodules are approximated as elastic spheres. The spherical assumption is better for Atlantic nodules but not as good for Pacific nodules which are somewhat flattened in the vertical direction. Pacific nodules may at best be described as oblate spheroids. It may be found in further investigations that a shape correction factor is required, but no consideration is given to a correction factor in this 'first look' study.

In general, an elastic medium supports one compressional wave speed of propagation and one shear wave speed of propagation in response to acoustical perturbations. The nodules are actually porous spheres for which theory predicts two compressional wave speeds and one shear wave speed to exist. During tests on the nodules, only one compressional wave speed was observed, so the elastic approximation is used.

Scattering analysis applications were investigated by other researchers working on this Sea Grant project at VPI&SU. The reader is referred to Ma (1981), and to Magnuson <u>et al.</u> (1981) for more detailed presentations of the following analyses.

The response of a single elastic scatterer to an incident plane wave is considered first. A scattering cross section is defined and an expression obtained for the low frequency case where ka<<1. Experimentally determined numerical values are substituted into the scattering cross section expression. The multiple scattering problem is then addressed (considering both sparsely packed and densely packed nodule fields). Lastly, a simplified form of the scattering solution is examined to show the application of size distributions and wave speed measurements.

3.1 SINGLE SCATTERER ANALYSIS

The total pressure field for an individual scatterer is made up of the incident plane wave pressure p_I and the outgoing scattered wave pressure p_s. Writing expressions for these pressures requires knowledge of the general solution to the linearized acoustic wave equation in spherical coordinates and consideration of the boundary conditions.

The linearized acoustic wave equation is

$$(\nabla^2 + k^2)\ p = 0 \qquad (1)$$

where p is the perturbation pressure and k is the wavenumber ω/C (frequency divided by wave speed). The general solution to equation (1) is

$$p = \sum_{n,m=0}^{\infty} P_{m,n} Y_{m,n} (\theta,\psi) \begin{bmatrix} j_n(kr) \\ \\ n_n(kr) \end{bmatrix} \tag{2}$$

where $Y_{m,n}(\theta,\psi)$ is a spherical harmonic, $j_n(kr)$ and $n_n(kr)$ are a spherical Bessel function and a Neumann function respectively, and θ, ψ, and r are indicated in Figure 6. There is no ψ dependence in our problem because of symmetry.

Equation (2) may be applied to the incident plane wave, which is actually given by

$$p_I = p_a e^{ikr\cos\theta} \tag{3}$$

yielding the following simplified result:

$$p_I = p_a \sum_{n=o}^{\infty} (2n+1) i^n \, j_n(kr) p_n(\cos\theta) \tag{4}$$

where p_a is the incident pressure amplitude and $p_n(\cos\theta)$ is a Legendre polynomial.

Application of equation (2) to the outgoing scattered wave gives

$$p_s = \sum_{n=0}^{\infty} B_n \, h_n^{(2)}(kr) \, p_n(\cos\theta) \tag{5}$$

where $h_n^{(2)}(kr)$ is a spherical Hankel function, and B_n must be evaluated by the boundary conditions.

The boundary conditions require an acoustical wave match at the interface between the scatterer's interior compressional and shear elastic wave solutions and the exterior compressional wave of the surrounding fluid medium. Physically, the match is achieved by applying continuity of stresses and continuity of normal and tangential displacements at the interface. It is found by Ma (1981) that

$$B_n = \frac{1}{1+iC_n} \, P_a(2n+1)i^n \tag{6}$$

where

$$C_n = \frac{n_{n1} D_n - g \dfrac{x_1}{x_3{}^2} n'_{n1} E_n}{-j_{n1} D_n + g \dfrac{x_1}{x_3{}^2} j'_{n1} E_n} \tag{7}$$

$$D_n = 2n(n+1)\left(1 - \frac{j_{n2}}{x_2 j'_{n2}}\right) - \frac{x_3{}^2 j''_{n3}}{j_{n3}} - (n^2+n-2)$$

$$E_n = 4n(n+1)\left(1 - \frac{j_{n2}}{x_2 j'_{n2}}\right)\left(1 - \frac{x_3 j'_{n3}}{j_{n3}}\right)$$

$$-2x_2 \left\{ \left(\frac{x_3{}^2 j''_{n3}}{j_{n3}} + n^2 n-2\right) \left[\left(\frac{1}{2h_3{}^2} - 1\right) \frac{j_{n2}}{j'_{n2}} - \frac{j''_{n2}}{j'_{n2}} \right] \right\}$$

$x_1 = ka$

$x_2 = k_L a$

$x_3 = k_T a$

$g = \rho_e/\rho_o$

$h_3 = C_T/C_L$

The subscripts 1, 2, or 3 on the spherical Bessel and Neuman functions refer to the argument of the function so that j_{ni} denotes $j_n(x_i)$ and similarly for n_{ni}. The superscript ' refers to the derivative with respect to the argument. k is the surrounding fluid wave number ω/C_o and k_L and k_T are the scatterer's longitudinal and transverse wave numbers, ω/C_L and ω/C_T respectively. The surrounding medium density is given by ρ_o and the elastic medium density by ρ_e.

The scattered pressure p_s may then be written as

$$p_s = \sum_{n=0}^{\infty} \frac{1}{1+iC_n} p_a (2n+1) i^n h_n^{(2)}(kr) p_n(\cos\theta) \qquad (8)$$

For the far field solution (kr>>1), $h_n^{(2)}$ (kr) may be replaced as follows:

$$h_n^{(2)}(kr) = \frac{1}{kr} e^{-i[kr-(n+1)\pi/2]} \qquad (9)$$

We may then write the scattered pressure as

$$p_s = \left\{ \sum_{n=0}^{\infty} \frac{1}{1+iC_n} (2n+1) i^n p_n(\cos\theta) e^{i(n+1)\pi/2} \right\} p_a \frac{e^{-ikr}}{kr} \qquad (10)$$

where e^{-ikr} is the scattering phase. This result is obtained in a more rigorous manner by Ma (1981).

We see that the scatter pressure from one nodule may be written in terms of an infinite sum;

$$p_s = \sum p_{si} \tag{11}$$

At present, there is primary interest in the Rayleigh scattering region (that is, where ka, wave number times nodule radius, is small) for there is a simple frequency dependence expected here. For ka<<1,

$$p_s = (p_s)_0 + (p_s)_1 + \text{higher order terms} \tag{12}$$

The first two terms on the right hand side of equation (12) are respectively, the monopole and the dipole terms and they correspond to n=0 and n=1 in equation (10). Upon evaluating C_n for several values of n, it is found that the monopole and dipole terms both are of order $a(ka)^2$ while the 'higher order terms' are of order $a(ka)^4$ and may be neglected.

The scatter pressure from an individual scatterer in the Rayleigh region (ka<<1) is found to be (Ma 1981),

$$p_s = a(ka)^2 \left[\frac{e - \dfrac{1}{1 - {}^4/{}_3 h_3^{\,2}}}{3e} + \cos\theta \, \frac{g-1}{2g+1} \right] p_a \frac{e^{-ikr}}{r} \tag{13}$$

where

$$e = g \, C_L^{\,2} / C_0^{\,2}$$

$$g = \rho_p / \rho_o$$

$$h_3 = C_T / C_L$$

The subscripts T, L, and e refer to the elastic solid, and subscript o refers to the surrounding fluid medium. The first term in brackets in equation (13) is the monopole term and the second term is the dipole term. The dipole term is a function of the scattering angle θ. Positive θ is measured from the line connecting the incident pressure wave source with the scatterer to the line connecting the scatterer with the point at which p_s is sought.

The scattering cross section σ is a measure of the scattering capability of an object. It is defined as the ratio of the scattered intensity to the incident intensity and measured at some distance r from the scattering source point;

$$\sigma = \frac{I_s}{I_o} r^2 \tag{14}$$

The intensities I_s and I_o are related to the pressures p_s and p_a by

$$I_o = \frac{p_a^2}{\rho_o C_o} \tag{15a}$$

$$I_s = \frac{p_s^2}{\rho_o C_o} \tag{15b}$$

Thus, for r equal to 1 meter (the commonly used point of reference for σ),

$$\sigma = |p_s/p_a|^2 \tag{16}$$

and has the dimensions of an area.

The scattering cross section for a single elastic sphere with ka<<1 is

$$\sigma = a^2(ka)^4\left[\frac{e - \frac{1}{1-{}^4/{}_3h_3^{\,2}}}{3e} + \cos\theta\,\frac{g-1}{2g+1}\right]^2 \qquad (17)$$

This expression may be compared with an expression of the scattering cross section for a single fluid sphere with ka<<1, attributed to Rayleigh himself (Clay and Medwin 1977), given by

$$\sigma = a^2(ka)^4\left[\frac{e-1}{3e} + \cos\theta\,\frac{g-1}{2g+1}\right]^2 \qquad (18)$$

where the first term in brackets is the monopole term and the second term is the dipole term. Equations (17) and (18) are of very similar form. The only difference between the elastic and fluid expressions is in the monopole term, and this difference is due to shear wave effects in the elastic sphere (the fluid sphere propagates a compressional wave only).

If we take elastic sphere equation (17) and let the shear wave speed go to zero (h_3 goes to zero, leaving only the compressional wave as in a fluid sphere), then the additional elastic term in the monopole goes to one:

$$\frac{1}{1-{}^4/{}_3h_3^{\,2}} \longrightarrow 1 \qquad (19)$$

The result is equation (18), the fluid sphere scattering cross section for $ka<<1$.

Results obtained in Chapter IV can be used to evaluate most of the terms in equation (13). Average Pacific nodule densities and wave speeds are used. Let

$$g = 1.94$$

$$h_3 = 0.90$$

$$e = 4.76$$

and the scattering cross section for an elastic nodule in the Rayleigh range becomes

$$\sigma = \left\{a^3k^2\left[(1.21) + \cos\theta\,(.540)\right]\right\}^2 \tag{20a}$$

For convenience, we define $L(\theta)$ such that

$$\sigma = \left\{a^3k^2L(\theta)\right\}^2 \tag{20b}$$

3.2 MULTIPLE SCATTERING ANALYSIS

The multiple scattering analysis uses a self consistent field approach (Foldy 1945) in examining the total pressure field occurring in the presence of N scatterers. The total pressure field $p(r)$ equals the incident acoustical pressure field $p_I(r)$ plus the sum of all the scattered pressure fields from each of the N scatterers;

$$p(r) = p_I(r) + \sum_{i=1}^{N} p_{si}(r) \tag{21}$$

The origin of the coordinate system for this case is fixed on a plane of scatterers (Figure 7). The ith scatterer is located at r_i (where $z_i=0$) and this scatterer emits a scattered pressure field given by

$$p_{si}(r) = g(s_i, \omega)\, E(r,r_i)\, p^i(r_i) \qquad (22)$$

where $g(s_i,\omega)$ is a function of the incident frequency ω and a scattering parameter s (which may, in general, be related to the nodule radius and nodule acoustical properties), and $E(r,r_i)$ is a Greens function that characterizes propagation through the medium between the scatterer at r_i and the field location at r given by

$$E(r,r_i) = \frac{e^{ik|r-r_i|}}{|r-r_i|}$$

Lastly, $p_i(r_i)$ is the total pressure field external to the ith scatterer.

The external field may be defined

$$p^i(r_i) = p(r) - p_{si}(r) \qquad (23)$$

or in words, the external field to scatterer i equals every pressure contribution (incident and scattered) to the total field (p(r)) around i minus its own scattered pressure field ($p_{si}(r)$). Herein lies the 'self consistency' of this approach. The external field has been defined in terms of the quantity initially being sought - the total pressure field p(r).

Combining equations (21) and (22), we have

$$p(r) = p_I(r) + \sum_{i=1}^{N} g(s_i,\ \omega)\ E(r,r_i)\ p^i(r_i) \qquad (24)$$

and combining equations (21), (22), and (23), we can write

$$p^i(r_i) = p_I(r) = \sum_{\substack{j=1 \\ j\neq i}}^{N-1} g(s_j,\omega)\ E(r,r_j)\ p^j(r_j) \qquad (25)$$

where the same external field term appears on both sides of the equation, and a similar equation can be written for the external field of the jth nodule. Equations (24) and (25) may be solved for some particular configuration of scatterers, but we are interested in quantities that are averaged over all possible configurations of scatterers since for the general application of this theory to nodule fields, the configuration will be unknown.

The configurational average is defined as

$$\langle p\rangle = \int_{2N} pQ(r_1 r_2 .. r_N, s_1 s_2 .. s_N) dr_1 dr_2 .. dr_N ds_1 ds_2 .. ds_N \qquad (26a)$$

where

$$Q(r_1 r_2 .. r_N,\ s_1 s_2 .. s_N) dr_1 dr_2 .. dr_N ds_1 ds_2 .. ds_N \qquad (26b)$$

is the probability of a particular configuration occurring with scatterer locations between r_i and dr_i and corresponding scattering parameters between s_i and ds_i.

For the ith scatterer's position and scattering parameter fixed, the conditional configurational average is expressed as

$$\langle p \rangle_i = \int_{2N-1} pQ(r_1 r_2 .. r_N, s_1 s_2 .. s_N / r_i, s_i) dr_1 dr_2 .. dr_{N-1} ds_1 ds_2 .. ds_{N-1} \tag{27}$$

Using conditional probabilities, we can rewrite the probability density function found in equations (26) as

$$Q(r_1 r_2 .. r_N, s_1 s_2 .. s_N) = Q_i(r_i, s_i) Q(r_1 r_2 .. r_N, s_1 s_2 .. s_N / r_i, s_i) \tag{28a}$$

or as

$$Q(r_1 r_2 .. r_N, s_1 s_2 .. s_N) = Q_{ij}(r_i r_j, s_i s_j) Q(r_1 r_2 .. r_N, s_1 s_2 .. s_N / r_i r_j, s_i s_j) \tag{28b}$$

where the dividing slash in the conditional probabilities means the indicated parameters are fixed.

Taking the configurational average of equation (24) and applying equation (28a) to the resulting probability density, we get equation (29a) shown below. The ith conditional probability of equation (28a) is contained in the external pressure field term $\langle p^i(r_i) \rangle_i$. Taking the conditional configurational average of equation (25) (for the external pressure field average), and expressing the ith conditional probability found in equation (28a) in terms of equation (28b), we get equation (29b) where the external pressure field average $\langle p^j(r_j) \rangle_{ij}$ contains the ijth conditional probability found in equation (28b).

Reapplying the configurational average to equation (25) for the external pressure field of each subsequent nodule, a series of N coupled integral equations results. This series of equations, known as the Poldy-Lax hierarchy, is given as follows;

$$\langle p(r)\rangle = p_I(r) + \sum_{i=1}^{N}\int dr_i ds_i Q_i(r_i,s_i)g(s_i,\omega)E(r,r_i)\langle p^i(r_i)\rangle_i \qquad (29a)$$

$$\langle p^i(r)\rangle_i = p_I(r) + \sum_{j\neq i}^{N-1}\int dr_j ds_j \; \frac{Q_{ij}(r_i r_j,s_i s_j)}{Q_i(r_i,s_i)} \; g(s_j,\omega)E(r,r_j)\langle p^j(r_j)\rangle_{ij} \qquad (29b)$$

$$\langle p^j(r)\rangle_{ij} = p_I(r) + \sum_{k\neq j}^{N-1}\int dr_k ds_k \frac{Q_{ijk}(r_i r_j r_k,s_i s_j s_k)}{Q_{ij}(r_i r_j,s_i s_j)} \; g(s_k,\omega)E(r,r_k)\langle p^k(r_k)\rangle_{ijk} \qquad (29c)$$

etc.

Successive equations in the hierarchy use higher order statistics from the scatterer configuration as implied by the increasing explicit conditional probabilities that occur in the external field terms.

The summation from 1 to N in equation (29a) simply produces a multiplier of N into the integrand. The scattering parameter (s_i) integration is examined separately from the radial (r_i) integration over the bottom area. We may define

$$G(r_i) = \int dr_i N Q_i(r_i, s_i) g(s_i, \omega) \qquad (30)$$

Acoustical properties are assumed to be independent of nodule size. Using average acoustical properties, the scattering parameter s may be considered to depend on the nodule size only. The probability function $q_i(r_i, s_i)$ is reduced to the form

$$Q_i(r_i, s_i) = \beta(r_i)\ \alpha(s_i) \qquad (31)$$

for independent size probability distribution $\alpha(s_i)$ and locational probability distribution (expected to be valid except in the case of very densely packed systems for which coupling must be considered - Bong (1980)). The random locational or radial probability distribution $\beta(r_i)$ is given by

$$\beta(r_i) = \hat{\delta}/N$$

and $\hat{\delta}$ is the number density (number of nodules per unit area) of scatterers in the field.

So we see in equation (29) that the size distribution $\alpha(s_i)$ is required for the configurational average (assuming average material properties). A major part of this report is concerned with developing this function from photographic data (see Size Distributions in Manganese Nodule Fields). We also find in equation (31) that $g(s_i, \omega)$ turns out to be the square root of the scattering cross section $\sqrt{\sigma}$. An expression for σ is given in the Single Scattering Analysis, equation (17).

We may now write

$$G(r_i) = N\beta(r_i)\int ds_i \alpha(s_i) g(s_i,\omega) \qquad (32a)$$

$$= N\,\hat{\rho}/N\,\overline{g}$$

$$= \hat{\rho}\overline{g} \qquad (32b)$$

where

$$\overline{g} = \int ds_i \alpha(s_i) g(s_i,\omega) \qquad (33)$$

and the overbar denotes size averaged quantities. It is noted once again that we have assumed average acoustical properties for the field. Equation (29a) becomes

$$\langle p(r)\rangle = p_I(r) + \int dr_i \hat{\rho}\,\overline{g} E(r,r_i)\langle p^i(r_i)\rangle_i \qquad (34a)$$

Applying a similar procedure to (29b), it is found that

$$\langle p^i(r_i)\rangle_i = p_I(r_i) + \int dr_j\ \hat{\rho}\overline{g}\ f(R)E(r_i,r_j)\langle p^j(r_j)\rangle_{ij} \qquad (34b)$$

where $R = |r_i - r_j|$ and f(R) is a pair correlated radial distribution function which gives information about the locational relationships between adjacent nodules. Radial distributions are examined in another portion of this report although not treated in an in depth manner (see Chapter VI).

For equation (29b), we define

$$G(r_j|r_i) = \int ds_j N \frac{Q_{ij}(r_i r_j, s_i s_j)}{Q_i(r_i, s_i)}\, g(s_j,\omega) \qquad (35)$$

and we can write

$$\frac{Q_{ij}(r_i r_j, s_i s_j)}{Q_i(r_i, s_i)} = \frac{q_{ij}(r_i r_j)\ \alpha(s_i)\alpha(s_j)}{\beta(r_i)\alpha(s_i)} \tag{36}$$

where the radial probability $q_{ij}(r_i r_j)$ can not be broken down further because the location of scatterer i with respect to scatterer j is not independent (for densely packed systems). They are pair correlated. We define

$$q_{ij} = \hat{\rho}^2/N^2\ f(R) \tag{37}$$

and plugging back into equation (35) we get

$$G(r_j|r_i) = \int ds_j N\hat{\rho}/N\ f(R)\alpha(s_j)g(s_j,\omega) \tag{38}$$

By equation (33), we may write

$$G(r_j|r_i) = \hat{\rho} f(R)\ \bar{g} \tag{39}$$

the right hand side of which occurs in equation (34b). The difference between equations (39) and (32) is due to the locational correlation between pairs of nodules which is represented by the radial distribution function f(R).

Only the first two equations of the Foldy-Lax hierarchy, equations (34a) and (34b), have been examined because under the proper circumstances, a closure condition can be introduced so that solving all of the N equations is avoided. Two sets of circumstances with corresponding closure conditions are considered here for manganese nodule fields.

For sparse distributions of scatterers (low number density β), it can be assumed that the configuration of scatterers and the average total field are not significantly affected by the location and scattering of the ith scatterer. The closure condition approximating this circumstance is

$$\langle p^i(r_i)\rangle_i = \langle p(r_i)\rangle \tag{40}$$

and only the first equation of the hierarchy, equation (34a), need be solved. Again, this solution is valid only for sparsely packed nodule fields.

For a densely packed distribution of scatterers (high β), the location of scatterer i will, in general, impose limitations on the location of adjacent scatterers, although the scattering from the ith scatterer still will not affect the average total field significantly. Consideration of pair correlation statistics is possible using the closure condition

$$\langle p^j(r_j)\rangle_{ij} = \langle p^i(r_i)\rangle_i \tag{41}$$

and the hierarchy is truncated after the second equation (34b). This closure condition has been dubbed the quasi crystaline approximation by Lax (1951).

3.3 FURTHER EXAMINATION OF VARIOUS TERMS

Equations (34) define the total pressure field occurring for the multiple scattering of nodules and this total pressure field can be used to determine the acoustic signature of the nodule field. The main focus of this thesis is the examination the variables $\bar{g}$ and $f(R)$ for use in those equations. $\bar{g}$, as written in equation (33), is a function of the square root of the scattering cross section $g(s,\omega)$ (which requires quantified acoustical properties), and of the size distribution $\alpha(s)$.

In general, s can be set equal to a^2 - the nodule's radius squared. From equation (20b) we find, in the Rayleigh region (ka<<1), that

$$g(s,\omega) = \sqrt{\sigma} = a^3k^2L(\theta) \tag{42}$$

where k is constant for a given frequency and $L(\theta)$ is independent of s. In terms of the variable s, equation (42) becomes

$$g(s,\omega) = s^{3/2}k^2L(\theta) \tag{43}$$

For $s = a^2$, $\alpha(s)$ is given by the probability function $q(a^2)$ which is defined in Chapter V by equation (56);

$$\alpha(s) = \frac{s}{b^2}\, e^{\frac{-s^2}{2b^2}} \tag{44}$$

Equation (33) for $\bar{g}$ becomes

$$\bar{g} = k^2 L(\theta) \int ds \, \frac{s}{b^2} \, e^{\frac{-s^2}{2b^2}} \, s^{3/2} \qquad (45)$$

The size average of the probability distribution $\alpha(s)$ is by definition equal to 1 leaving

$$\bar{g} = k^2 L(\theta) \overline{s^{3/2}} \qquad (46)$$

where again the overbar denotes size averaged over the entire field. In terms of the radius - a, we have

$$\bar{g} = k^2 L(\theta) \overline{a^3} \qquad (47)$$

$$\bar{g} = \overline{a^3} k^2 \left[(1.21) + \cos\theta \; (.540) \right] \qquad (48)$$

So it has been shown that the total pressure field is a function of the average cubed radius in the Rayleigh region - very convenient for figuring average volumes. Outside of the Rayleigh region, however, $g(s,\omega)$ is a complicated function of a and $\overline{a^3}$ will not generally fall directly out of the equations. Determining $\overline{a^3}$ (or any $\overline{a^m}$) from whatever averaged function of a that may result from the size averaging of $g(s,\omega)$ is the subject of Size Distributions in Manganese Nodule Fields.

As mentioned previously, $f(R)$ is examined somewhat lightly in Spatial Distributions in Manganese Nodule Fields. For this study, we seek only to verify the existence of certain pair correlated features of the spatial distribution.

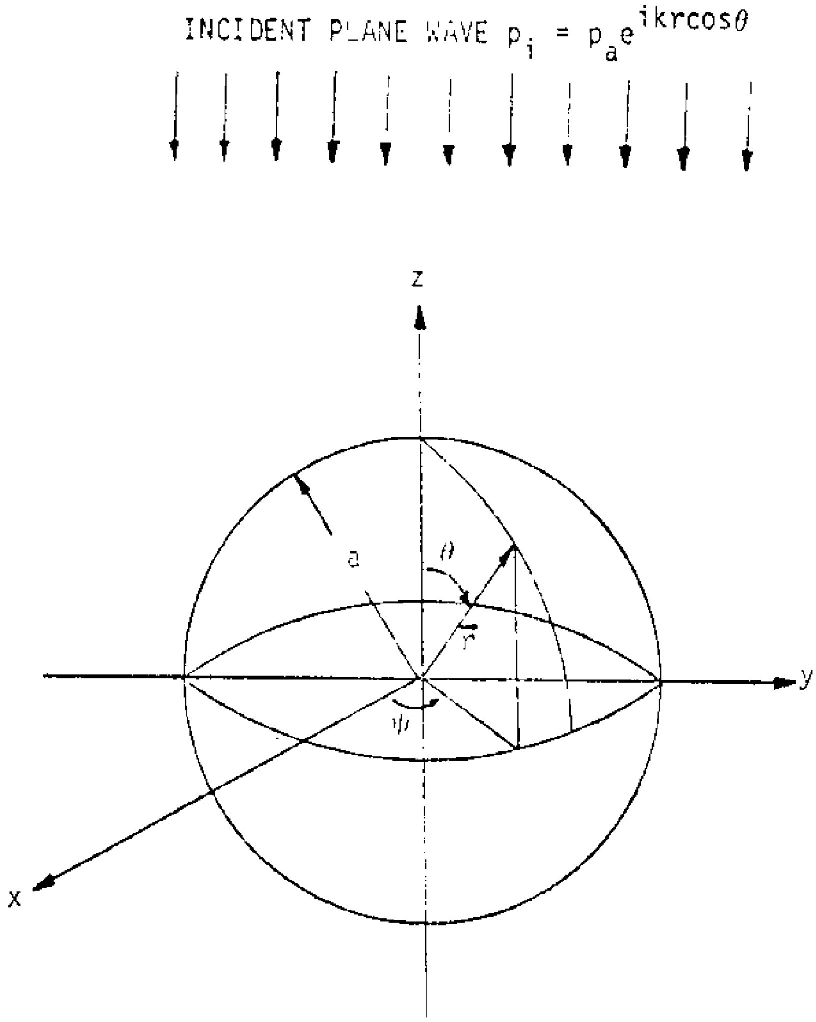

Figure 6. Spherical Coordinate System for Single Scatterer

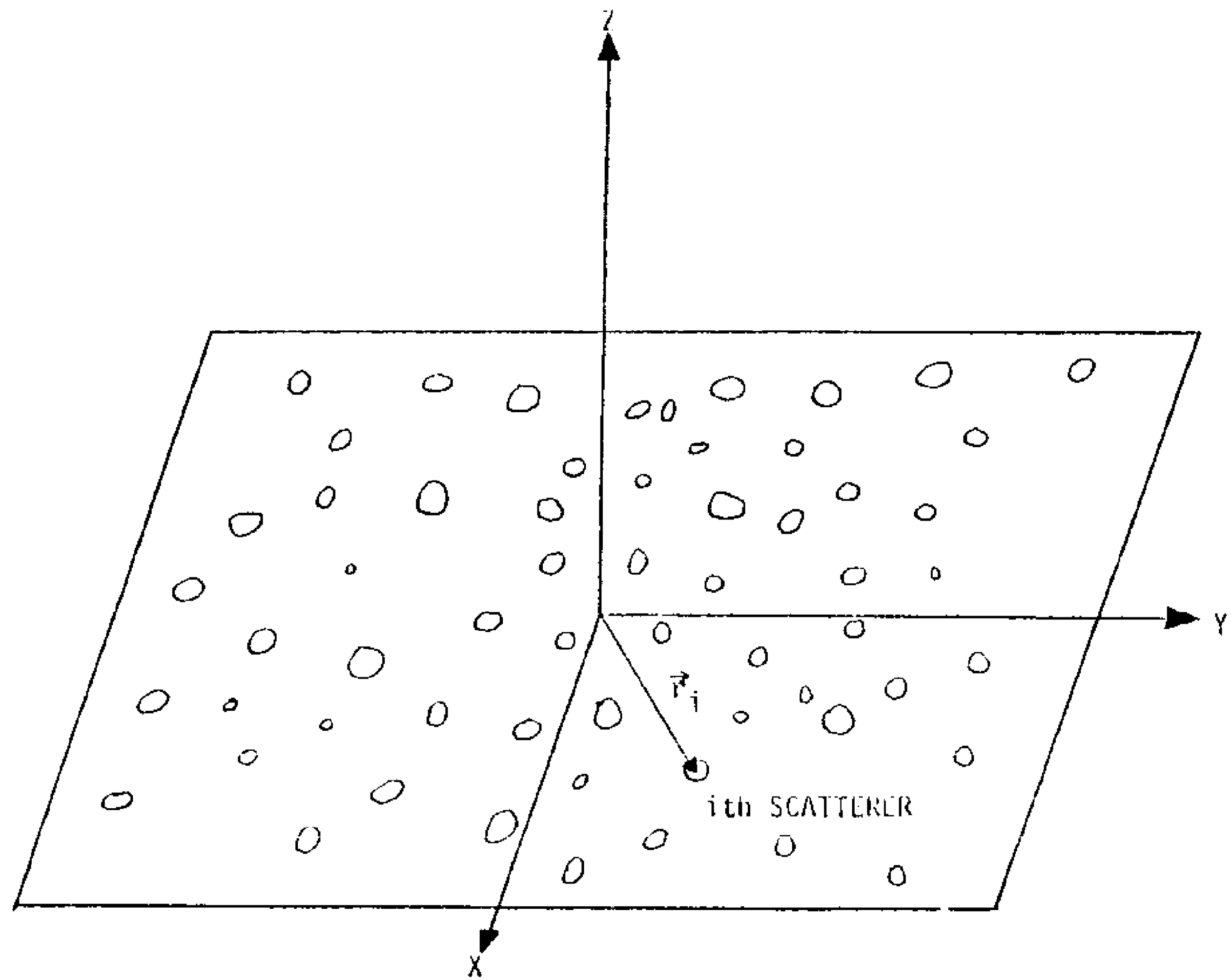

Figure 7. Coordinate System for Multiple Scattering Analysis

Chapter IV

ACOUSTICAL MEASUREMENTS OF MANGANESE NODULES

The acoustical properties of manganese nodules are intrinsic requirements for the application of the scattering analyses to nodule fields. One can choose a specific type of material to which these analyses apply by using values for the density, and the longitudinal and transverse wave speeds which are similar to those of the desired material. Equation (17) for the scattering cross section requires each of the properties mentioned here. We must therefore have some quantitative measurements of the density and the wave speeds found in manganese nodules. A summary of the measurements performed is given directly below. A detailed discussion of the procedures follows. Nodule samples from the Pacific (between California and Hawaii) and from the Atlantic (the Blake Plateau) were obtained from Deepsea Ventures, Inc. Two northern Atlantic nodules were obtained from Woods Hole Oceanographic Institution in Woods Hole, Massachusetts.

4.1 ACOUSTICAL MEASUREMENTS AND PROCEDURES

The nodules, which were in a semi-dried condition upon receipt, were submerged in water until saturation (usually occurring within 48 hours). Wave speed measurements were then performed, as well as weight and displacement volume measurements. The nodules were then kiln dried (at 108C) to constant mass and wave speed and weight measurements performed again. Wet and dry bulk densities, dry material densities, and porosities were determined and may be found in Appendix A. The compressional and shear wave speed measurements are also recorded in Appendix A. A more condensed form of the data containing information required for use in the scattering analysis may be found in Table 1.

Wet bulk density ρ_w simply equals the wet nodule mass M_w divided by the nodule volume V. In determining the wet mass, care was taken to remove excess surface water. Each nodule was weighed several times and the results averaged to reduce error. Dry bulk density ρ_d is computed similarly except that the dry nodule mass M_d is used.

$$\rho_{\omega,d} = \frac{M_{\omega,d}}{V} \tag{49}$$

where w denotes wet bulk and d denotes dry bulk. The volume includes all airspace (or fluid space) within the nodule (a significant fraction). Volumes were obtained on water saturated nodules by a displacement method. The steps are: fill a graduated beaker containing the nodule to a reference line with water; remove the nodule, taking care to let water which was clinging to the surface drip back into the beaker; read the displaced volume off the beaker. The material density is the density of the crushed nodule material (this excludes airspace volumes found in the porous whole nodule structure). It is found by first assuming the saturating water density to be 1.0 g/cc. The mass difference between the wet and the dry nodule is the mass of water retained in the porous nodule. This water mass may be converted to a fluid (or airspace) volume. Subtracting this airspace volume from the nodule displacement volume gives the solid nodule material volume. The dry nodule mass equals the nodule material mass (since the weight of any enclosed air is negligible). The solid material density is

$$\rho_{sm} = \frac{M_d}{V - \dfrac{(M_\omega - M_d)}{\rho_{H_2O}}} \tag{50}$$

where sm = solid material. The porosity γ, which is the ratio of airspace volume to the nodule volume, may be written

$$\gamma = \frac{\rho_{sm} - \rho_d}{\rho_{sm}} \times 100\% \tag{51}$$

The porosity is not directly used in the scattering analysis and both nodule densities and porosities are reported in the literature (Greenslate 1977). These measurements were performed however to ensure that the nodules contain no large eccentricities and are fairly representative of manganese nodules found in the Pacific and Atlantic Oceans.

The reader is referred to Figure (8) for a schematic of the wave speed measuring apparatus. Longitudinal and transverse wave speeds are measured using the corresponding acoustic transducer pairs. The signal generator is of the repeating impulse type. A generated 'input' pulse simultaneously excites the sending transducer and registers on an oscilloscope screen. The pulse travels through the nodule specimen and excites the receiving transducer. The signal emanating from the receiving transducer crystal is amplified and displayed on the oscilloscope screen in real time (with respect to the generated output pulse). The distance between the beginning of the input pulse and the beginning of the response signal (the signal that traveled through the nodule), as shown on the oscilloscope screen, is the travel time through the nodule and the system. (The system consists of anything the acoustic pulse travels through besides the nodule). A system time lag may be measured by placing the transducers face to face. Subtracting the system time lag gives the acoustic wave travel time through the nodule only. When making these measurements on a nodule, the transducers must be placed directly across from each other on parallel machined faces of the nodule. The travel time measurement divided by the distance between parallel faces yeilds the wave speed.

$$C = \frac{(t - t^*)}{d} \qquad (52)$$

where C is the wave speed, t* is the system time lag, and t and d are shown in Figure 8.

The type of wave speed measured depends upon the type of transducer pair used. A longitudinal transducer crystal can be excited into and can pick up a motion perpendicular to the plane of contact between crystal and nodule. The longitudinal wave speed then is a measure of compressibility and is defined as

$$C_L = \sqrt{E/\rho} \qquad (53a)$$

where E is the modulus of elasticity. A transverse transducer crystal excites or picks up a motion parallel to the nodule/crystal interface. The transverse wave speed is a measure of rigidity (e.g. fluids are non-rigid and therefore, allow no shear waves to propagate) and is defined as

$$C_T = \sqrt{G/\rho} \qquad (53b)$$

where G is the shear modulus of elasticity.

A coupling grease was used to mate the longitudinal transducers to the nodule surfaces for improved performance (better contact - clearer signals). No grease was used for the shear wave transducers which require contact friction between transducer and nodule surface to operate. Both transducer sets responded to larger pressures pushing them against the nodule faces by displaying clearer signals.

Rotating the compressional wave transducers while on the nodule faces had no effect. But, rotating the shear wave transducers affected the travel time readings (note that the orientation of the shear wave transducers relative to each other remained fixed during this rotation procedure), indicating that the nodules may have some annular shell type structure that responds to the direction in which the shear wave is applied. For our data, we attempted to record the minimum and maximum shear wave speeds possible.

An attempt to calibrate the system was made by taking air and water measurements. Some metal samples (copper, aluminum, and steel) were also measured and good results were indicated for both shear and compressional wave speeds. However, unknown alloy content of our test metals compared to metals tabulated in the literature prevented their use for the system's calibration. Both air and water measured about 2% high. Therefore, all wave speeds have been reduced by 2% from the measured values. It should be mentioned that while the metals could not be used for determining a calibration factor, their wave speeds consistently measured the same at different times indicating no creep in the system calibration setting. Air and water measurements generally measured the same but some very small variations were noted and may be attributed to temperature variations.

A possible reading error may also exist from reading the oscilloscope screen. The possible error here was found to be less than 3% for all nodule measurements taken except one which had a 6% reading error possible. The reading error magnitude depends on the time scale selected for display on the oscilloscope. The screen is divided into ten intervals and each interval is divided again into ten subintervals. We can discriminate to within plus or minus one half of a subinterval. The time length of one interval may be selected and the absolute error becomes ±.05 multiplied by that time length. The absolute error divided by the travel time recorded is the percent error possible in reading the screen.

4.2 DISCUSSION OF RESULTS

Major emphasis is to be given to the Pacific nodule measurements, for these are the nodules of interest to mining companies. However, Atlantic nodules were available and were therefore measured also. Appendix A gives complete listings of data recorded for each sample. In concensed Table 1, several samples are excluded from parts of the table for various reasons. Pacific nodules P1, P3, and P8 developed cracks which prevented some wave speed measurements from being made. Nodules P6 and P8 broke up before their densities and porosities could be determined. Shear wave speeds could not be determined for Atlantic nodules A4 and DR15 because the signal apparently could not make it through the nodules. Nodule CH58 in the wet condition allowed only a weak shear signal through that was quite low in speed compared to other Atlantic nodules. Examining the behavior of the shear wave in other wet nodules, we see that its speed should increase substantially over the speed for the dry nodule (not so for CH58). No external cracks are visible on CH58 and we can only assume that the weak signal was misread. Atlantic nodules DR15 and CH58 (obtained from Woods Hole Oceanographic Institute) were quite different in their appearance and their acoustical properties when compared to other Atlantic nodules. Their densities and their compressional and shear wave speeds (when measurable) were low, and their pores appeared to be filled with a very fine, light colored sediment.

In general, both Pacific and Atlantic nodules revealed wet densities and porosities very close to those found in the literature for Pacific nodules. Greenslate (1977) gives an average wet bulk density for Pacific nodules as 1.95g/cc and a porosity range of between 50 - 60%. The Pacific nodule samples measured to within 2.5% of the 1.95 g/cc average except for one nodule which was 9% high. Porosities were found to range from 50 - 55%. Average densities and porosities for Atlantic nodules are not found in the literature.

Pacific nodules show a smaller range of compressional wave speeds (1950m/s to 2500m/s) with the average (2350m/s) somewhat lower than comparable measurements for Atlantic nodules (which ranged from 2125m/s to 3215m/s and averaged at 2605m/s). The shear wave speed ranges were about the same (1615m/s to 2645m/s) for Pacific and Atlantic nodules. Pacific nodules were less sensitive to shear wave orientation. The higher compressional wave speeds and the greater sensitivity to shear direction in the Atlantic nodules may both be due to the presence of many veins of very hard, white calcareous material (see Gladsby 1977 for a chemical analysis) that is not found in Pacific nodules. The ratio of the shear wave speed to the compressional wave speed ranged from 0.83 to 0.98 in the Pacific nodules and from 0.69 to 0.80 in the Atlantic nodules.

4.3 FURTHER INVESTIGATION

The Atlantic nodules appeared to be much more structurally sound whether in a wet or dry condition. The Pacific nodules, after drying, tended to break up or develop cracks easily. Visual inspection showed no external cracks in the nodules (which had been dried out before receipt) for which wave speed measurements were obtained. Whether internal cracks existed or not in the Pacific or Atlantic nodules is not known. There is also evidence that general pore structure damage may occur during drying out. Possible internal cracks or pore structure damage in nodules that have been dried out may result in different mechanical properties and most likely in slower wave propagation speeds because of a less homogeneous medium. The nodules were measured at atmospheric pressures and temperatures.

Ideally, freshly recovered nodules packed in seawater should be measured (for wave speeds) at assimilated ocean deep pressures and temperatures. A larger sample group shoule be utilized for greater confidence in the results.

However, given that these are the first quantitative accounts of acoustical wave velocities in manganese nodules, the results are satisfactory for use in the scattering analyses.

Table 1. Acoustical Properties of Manganese Nodules

CONCRETION TYPE	WAVE SPEEDS			DENSITY (g/cc)
	C_L (m/s)	C_T (m/s)	C_T/C_L	
PACIFIC NODULES	1950 - 2500 [2350]*	1615 - 2450 [2000]	0.83 - 0.98	1.91 - 1.96
ATLANTIC NODULES	2125 - 3215 [2605]	1625 - 2580 [1980]	0.69 - 0.80	1.89 - 2.07

* [ ] - average

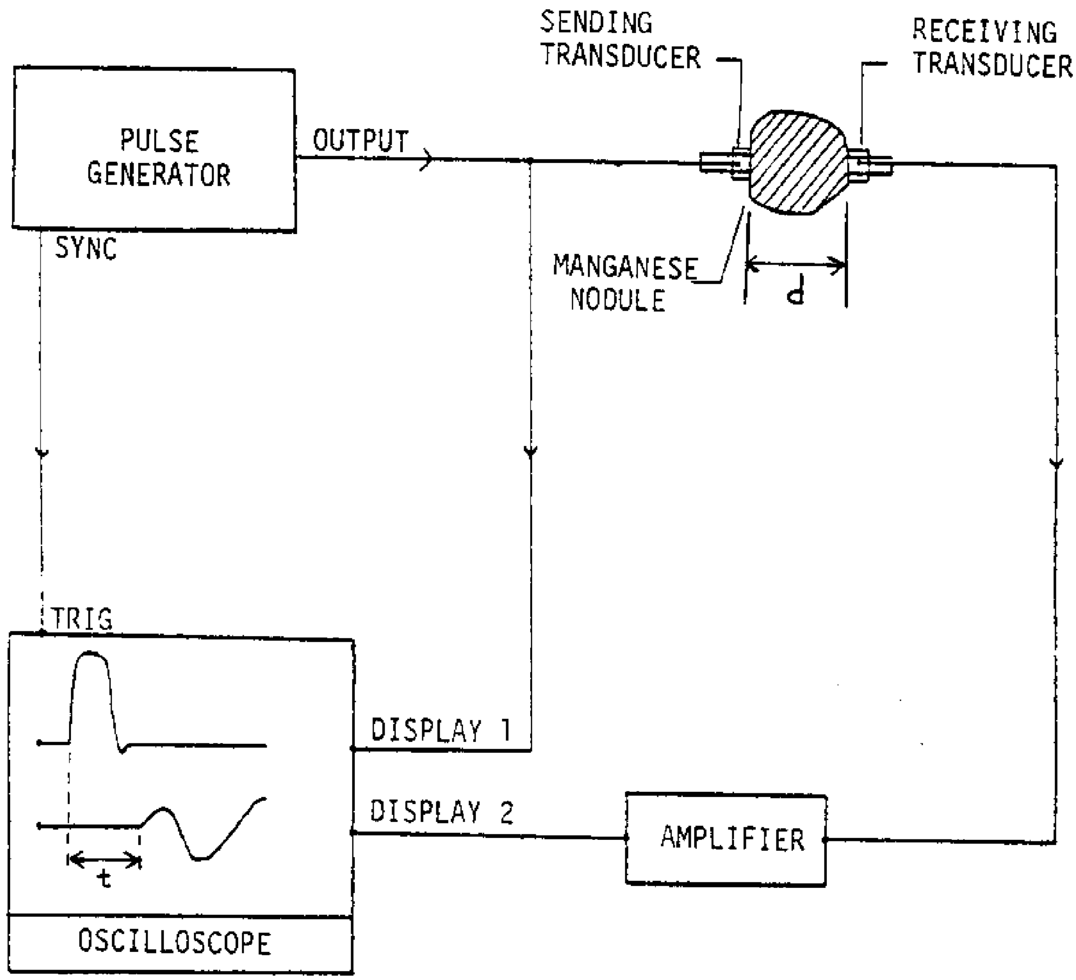

Figure 8. Schematic of Wave Speed Measurement Apparatus

Chapter V

SIZE DISTRIBUTIONS IN MANGANESE NODULE FIELDS

We wish to determine a statistical area distribution function that characterizes the frequency with which nodule cross sectional areas occur (relative to the local average area) in any particular nodule site. Such a function would describe the statistics of nodule sizes which are required for the multiple scattering analysis ($\alpha(s_i)$ in equation (33)). We can also develop analytic relationships between average radii of different powers. Note that

$$\overline{a^n} \neq \bar{a}^{\,n}$$

where a is the radius and the overbar denotes the average over a group of nodules.

For acoustic wave frequencies in the Rayleigh region (where the wavelength is long compared to the nodule dimensions), the scattered pressure is proportional to the radius cubed. Therefore, the average pressure scattered from a nodule is proportional to $\overline{a^3}$ and is conveniently proportional to the nodules' average volume - of great interest to mining concerns. However, the average radius is also needed to ensure equipment/nodule compatibility, and this requires relating $\bar{a}$ and $\overline{a^3}$. For incoming acoustic wave frequencies in the resonance region (that is, for frequencies between the low frequency Rayleigh scattering region and the high frequency geometrical scattering region), the scattered pressure is a more complicated function of radius (Ma 1981) which has not been averaged yet. The averages of the radius and the cubed radius must be obtainable from whatever averaged power of the radius term that may occur. A general relationship between averages of radii to various powers is sought. The sources of data and data preparation are described directly below. A discussion of the mathematical manipulations required to transform between averages of different powers of the radius follows.

5.1 DATA REDUCTION

Two sources of data have been utilized for finding area distribution functions. Data was obtained directly from several black and white bottom photographs supplied by Deepsea Ventures, Inc. and also from physical characteristics tables of various central Pacific nodule sites compiled by Fewkes, McFarland, Reinhart, and Sorem (1979 and 1980). Each characteristics table examines a small representative nodule site (typically a sea floor area of about 2500 cm**2) containing around 75 nodules. Listed in the tables are the floor plane cross sectional areas, the lengths, and the widths of each individual nodule in the site. From the floor plane areas (listed in Appendix B) the average cross sectional area of each data set is determined, and this quantity characterizes a curve describing the distribution of cross sectional areas. Obtaining data from the photographs requires considerable effort since the bottom plane cross sectional area for each individual nodule must first be determined.

The photographs are taken from less than ten meters above the Pacific Ocean floor, approximately 4000 meters below the water surface. In only one of the photographs is there a real length scale at the sea floor available. (This does not prevent analysis of the other photographs however, because the objective is to determine the distribution of the areas relative to some average area, not to predict or determine real scale areas.) One 35mm color slide of each photograph has been prepared. Three calibration slides to check projection distortion have also been produced. These consist of various angles and scale lengths placed in different portions of the 35mm slide frame. When projected onto a screen, the calibration slides showed no discernable distortions of lengths or angles in any portions of the slide frame when the projector was properly positioned (i.e. when leveled and squarely facing the screen).

A nodule field slide is projected onto a large hanging screen of white paper. A compromise must be made between projected nodule size on the screen and nodule definition. For ease of measurement, the largest size possible is desired for the projected nodule images at the screen (affected by pulling the projector away from the screen and using a zoom lens). But at the same time, the sharpest image possible is desired to distinguish the background shades of gray from the sometimes only slightly darker grays of the nodules themselves (pulling the projector away from the screen results in greater light diffusion losses, causing lessened edge definition). All the nodules are traced onto the screen, and any resolution problems are settled by reference to the original photograph.

The projected cross sectional area of each traced nodule is determined by use of a manual planimeter, in effect, a mechanical integrator. The outline of each traced nodule must be followed by the planimeter tracing point. After one trip around the perimeter, the nodule projected area (unscaled) may be read directly from the planimeter in square inches. If a real scale length is provided in the photograph, the real cross sectional area of each nodule may be determined. Otherwise, these projected areas are unscaled. Note that data was collected and reduced from only two photographs. This is extremely tedious work and since data is available in already reduced form (Fewkes' tables), examining all the photographs was unnecessary.

There are three types of error possible in using the planimeter: inaccurate reading of the area from the instrument, recording error; inaccurate tracing of the outline of the nodule, execution error; and, inaccurate calibration of the instrument, calibration error. The smallest division marked on the planimeter is a tenth of a square inch and so our recording error is one half of that or .05 in**2. A repeatability test showed execution error to be less than .05 in**2, the recording error (during which, extra care was taken in reading the planimeter scale in order to minimize recording error). An accuracy test on a 1.0 in**2 square showed calibration error to be undetectable (at least within the bounds afforded by the other errors). These measurement errors are relatively unimportant because we are attempting to determine qualitative properties of the distributions, not precise quantitative information.

One photograph was examined as a whole (consisting of 388 nodules) and also in two subsections (consisting of 246 and 142 nodules each). The resulting curves were compared. The tables from Fewkes et al. do not permit sectioning because the physical arrangement of the nodules on the ocean floor is unknown.

First, we must allocate each nodule size in a data set into its discretized interval of cross sectional area. That is, we need to know how many nodules have cross sectional areas between 0 and limit 1, between limit 1 and limit 2, and so on until all nodules have been accounted for. Each interval should have the same size. The size is arbitrary but initially, it should be as small as practically possible. If the interval size proves to be too small (as will be discussed shortly), combining adjoining intervals to make larger (but preferably still equal sized) intervals is simple.

This process will give an area distribution (i.e. number of nodules vs. cross sectional area interval) for a data set in histogram or bar graph form. Or one may transpose to the radius distribution or to the radius to the second, third, or sixth power distributions by plotting the number of nodules within each interval against the appropriate interval of radius raised to whatever power (see plots).

Referring to the data sets 1a, 1b, and 1c (listed in Appendix B), we see interval sizes of 2.4 - 2.5 cm**2. This spacing actually corresponds to interval sizes of 0.1 in**2 (the smallest measurement size possible using the planimeter) transformed to the metric scale and multiplied by a real scale ratio (derived from the real scale length supplied in the photograph). Examining this data, we see that there are a possible 33 intervals. But, plotting the distribution of nodules against 33 area intervals in bar graph form would result in an excessively rough graph (a problem inherent in small data sets and remedied by obtaining larger data sets or, in this case, by using larger discretized plotting intervals). By using two, three, or more intervals in a row as a new larger interval spacing, the histogram can be smoothed out. Smoothing of the graph is necessary in order to fit a curve to it. Note that the data sets from Fewkes' tables (real scale data) are classified into 1 cm**2 intervals (Appendix B, Data sources 3 through 8), but the bar graphs produced for this data (Figure 17 and Figures 20 through 24) use 3 cm**2 intervals for a smoother bar graph representation of the distributions.

5.2 SIZE DISTRIBUTION STATISTICS

From the statistics of the radius squared data, we can calculate an average of the squared radius $\overline{a^2}$ and the variance of the radius squared σ_{a^2}. Likewise, we can calculate the average radius $\overline{a}$, the average of the cubed radius $\overline{a^3}$, the average of the radius to the sixth power $\overline{a^6}$, and corresponding variances of the radius to a power. The general form for the average mth power of the radius $\overline{a^m}$ is

$$\overline{a^m} = \frac{1}{N}\sum_{i=1}^{N} a_i^m\, n_i \qquad (54)$$

and for the variance of that average σ,

$$\sigma_{a^m} = \left[\frac{1}{N}\sum_{i=1}^{N}(a_i^m - \overline{a^m})^2\, n_i\right]^{1/2} \qquad (55)$$

where N is total number of nodules, a_i^m is some discrete size, n_i is the number of nodules having size a_i^m, and m is the power of the radius under consideration.

It was found that a Rayleigh probability function (or density) describes the radius squared distribution quite well (the radius square distribution and the area distribution are the same). The Rayleigh probability function for the radius squared distribution is;

$$q(x) = \frac{x}{b^2}\, e^{\frac{-x^2}{2b^2}} \qquad (56)$$

where $x = a^2$ and b is related to the average squared radius $\overline{a^2}$ (the relationship will be derived shortly). Thus, the nodule size distribution (for any radius power) is specified by the single Rayleigh parameter b which may be quantified from real data (i.e. area statistics), or used to relate the averages of different powers of the radius. In Davenport and Root (1958) a discussion is given on monotonically increasing or decreasing probability function sets and their use in other single variable functions as the single variable. An expression is obtained which is of use in relating the probability densities for different powers of the radius;

$$q_n(y) = q_2(x)\left|\frac{dx}{dy}\right| \tag{57}$$

where $y = a^n$, $x = a^2$, and q_n and q_2 are probability functions of radii to the indicated powers (indicated by subscripts). For this particular case;

$$q_n(y) = \frac{x}{b^2} e^{\frac{-x^2}{2b^2}}\left|\frac{dx}{dy}\right| \tag{58}$$

To determine the radius probability density, we let

$$y = a = x^{1/2}$$

then

$$\frac{dy}{dx} = \frac{1}{2x^{1/2}}$$

$$q_1(y = a) = \frac{x}{b^2} e^{\frac{-x^2}{2b^2}} \left|2x^{1/2}\right|$$

$$q_1(a) = 2\,\frac{a^3}{b^2}\, e^{\frac{-a^4}{2b^2}} \tag{59}$$

Similarly, to determine the radius cubed probability density, we let

$$y = a^3 = x^{3/2}$$

then

$$\frac{dy}{dx} = \frac{3}{2} x^{1/2}$$

and we find

$$q_3(a^3) = \frac{2}{3} \frac{a}{b^2} e^{\frac{-a^4}{2b^2}} \qquad (60)$$

By following the above procedures through with $y = a^n$, we find the general formula for the a^n probability density (where n is real and positive):

$$q_n(a^n) = \frac{2}{n} \frac{a^{(4-n)}}{b^2} e^{\frac{-a^4}{2b^2}} \qquad (61a)$$

or

$$q_n(a^n) = \frac{2}{n} \frac{x^{(2-\frac{n}{2})}}{b^2} e^{\frac{-x^2}{2b^2}} \qquad (61b)$$

where $x = a^2$. The last equation is in terms of x instead of a in order to remind us that this analysis is based on a radius squared distribution curve fit. It now remains to evaluate the Rayleigh parameter b.

By definition of a statistical average,

$$\bar{a} = \overline{x^{1/2}} = \int_0^\infty x^{1/2} q_2(x)dx$$

$$= \int_0^\infty \frac{x^{3/2}}{b^2} e^{\frac{-x^2}{2b^2}} dx \qquad (62)$$

and

$$\overline{a^2} = \overline{x} = \int_0^{\infty} x \; q_2(x)\, dx$$

$$= \int_0^{\infty} \frac{x^2}{b^2} e^{\frac{-x^2}{2b^2}} dx \qquad (63)$$

Similar equations are obtainable for $\overline{a^3}$ or any $\overline{a^n}$ (for n real and positive). From integration formula tables, we know

$$\int_0^{\infty} \eta^{\nu-1} e^{-\mu\eta} d\eta = \mu^{-\nu}\Gamma(\nu) \qquad (64)$$

for ν real and greater than zero. In general, the gamma function $\Gamma(\nu)$ is given by

$$\Gamma(m + \tfrac{1}{2}) = \frac{\sqrt{\pi}}{2^m} (2m - 1)!! \qquad (65)$$

for an integer m. For a non-integer argument, the function is tabulated in mathematical handbooks. We can use this integration if we let

$$\eta = x^2$$

then

$$d\eta = 2x dx$$

For the average radius squared given by equation (63), we find

$$\overline{a^2} = \frac{1}{2b^2} \int_0^{\infty} \eta^{1/2} e^{\frac{-\eta}{2b^2}} d\eta \qquad (66)$$

requiring that

$$\nu = 3/2$$

and

$$\mu = \frac{1}{2b^2}$$

Then

$$\overline{a^2} = \left(\frac{1}{2b^2}\right)\left(\frac{1}{2b^2}\right)^{-3/2}\Gamma(3/2) \qquad (67)$$

By using gamma function tables, we find

$$\overline{a^2} = 1.2533b \qquad (68)$$

Similarly, we can find

$$\bar{a} = 1.0780\ b^{1/2} \qquad (69a)$$

$$\overline{a^3} = 1.5457\ b^{3/2} \qquad (69b)$$

$$\overline{a^6} = 3.7598\ b^3 \qquad (69c)$$

Following the above procedures through for $\overline{a^n}$ we find the following:

$$\mu = \frac{1}{2b^2} \qquad (70)$$

$$\nu = \frac{n}{4} + 1 \qquad (71)$$

and the general formula for the average of the radius to the power n is;

$$\overline{a^n} = \left(\frac{1}{2b^2}\right)^{\frac{-n}{4}}\Gamma\left(\frac{n}{4} + 1\right) \qquad (72)$$

for any real positive value of n.

This shows that the average radii to different powers are related by only one parameter - b. Below are some example transforms to $\overline{a^3}$ from various other average radii powers.

$$\overline{a^3} = 1.2388\ \bar{a}^{\,3} \qquad (73a)$$

$$\overline{a^3} = 1.1016\ \overline{a^2}^{\,3/2} \qquad (73b)$$

$$\overline{a^3} = 0.7972\ \overline{a^6}^{\,1/2} \qquad (73c)$$

5.3 DISCUSSION OF RESULTS

Plots are presented for the distributions of the radius a, the radius squared a^2, and the radius cubed a^3 in Figures 9 through 30. Radius square histograms or bar graphs represent actual ocean floor area measurements of nodules taken from photographs or data tables (all values are real size except those from data source 2 which are unscaled). Radius and radius cubed histograms are derived assuming spherical nodules. This is obviously not the case for real nodules and will be commented on later.

The Rayleigh probability density curves for a^2 and the predicted probability density curves for a and a^3 fit the discretized data (bar graphs) quite well. Average radius functions are indicated on the plots by dashed lines. To be matched by the probability density curves, the bar graphs have been normalized by dividing the number of nodules in each interval by the total number of nodules in the data set and by the interval size.

Plotted in Figure 31 are several data sets from various sites in the Pacific Ocean (data sources 1a, 2, 8, 9) with nearly the same average nodule size. The points represent the middle of each discretized interval from each of the data set histograms. The data sets were individually normalized as described above and then each set was non-dimensionalized by corresponding values of a. That is, the non-dimensional number of nodules to be plotted along the ordinate axis for one data set equals

$$\frac{n_i}{XINT \cdot N} \cdot \overline{a}^{\,2}$$

where n_i is the number of nodules in interval i, XINT is dimensional width of interval i, and N is total number of nodules for which $\overline{a}$, n_i, and N refer to only one data set. The radius squared on the abscissa axis is non-dimensionalized by dividing by the square of the average radius averaged over all the data sets. The Rayleigh probability density p(x) is non-dimensionalized by multiplying equation (57) by the averaged average radius and using the non-dimensional radius square (plotted on the abscissa axis) as the argument x. The probability curve is normalized to fit all the data sets by computing an average Rayleigh parameter b. This involves computing an averaged average square radius (not to be confused with the square of the averaged average radius). The resulting probability curve fits the data points rather well. Figure 32 is a similar plot using Pacific Ocean sites (data sources 3 through 7) that were all physically within 107 meters (350 feet) of each other. The results are similar.

The measured average radius, and the averages of the second, third, and sixth powers of the radius are listed for each data source in Appendix B. Again, these are based on true measured values of the radius squared (except for the unscaled case of data source 2). Equations (73) are related by the Rayleigh parameter b (see equations 68 and 69). By these equations, we can use averages of the radius to various powers to predict say $\overline{a^3}$ and then compare the predicted $\overline{a^3}$ with the measured $\overline{a^3}$. In doing this for many of the data sources, the error is found to be less than ±5% in most cases. Errors incurred by assuming $\overline{a^3} = \overline{a^n}^{3/n}$ may be as much as 50%.

5.4 <u>FURTHER INVESTIGATION</u>

As mentioned earlier, Pacific manganese nodules are not spherical and so the relationship between the length (the radius), the ocean floor area (the radius squared), and the volume (the radius cubed) of a nodule is not simple. McFarland (1980) has empirically derived a relationship between nodule mass (volume times density) and the longest (floor plane) length of typical nodules (the longest dimension of the nodules almost always occurs in the ocean floor plane since nodules are flattened in the vertical direction). The relationship has the form

$$\text{MASS} = .54\ (\text{LENGTH})^{2.67} \qquad (74)$$

Whether or not this relationship holds over large areas of Pacific Ocean is not known. This involves questions on whether the growth characteristics of nodules are the same anywhere in the Pacific. Fewkes' tables, from which several data sets of floor plane areas were taken (Appendix B), also include length to width ratios of nodules (note McFarland is a co-author with Fewkes and the nodule mass to length relationship is quite likely based in part on Fewkes' length to width ratios). Examining results from tests of the system proposed in this paper may indicate if further investigation is required on the effects of the length to mass relationship and the length to width ratios.

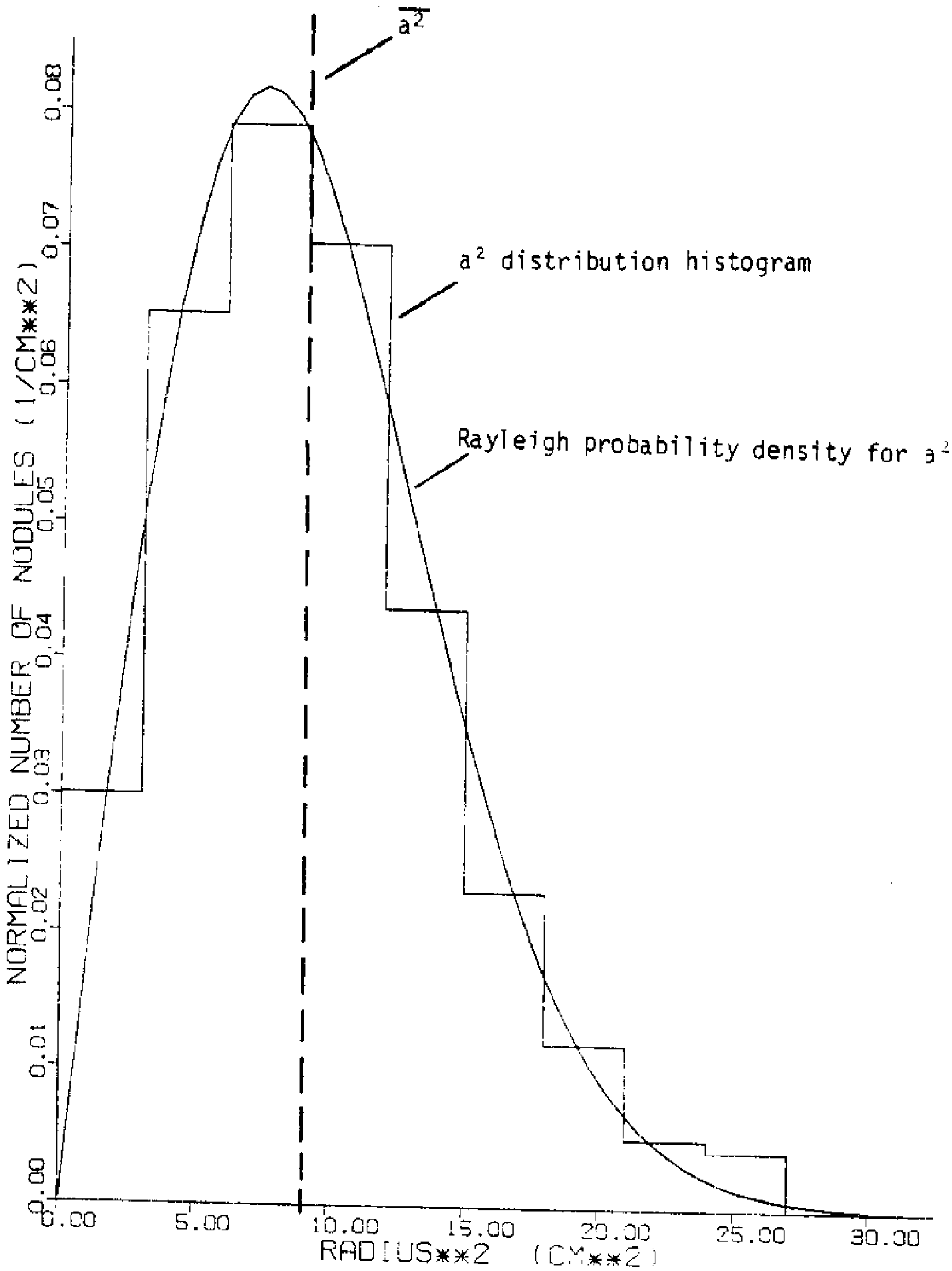

Figure 9. Size Distribution Curve Fit for Data Source 1a

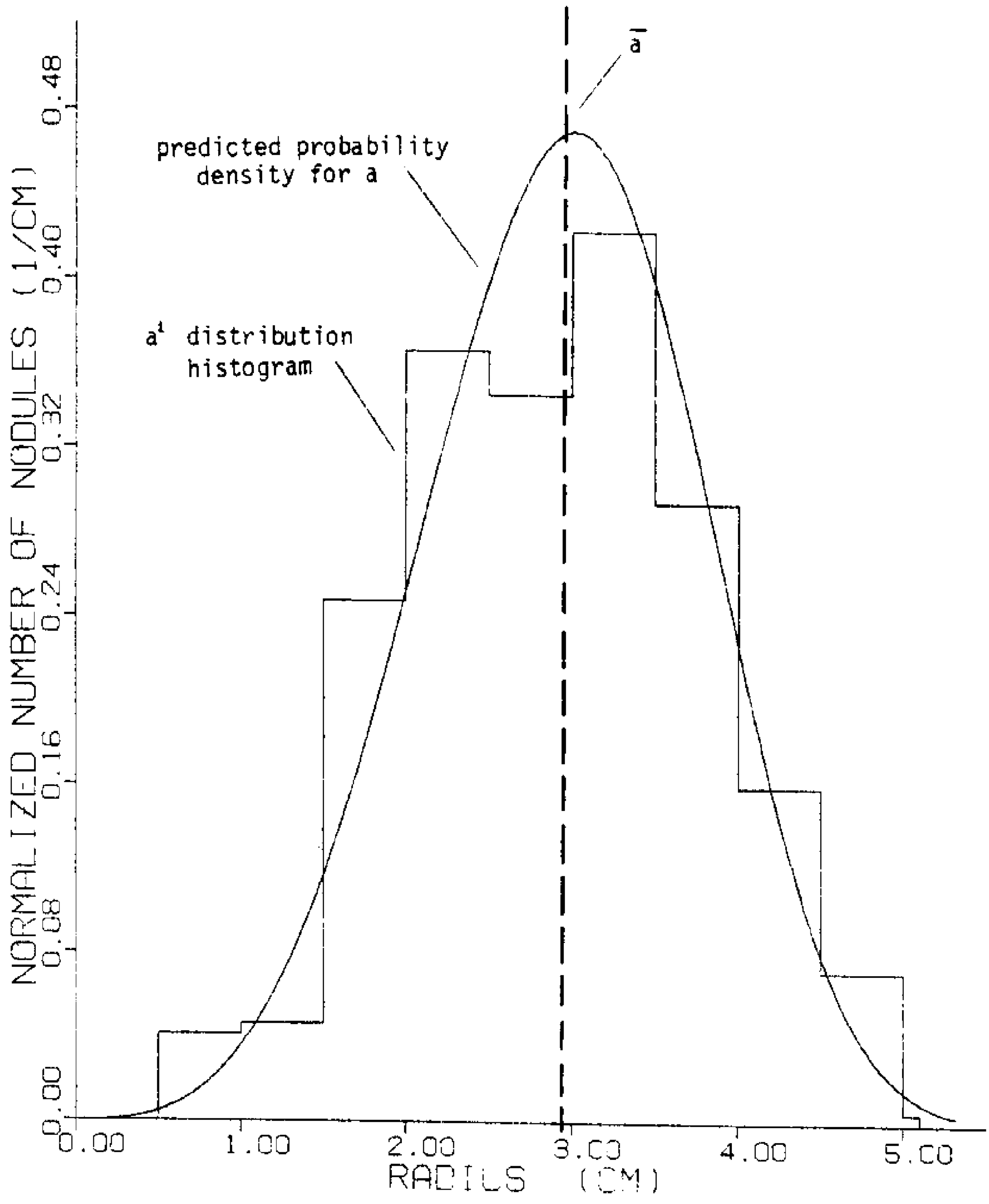

Figure 10. Size Distribution Curve Fit for Data Source 1a

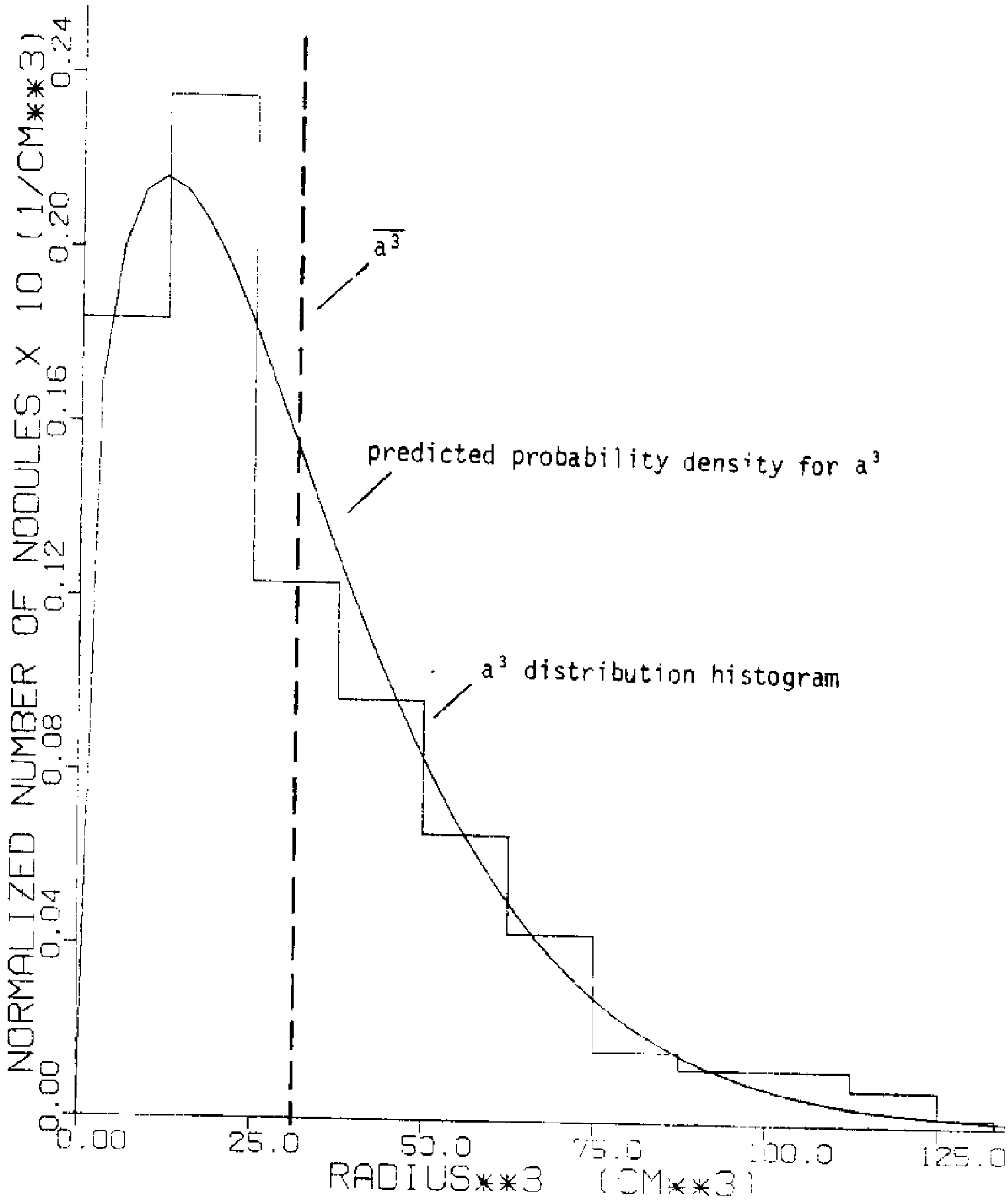

Figure 11. Size Distribution Curve Fit for Data Source 1a

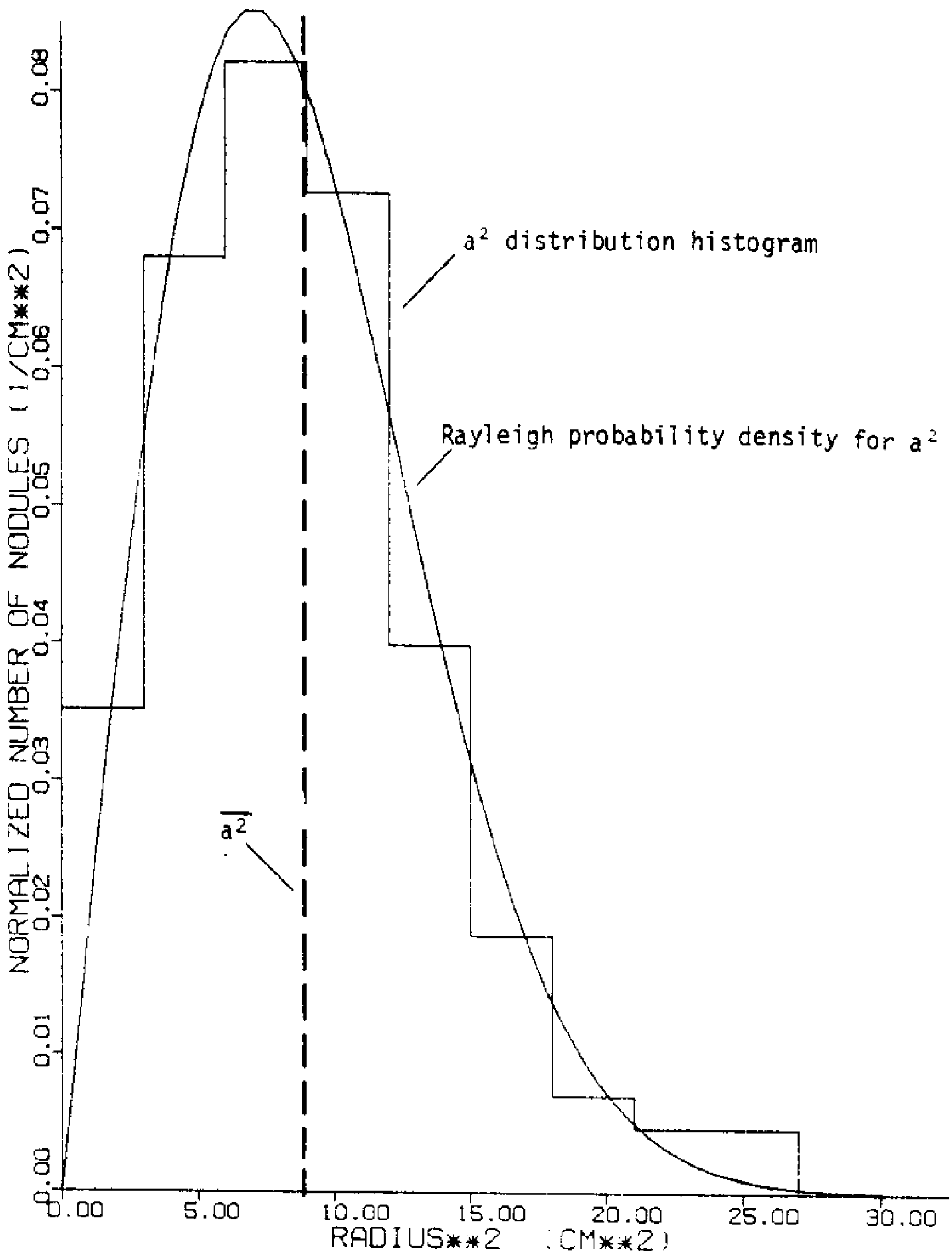

Figure 12. Size Distribution Curve Fit for Data Source 1b

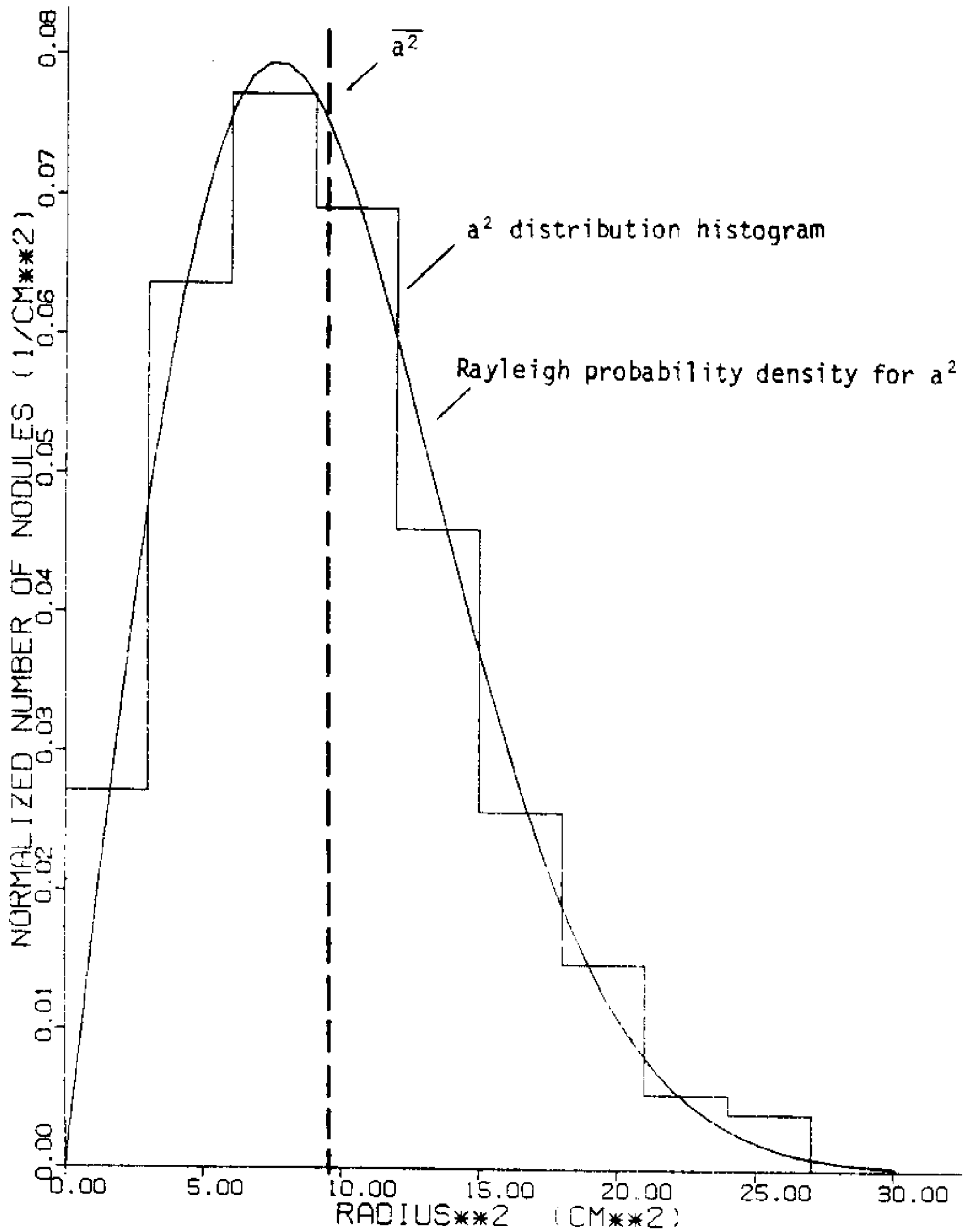

Figure 13. Size Distribution Curve Fit for Data Source 1c

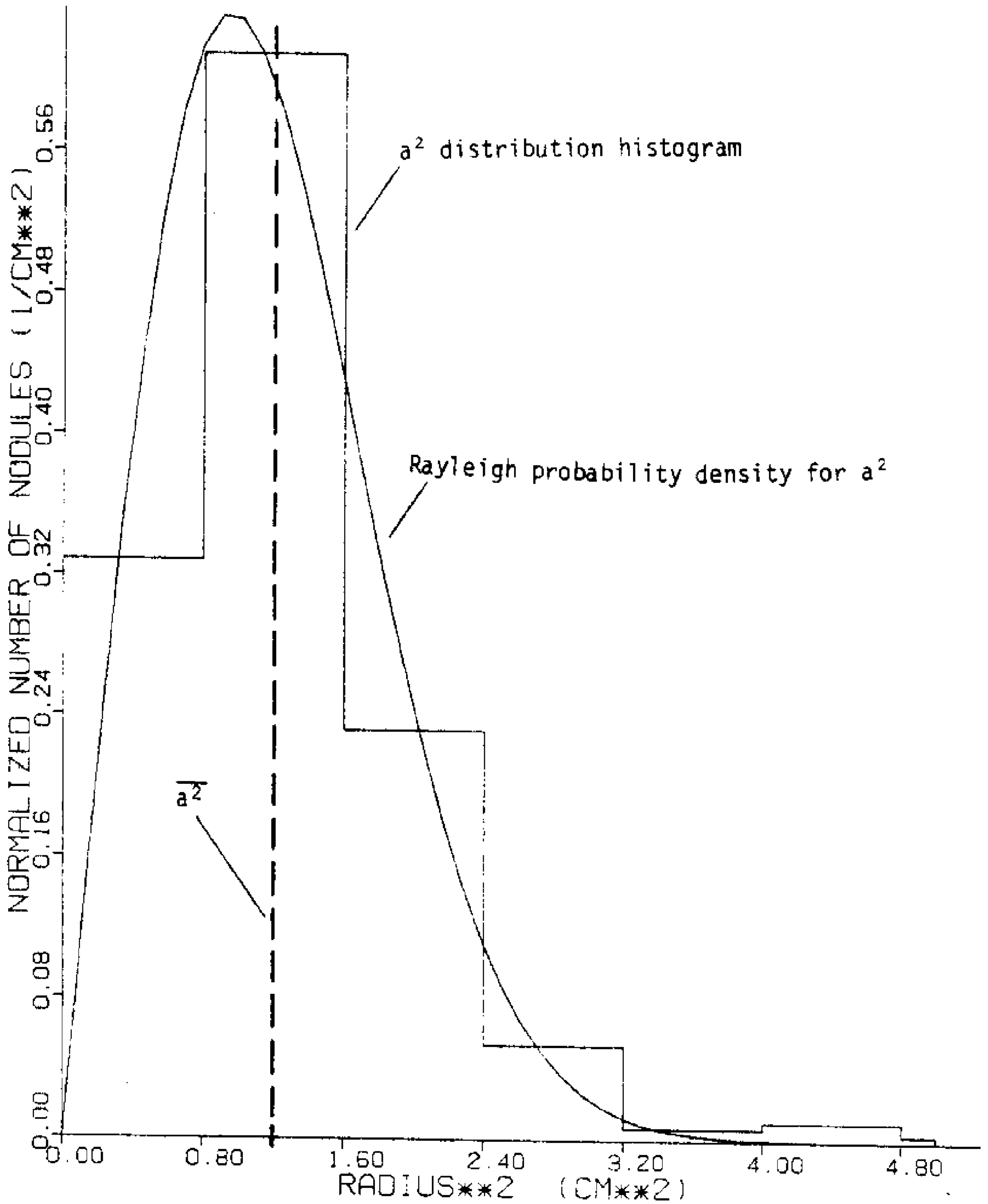

Figure 14. Size Distribution Curve Fit for Data Source 2

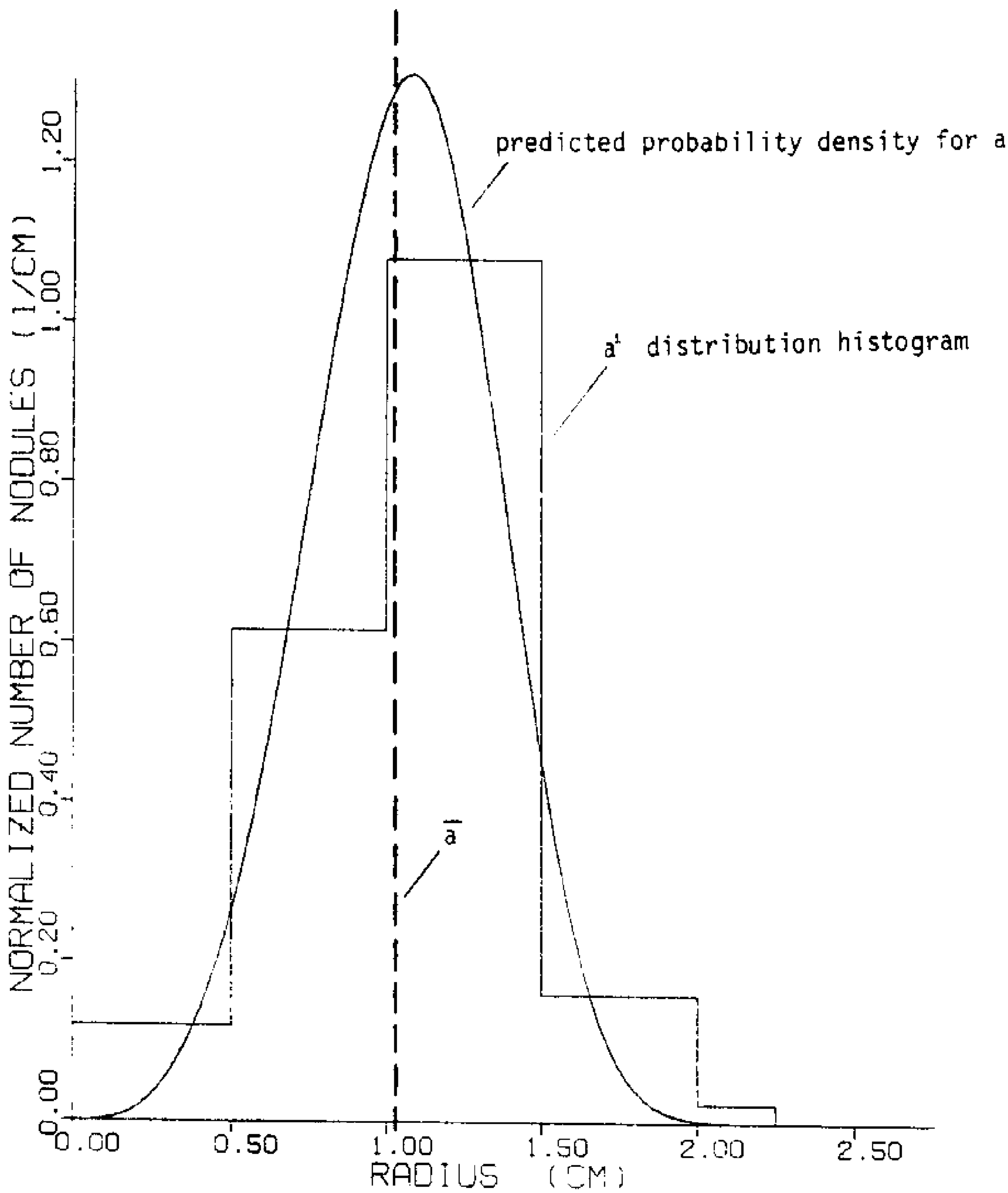

Figure 15. Size Distribution Curve Fit for Data Source 2

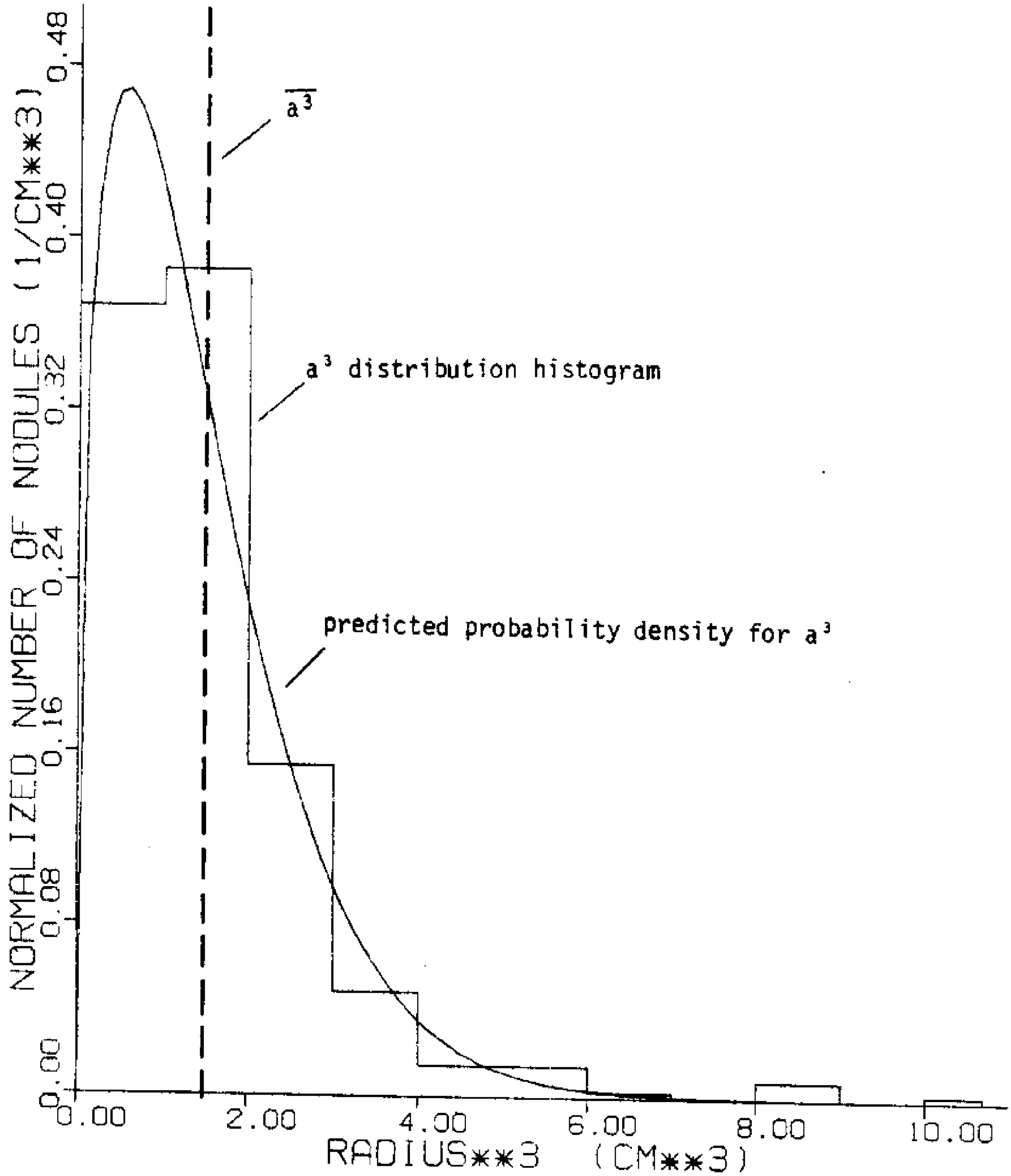

Figure 16. Size Distribution Curve Fit for Data Source 2

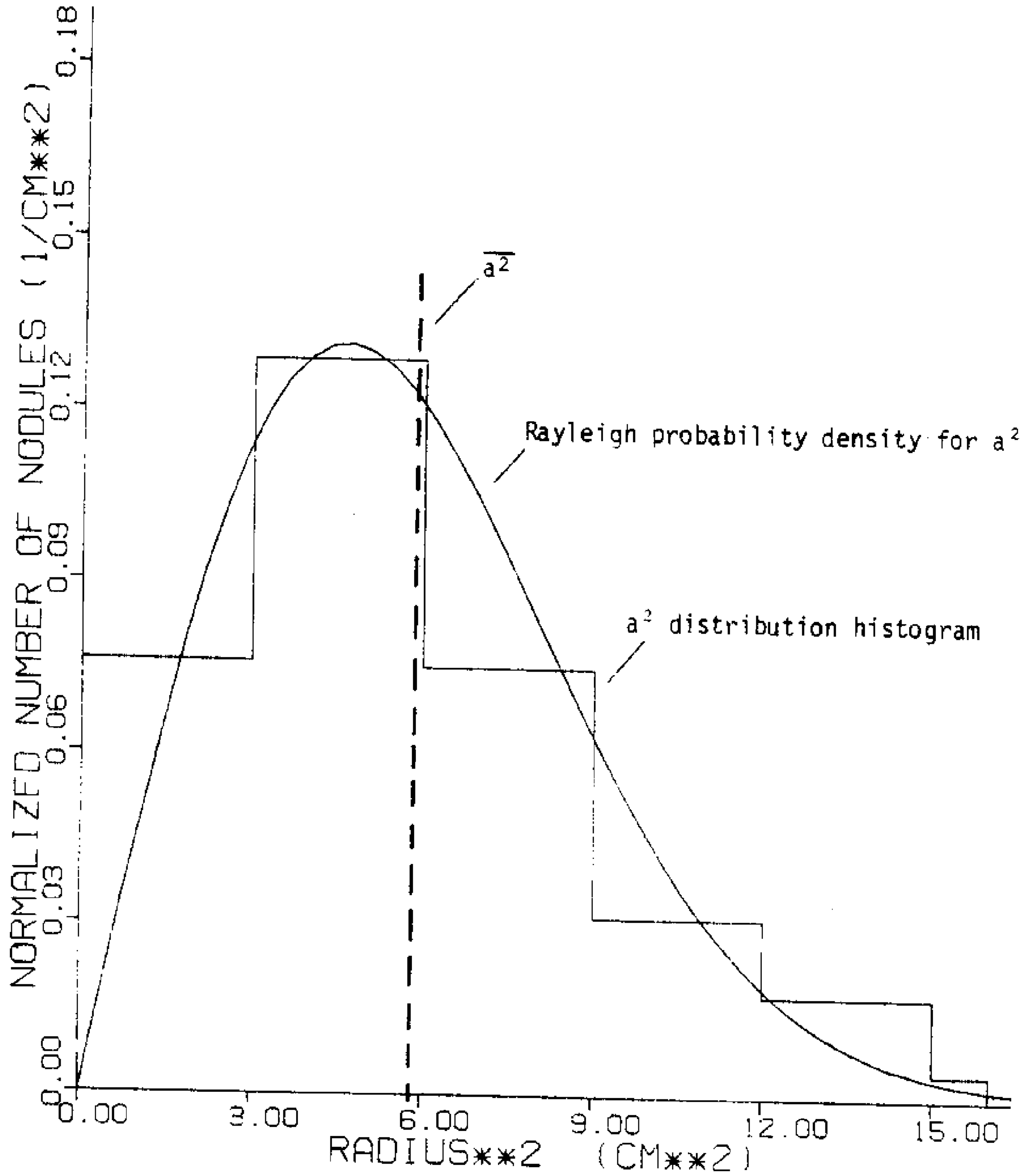

Figure 17. Size Distribution Curve Fit for Data Source 8

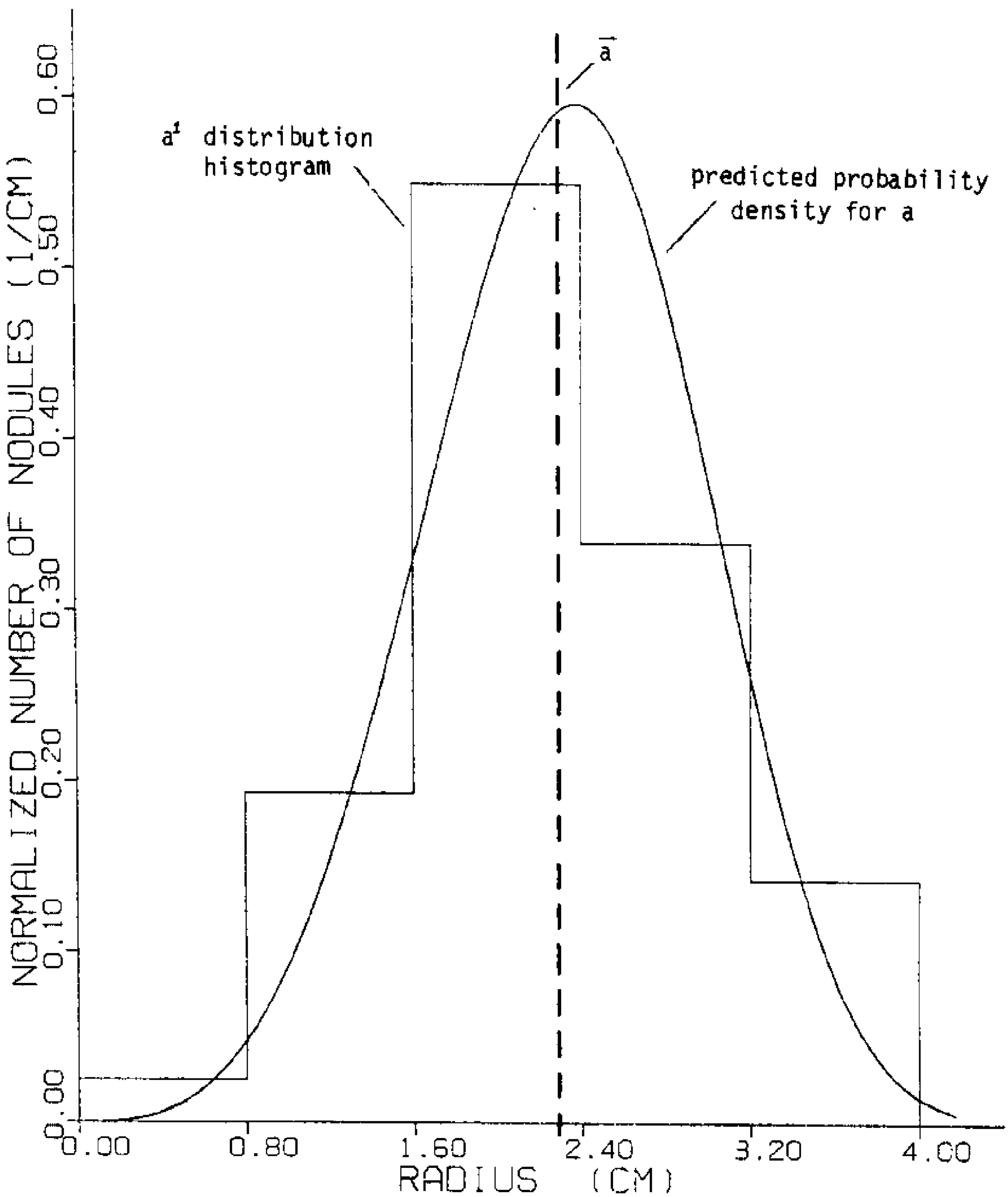

Figure 18. Size Distribution Curve Fit for Data Source 8

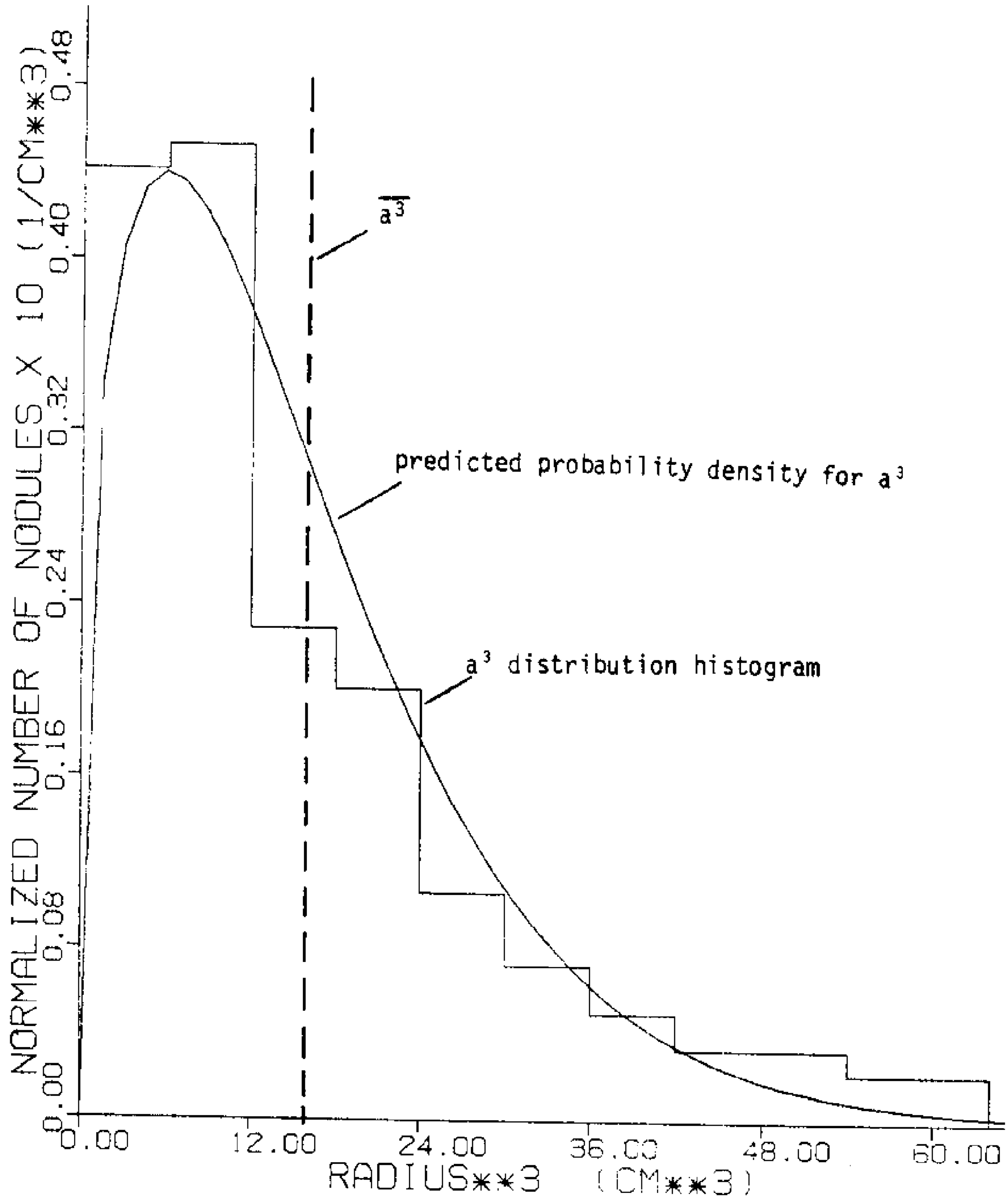

Figure 19. Size Distribution Curve Fit for Data Source 8

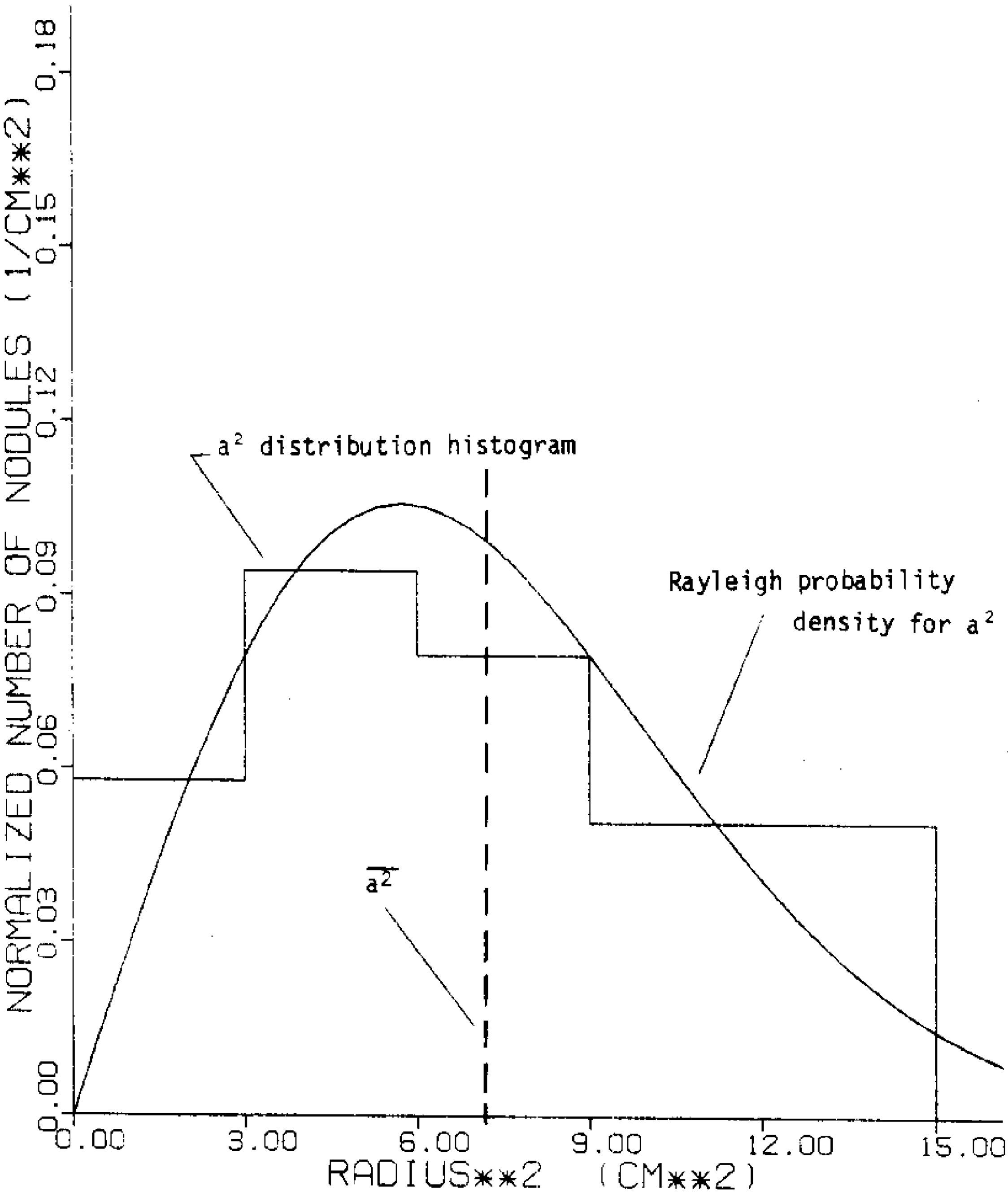

Figure 20. Size Distribution Curve Fit for Data Source 3

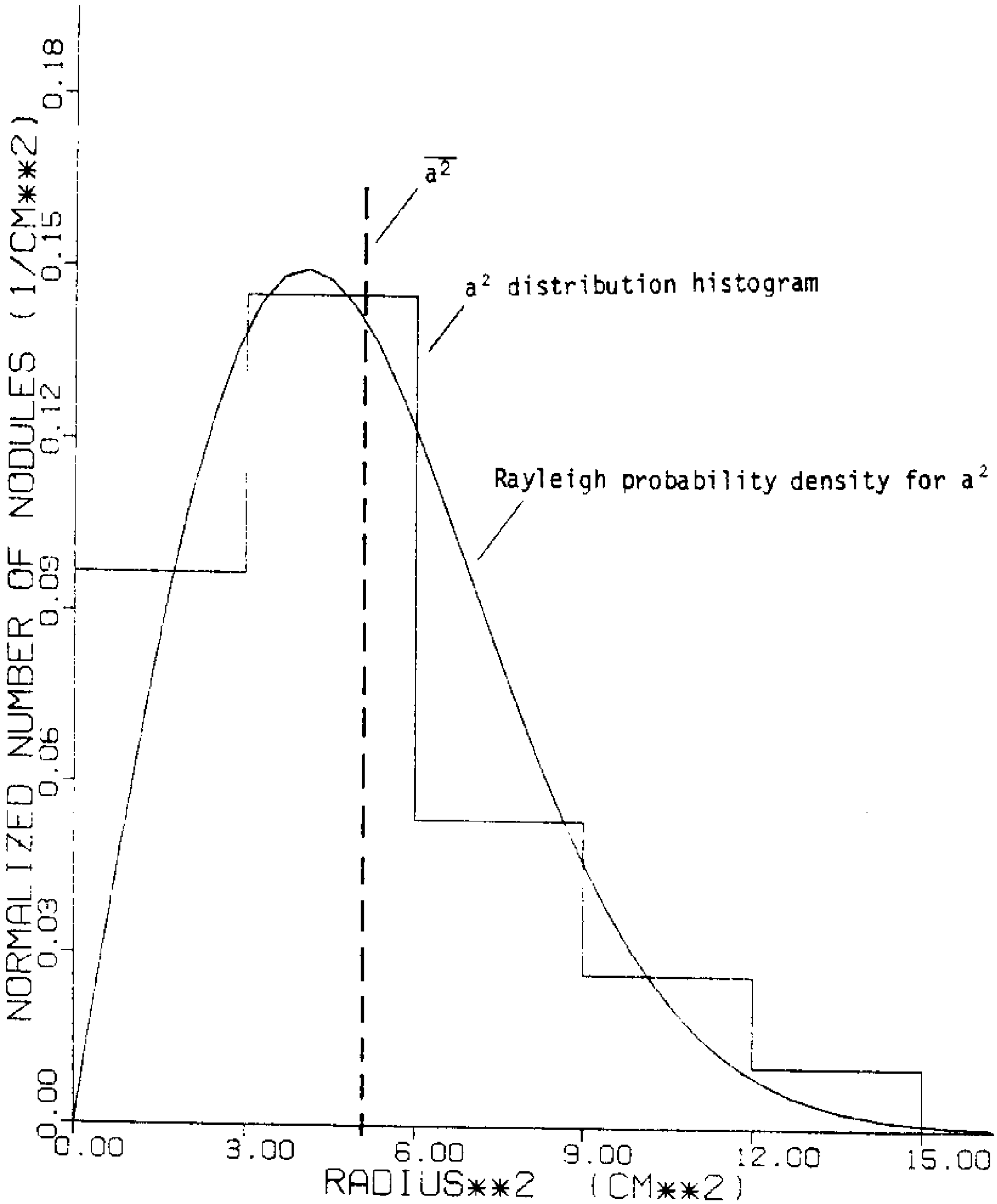

Figure 21. Size Distribution Curve Fit for Data Source 4

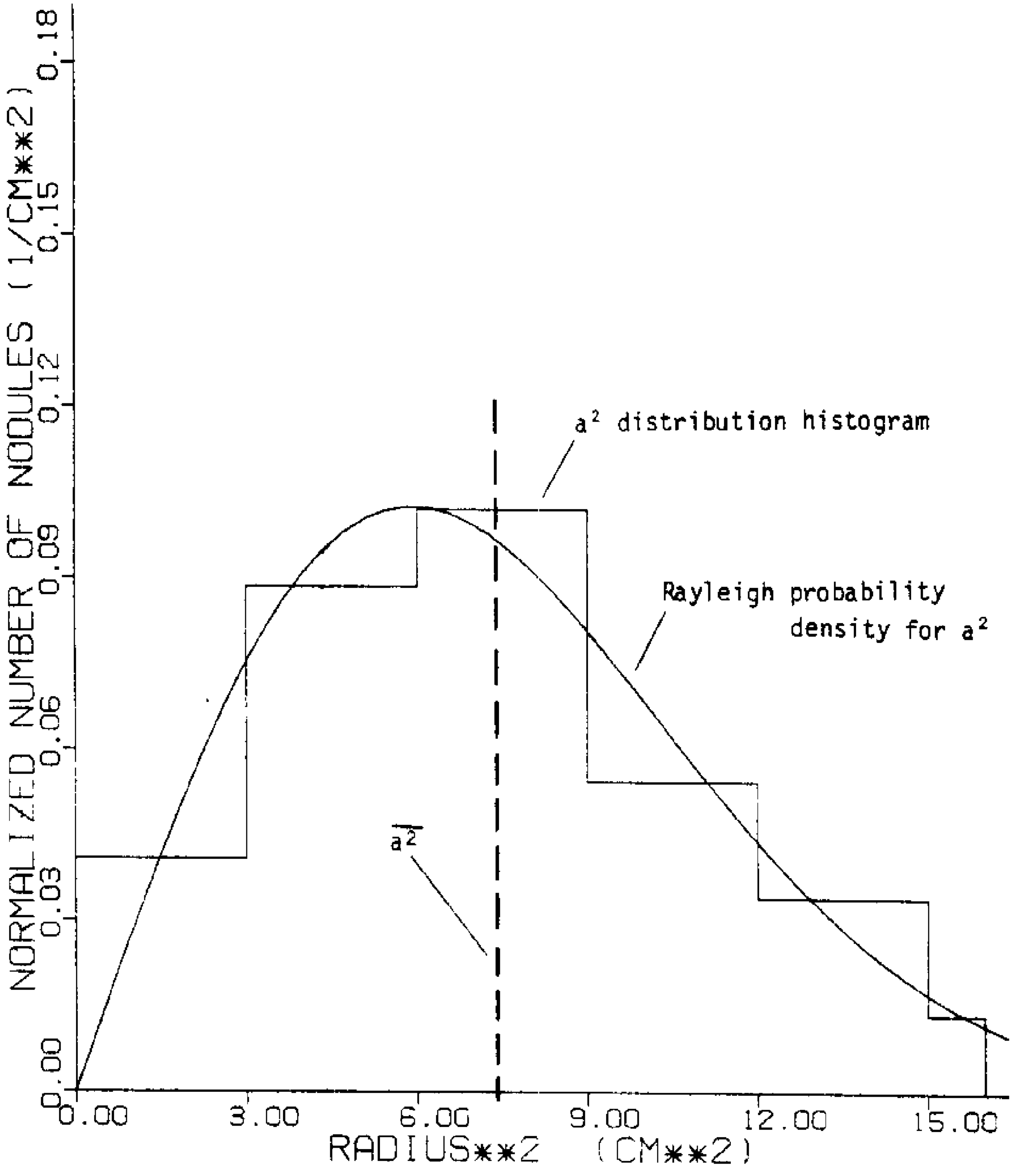

Figure 22. Size Distribution Curve Fit for Data Source 5

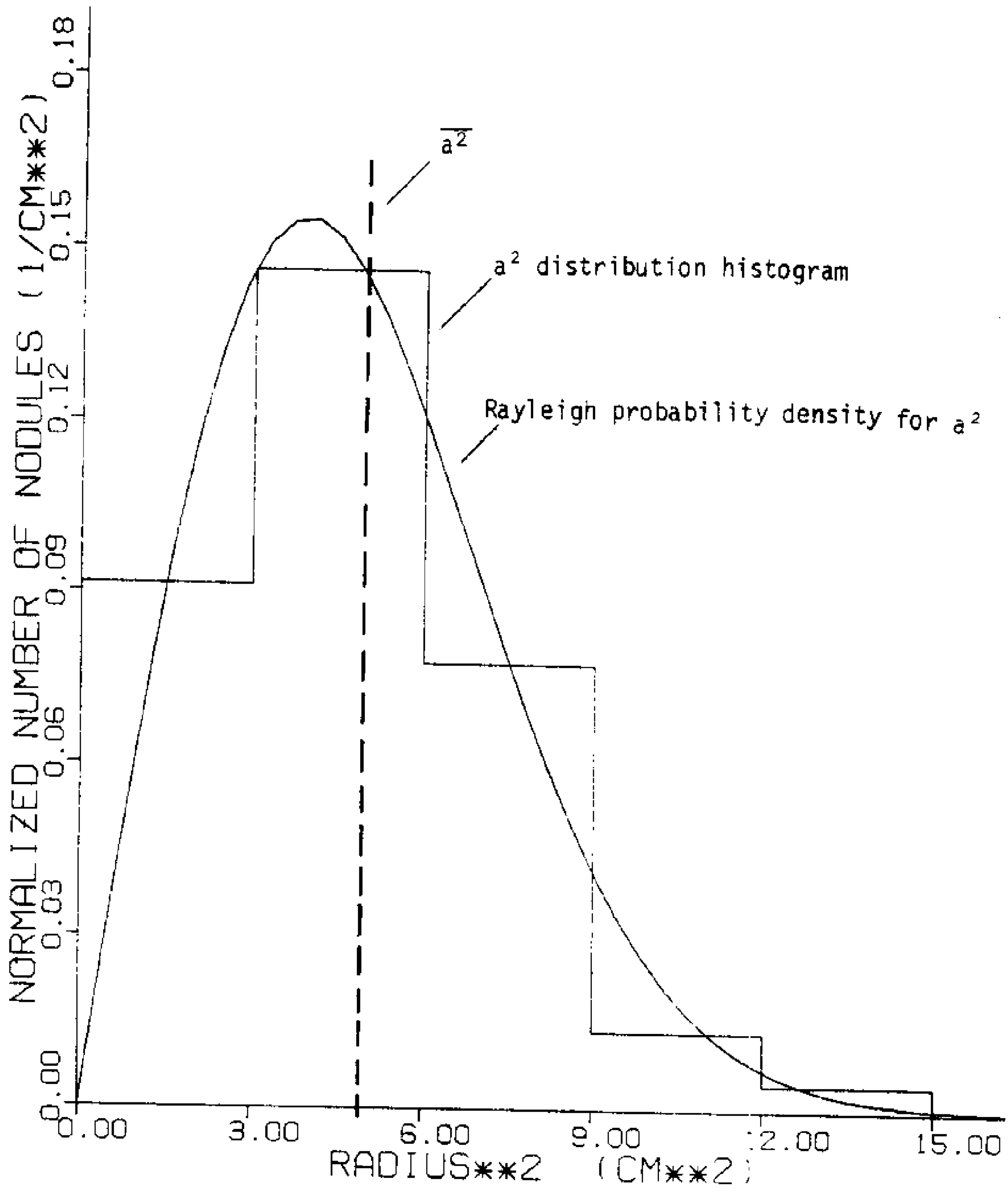

Figure 23. Size Distribution Curve Fit for Data Source 6

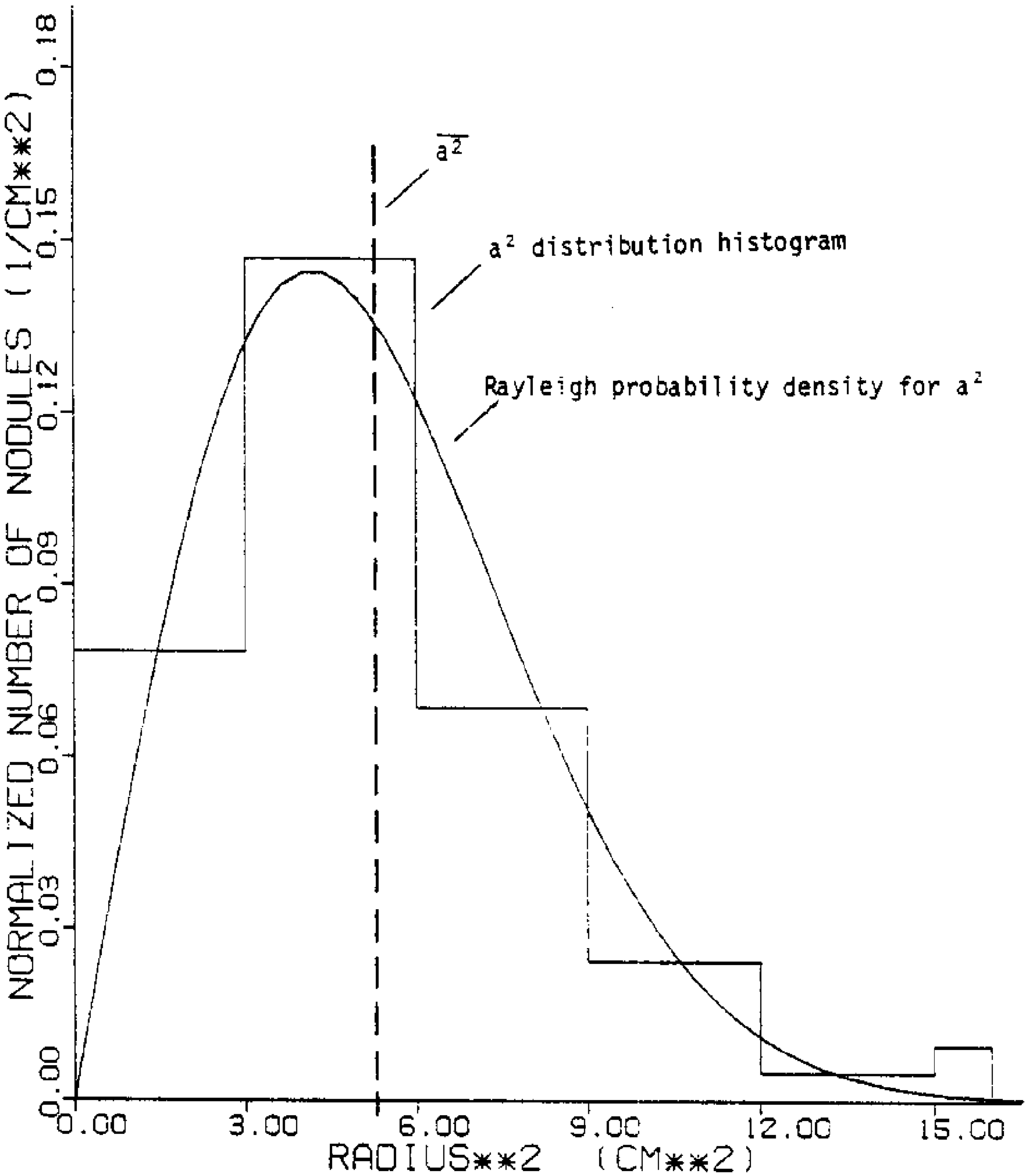

Figure 24. Size Distribution Curve Fit for Data Source 7

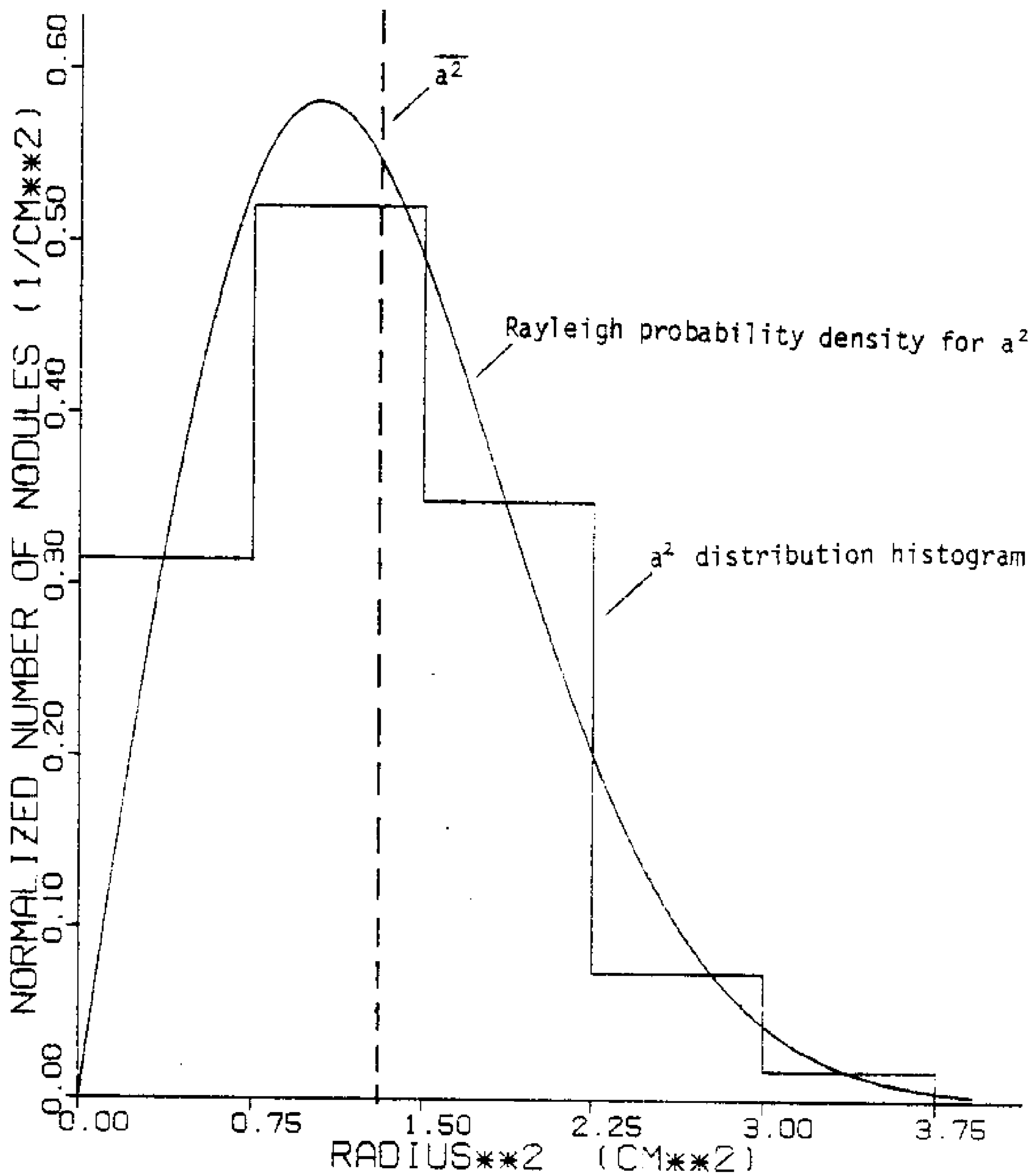

Figure 25. Size Distribution Curve Fit for Data Source 9

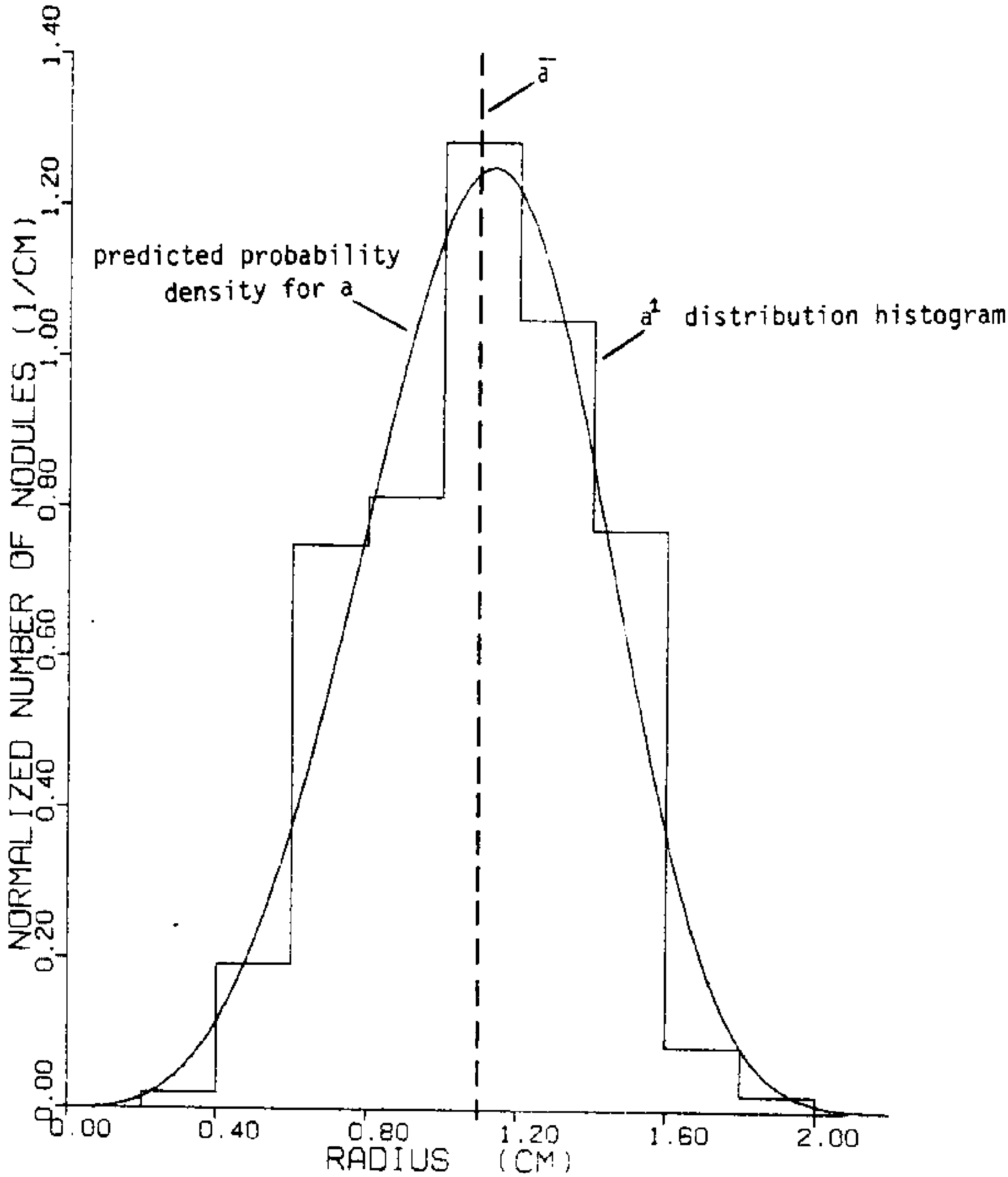

Figure 26. Size Distribution Curve Fit for Data Source 9

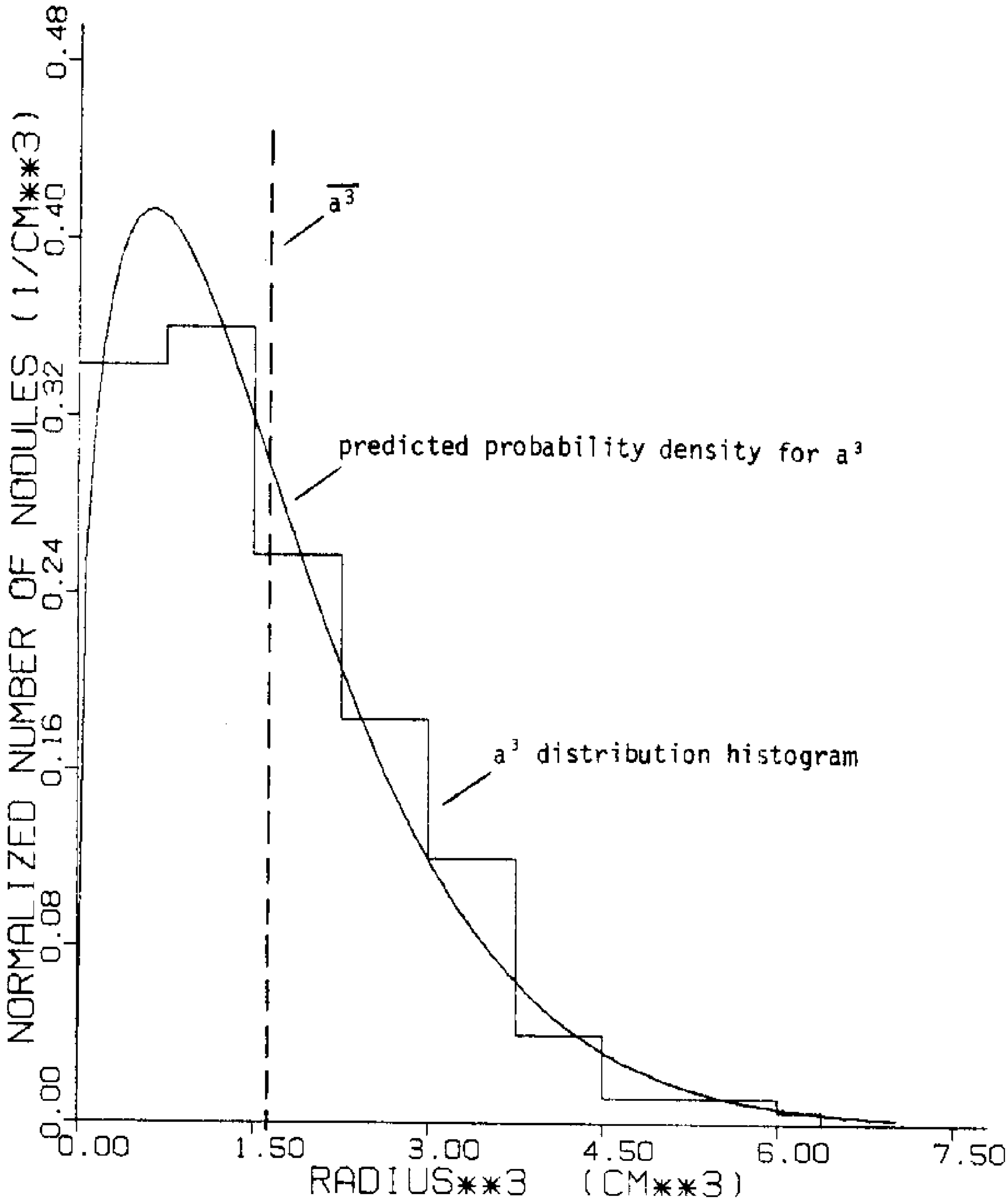

Figure 27. Size Distribution Curve Fit for Data Source 9

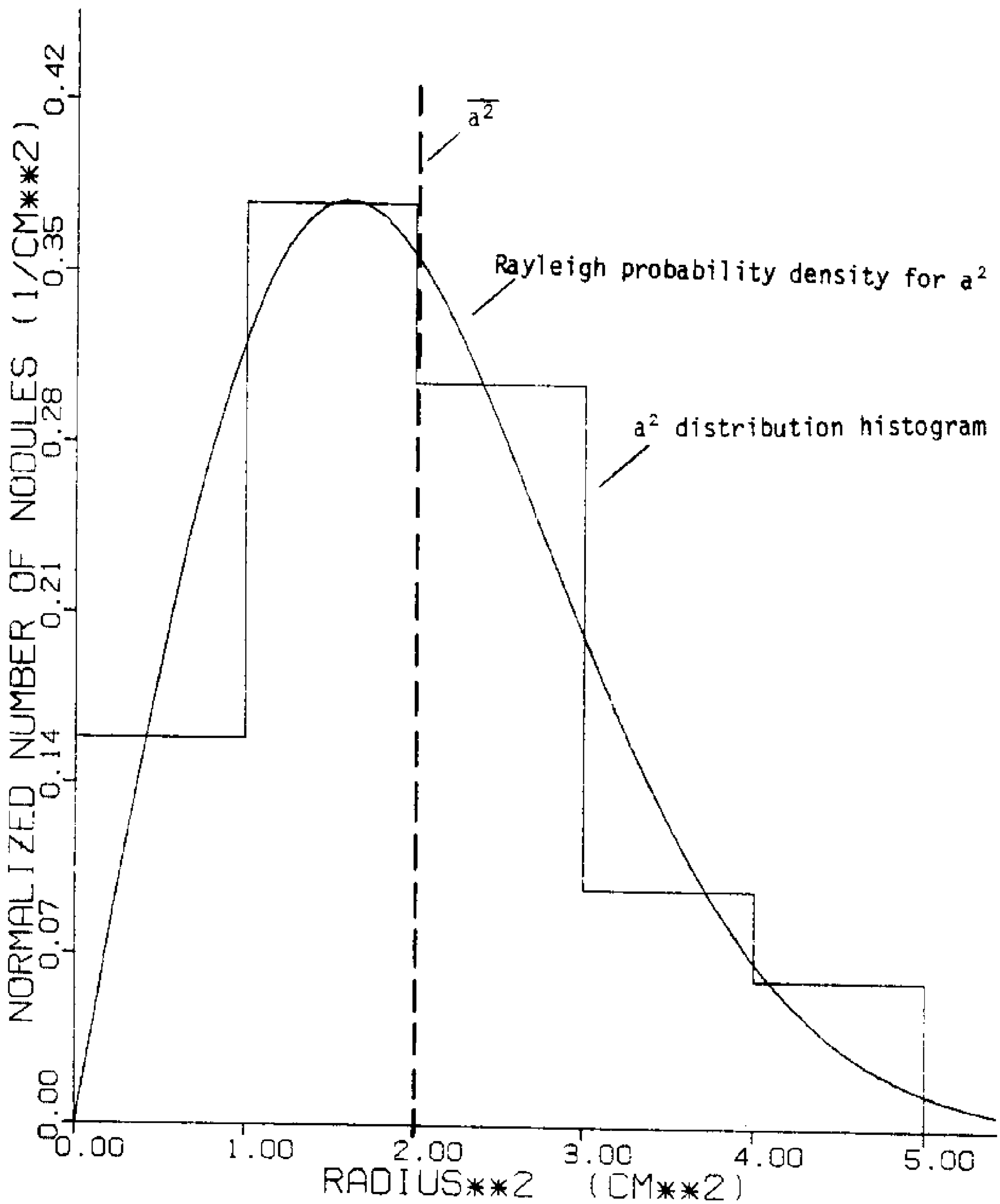

Figure 28. Size Distribution Curve Fit for Data Source 10

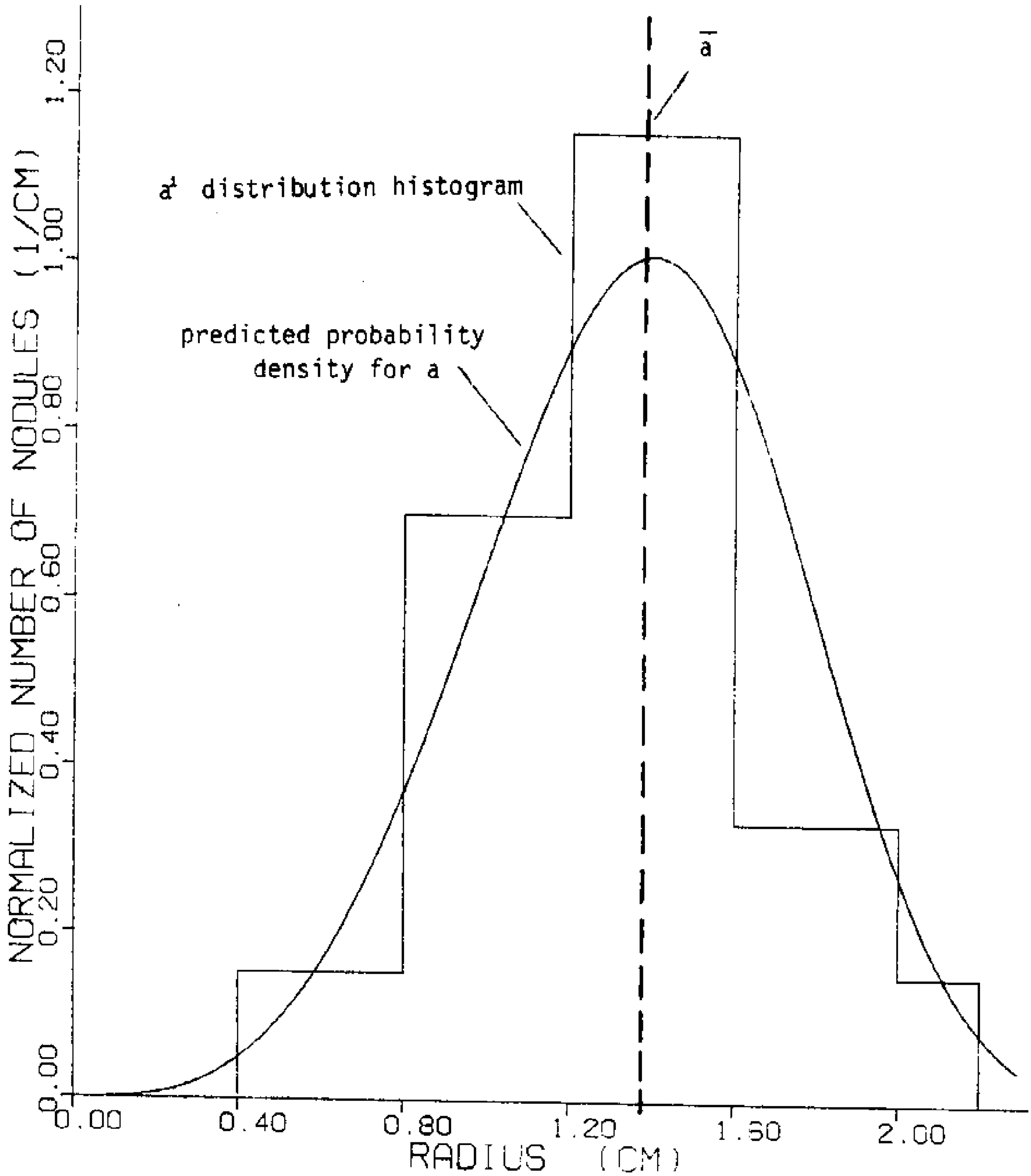

Figure 29. Size Distribution Curve Fit for Data Source 10

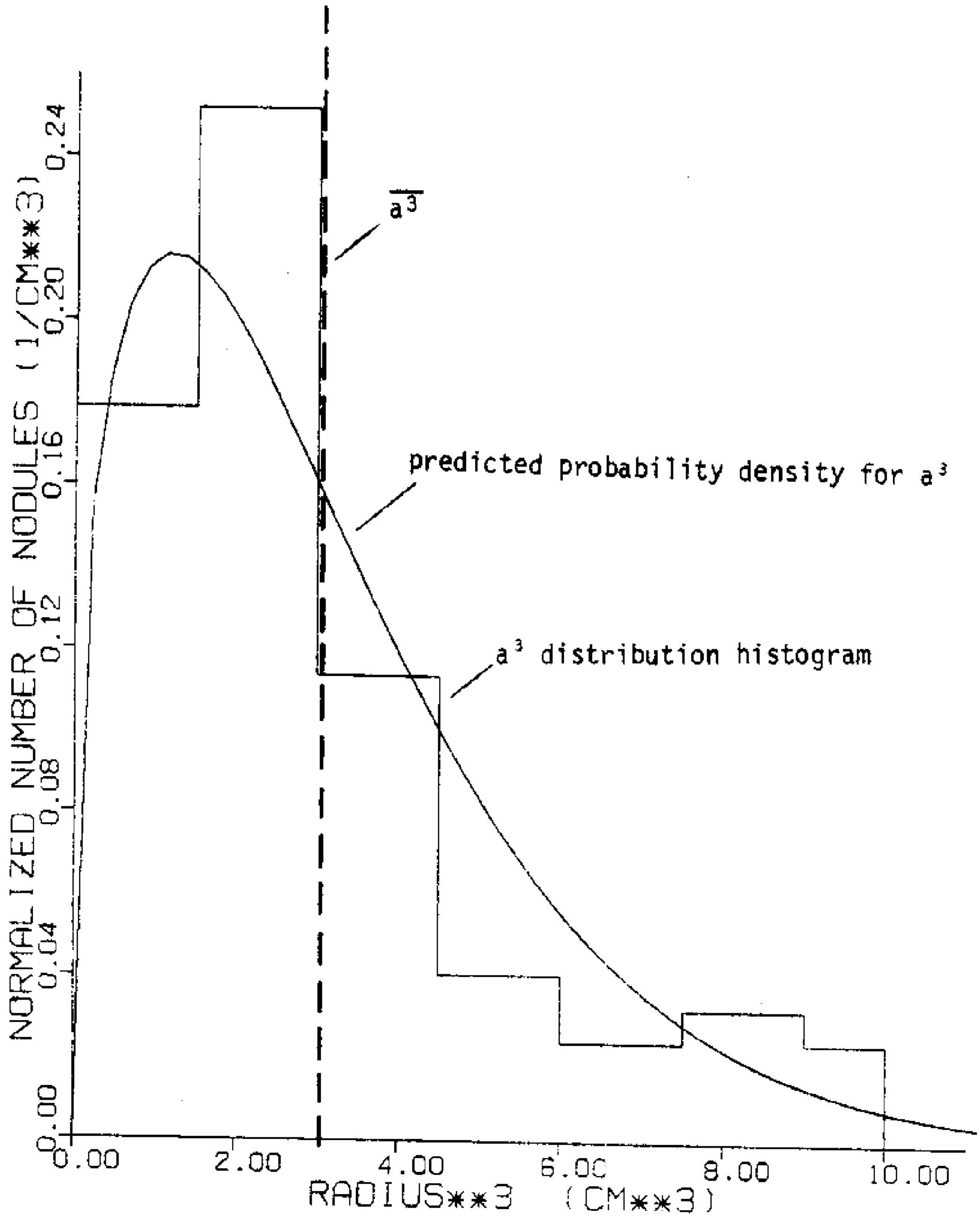

Figure 30. Size Distribution Curve Fit for Data Source 10

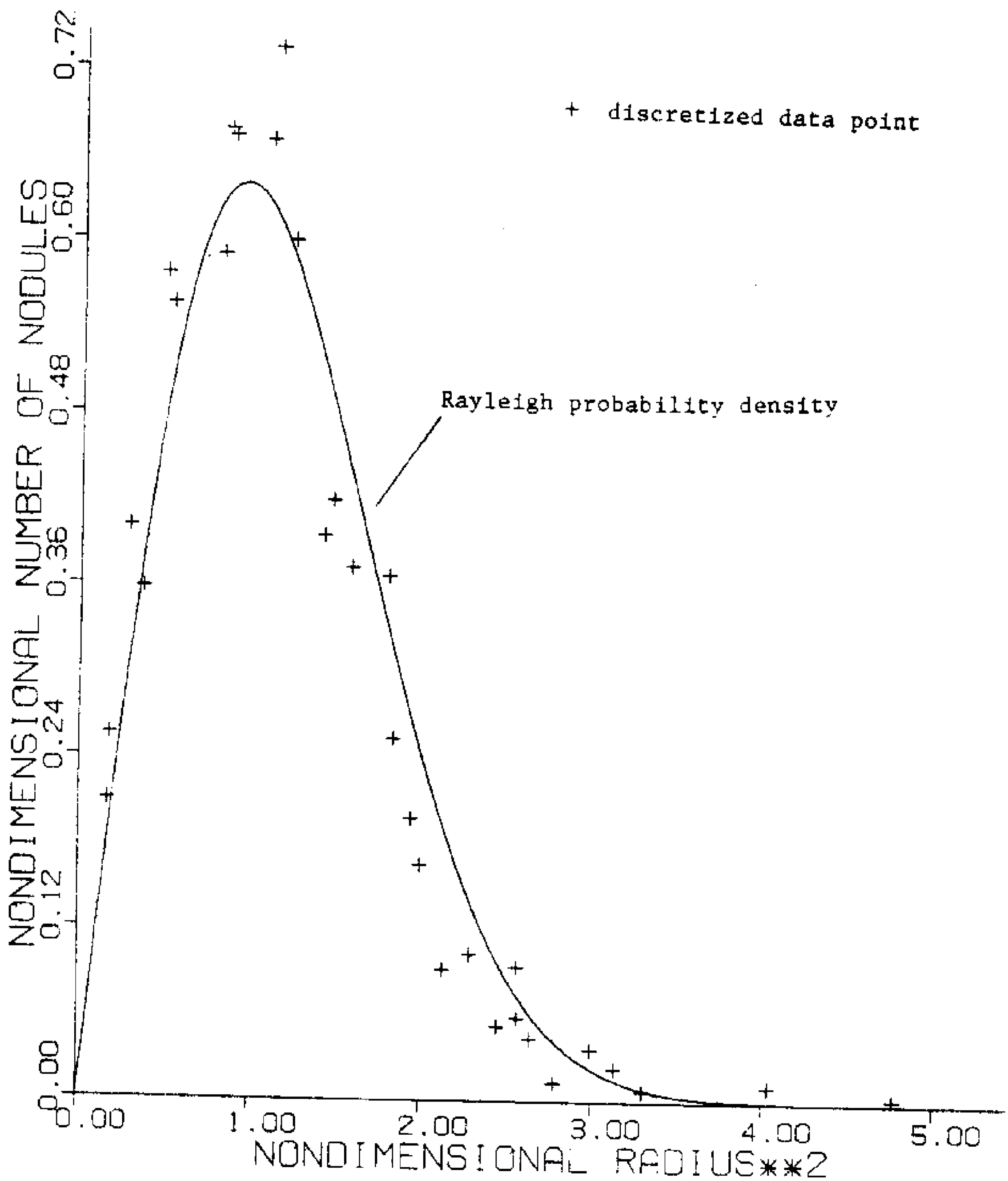

Figure 31. Nondimensional Size Distribution Curve Fit for Combined Data Sources 1a, 2, 8, and 9

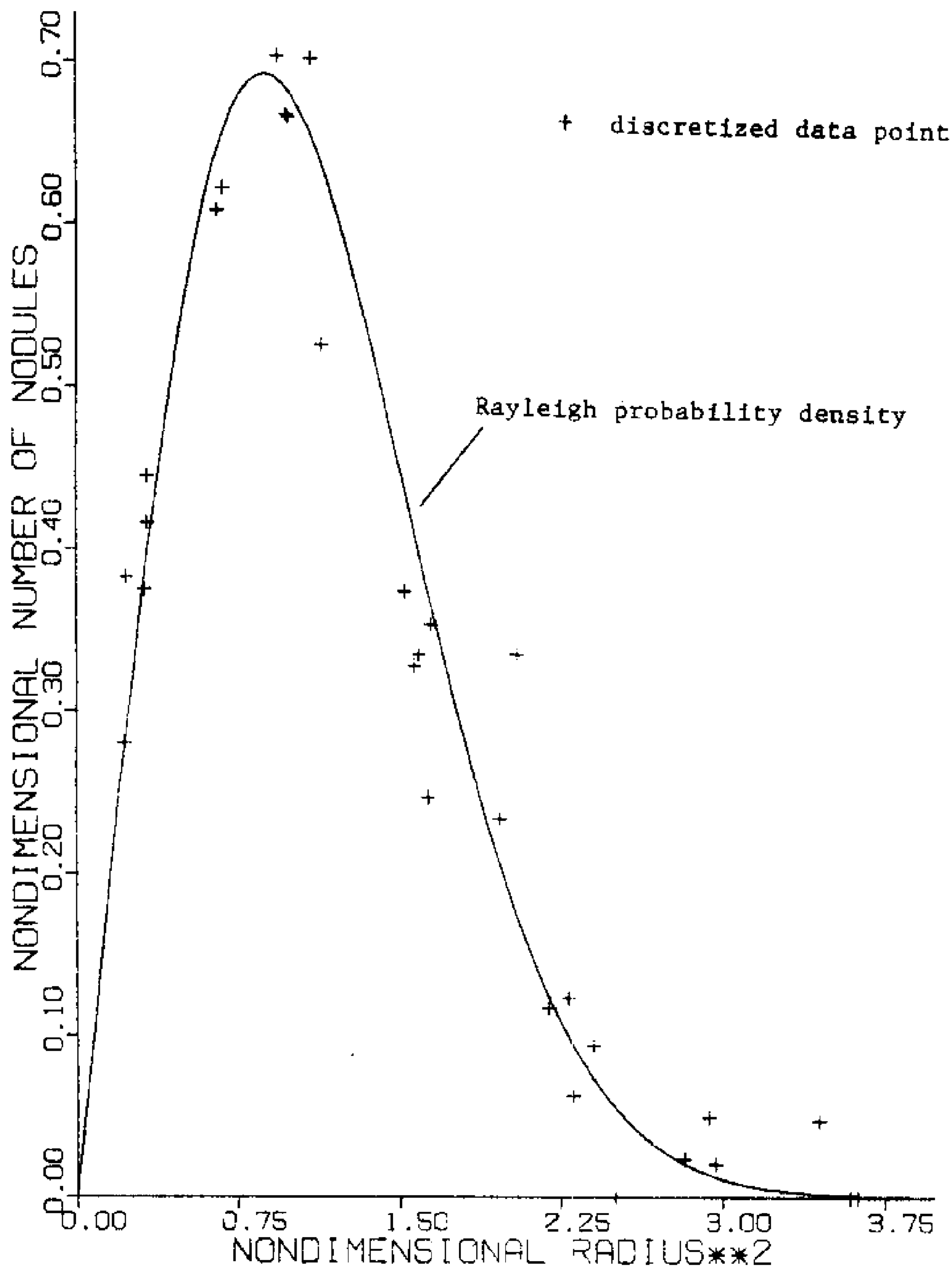

Figure 32. Nondimensional Size Distribution Curve Fit for Combined Data Sources 3, 4, 5, 6, and 7

Chapter VI

SPATIAL DISTRIBUTIONS IN MANGANESE NODULE FIELDS

In sparsely populated nodule fields, the locational relationship between any two nodules is essentially random. Nodules are spaced far enough apart so that one nodule does not impose significant locational restrictions on another.

In densely packed nodule fields, the possible location of any nodule may be appreciably inhibited by the presence of other nearby nodules. If initially, no nodule locations are known, the probability that the ith nodule is at a specific location is random. However, if a nodule is known to be at location i, the probability of the jth nodule being at a specific location is related to the ith nodule's position. The probability that the jth nodule is located in a region far away from the ith nodule is nearly random (the relative location of the ijth pair is very weakly correlated). However, if the jth nodule is located close to the ith nodule, there is a nonrandom pair correlation. Locational pair correlation is represented as the deviation from the random condition by the radial distribution function f(R).

Higher order locational statistics (conditional probabilities) are required for configurational averaging in densely packed fields. The second heirarchial equation of the Foldy-Lax series (equation 34b) considers locational correlation of nodule pairs through f(R). Therefore, for densely packed systems, equations (34a) and (34b) must be used. For sparsely packed systems, pair correlations are insignificant and the use of equation (34a) alone is sufficient.

The radial distribution function may be found in the following way. Consider one nodule at the center of a large field of nodules. If we set up enough circular rings of constant width about that nodule to encompass all other nodules in the field, and then count the number of other nodules found in each ring interval, the result is a discretized radial distribution (we shall modify this slightly when we consider the statistics of the results).

Hong (1980) numerically derived similar radial probability functions for hard spheres on a plane. His inclusion of pair statistics yields good multiple scattering results for densely packed systems. There will be no attempt to fit a curve to the radial distribution bar graph or determine an empirical distribution function as was done for the size distribution analysis. The limited use of information from the radial distribution at present does not warrant such a course. Interest lies in confirming general trends anticipated from reviewing Hong's paper.

Features of the radial probability distribution that should be emphasized are the exclusion length, the favorable location region, the shielded region, and the random probability region. The exclusion length defines the region immediately surrounding the center nodule in which very few other nodules are located. f(R) equals zero here. The random probability region refers to distant regions (far from the center nodule) and is represented by f(R) being equal to one. The favorable location region is a region of nearest neighbors, just outside of the exclusion length region, where the probability of another nodule existing, f(R), becomes greater than one. The favorable location region causes a shielding effect on the ring intervals immediately following it (going towards the distant regions). P(R) dips below the random level (1.0) in this shielded region because each nodule in the favorable location region has its own exclusion length.

6.1 DATA REDUCTION

Radial distributions are determined for photographic data sources 1 and 2. The enlarged nodule field reproductions produced for the size distribution analyses are used. The center of each reproduced nodule in the field is marked and numbered, and a Cartesian coordinate system is superimposed over the entire field. The location of the origin is unimportant. The x and y coordinates of each nodule center are then recorded using an electronic digitizer. The distance between any two nodules then is just a vector addition problem.

Just as we could vary the interval length for the size distribution, the interval size for the radial distribution is varied by using larger or smaller ring widths. Different interval sizes enhance various features of interest in the distributions. A large interval size smooths out the distribution (clearly displaying the levelling off in the far field), but it does not accurately distinguish the near field features (exclusion length, favorable region, shielding). Too small an interval size results in a very rough graph (due to using a discretized interval form to represent small data sets). A trade-off is required.

Considering one center nodule and its relationship to surrounding nodules provides too small a data set with which to work. Therefore, a group of center nodules (say 20 to 40 nodules) is utilized. Identical ring interval systems are set up around each center nodule and the number of nodules existing in corresponding ring intervals are summed. The fact that 20 center nodules are used instead of one is considered in a later normalization. This larger set of data is also more representative of the total field after averaging.

Another problem encountered involves being able to include enough intervals without running off the photographic reproduction. For a single center nodule, the intervals must extend out to at least five or six nodule diameters to be able to infer any trends in the distribution. For the single nodule in the center of a reproduction this is no problem. But, for a nodule at the outer edge of a large group of center nodules, it becomes a problem (where the intervals must extend out five or six average diameters). Considering the sizes of the reproductions and the nodules, 31 center nodules were used in data source 1, and 40 center nodules in data source 2.

6.2 CALCULATIONS

The radial distribution proposed at the beginning of this section plots number of nodules in each interval n_i against r_i, the distance from the center nodule to the interval i. In the resulting bar graph, n_i simply increases with distance from the center nodule. This occurs because as r_i increases and the interval (ring) width Δr remains constant, the area covered by each successive ring increases proportional to r. The number of nodules found in successive intervals is therefore expected to do the same. The problem is eliminated by dividing each n_i by the corresponding r_i. So, we should plot the number of nodules in each interval divided by the distance from the center nodule to the interval, n_i/r_i, against the same center nodule to interval distance, r_i.

The area of a particular ring interval A_i encircling some center nodule is

$$A_i = 2\pi r_i \Delta r \tag{75}$$

The number density $\hat{\rho}$ (number of nodules per unit area) of a random distribution may be defined as

$$\hat{\rho} = N/A \tag{76}$$

where N is the total number of nodules and A is the total bottom area in which they lie. For this random distribution we can also write

$$\hat{\rho} = n_i/A_i \tag{77}$$

where subscript i indicates some interval. Therefore, from equations (75) and (77),

$$\frac{n_i}{A_i\hat{\rho}} = \frac{n_i}{2\pi r_i \Delta r \hat{\rho}} = 1 \tag{78}$$

where this expression is written for one center nodule.

For the case of M center nodules in a random distribution, we can write

$$n_{T_i} = \sum_{j=1}^{M} n_{ij} \qquad (79)$$

where n_{T_i} is the total number of nodules in the combined interval i due to all M center nodules. We can then assume, for any one center nodule, that

$$n_i \approx \frac{n_{T_i}}{M} \qquad (80)$$

Thus, equation (78) becomes

$$1 = \frac{n_{T_i}}{2\pi r_i \Delta r \hat{\rho} M} \qquad (81)$$

We should therefore plot n_{T_i}/r_i vs. r_i. From equation (81), we see

$$\frac{n_{T_i}}{r_i} = 2\pi \Delta r \hat{\rho} M \qquad (82)$$

a constant, for a random distribution.

Near the center nodule(s) the distribution is not random - it is pair correlated. But, as one moves away from the center nodule (into the far field), the distribution becomes random, validating equation (82). The expected leveling off of the distribution should occur in the far field at a magnitude of n_{T_i}/r_i equal to $2\pi\Delta r\hat{\rho}M$. Dividing n_{T_i}/r_i for the entire field (near and far) by $2\pi\Delta r\hat{\rho}M$ gives us an expression for the radial distribution f(R), such that f(R) goes to one in the far field indicating a random distribution. Then the discretized radial distribution is expressed by

$$f(R) = \frac{n_{T_i}}{r_i} \frac{1}{2\pi\Delta r\beta M}$$

6.3 DISCUSSION OF RESULTS

Radial distributions for data sources 1 and 2 are plotted in Figures 33 and 34. Number of average diameters from the center nodule(s) is plotted along the x axis. The y axis has been normalized by equation (82). In the far field (further than 6 or 7 diameters away), the radial distribution should level off to f(R)=1.0 . The near field (within 5 diameters or so) should show the exclusion length, favorable location, and shielded regions.

A problem is encountered with data source 1 (Figure 33) in that the far field is never quite reached. The photograph of the nodule field simply was not large enough to get very far away from the center nodules.

One can see that neither distribution is very smooth. If one attempts to eyeball an average through the far field fluctuations, that average falls just short of the theoretically predicted f(R)=1. This may be the result of using too few center nodules to represent the field.

In the near field, one clearly sees an exclusion region and a sharp rise representing the favorable location region. Immediately following the rise, one sees the shielded region as a low dip. Note in Figure 34 that this rise-dip pattern apparently repeats itself several times before being lost in the fluctuations. This indicates that secondary and tertiary favorable locations and associated shielding effects may be present.

For data source 2 (Figure 34), the exclusion length is at least 1.5 average diameters. The largest concentration of other nodules occurs at a distance of 2 to 3 average nodule diameters.

Data source 1 (Figure 33) shows the shortcomings of this approach. According to the plot here, the minimum exclusion length is one average radius. For a field of uniformly sized nodules, the minimum exclusion length would have to be at least one diameter (the distance between nodule centers for nodule sides touching). However, nodule fields are not uniform. We must deal with an average nodule radius (averaged over the field). Some smaller nodules may be closer together than other nodules so that the distance between their centers is less than the field averaged diameter. In the case of Figure 33, four center nodules were much smaller than average and were located very near each other. Hence, the low exclusion length. Realizing this point, one can eyeball an exclusion length between .75 and 1.25 average diameters and the largest concentration of other nodules at 1.25 to 1.75 diameter's distance.

The quantitative information found above (exclusion lengths and favorable distances) may be used to evaluate the integral in equation (34b) for a typical nodule field in order to ascertain the importance of the pair correlation.

6.4 FURTHER INVESTIGATION

It has been shown that the expected exclusion, favorable location, and shielded regions for pair correlated radial distributions do exist in manganese nodule fields. The importance of these features in the scattering analysis and the expression of the distribution function in terms of these features should be studied next. The exclusion length is expected to increase, and the magnitude of the favorable location probability is expected to flatten out (towards f(R)=1) with decreasing nodule population density. These relationships should also be examined.

So, future examination of locational distributions should look into the following topics.

1) Effect of a typical radial distribution function on the multiple scattering analysis. Must it be included and can the function be expressed in a simplified manner?

2) Variation of near field features of the radial distribution function with changes in nodule number density. Is the variation significant over the range of densities for practical mining interests?

3) Variation of radial distribution function with number density change for large bottom areas (on

the order of $10,000m^2$) as opposed to the very small data sets used for this analysis (on the order of $1m^2$).

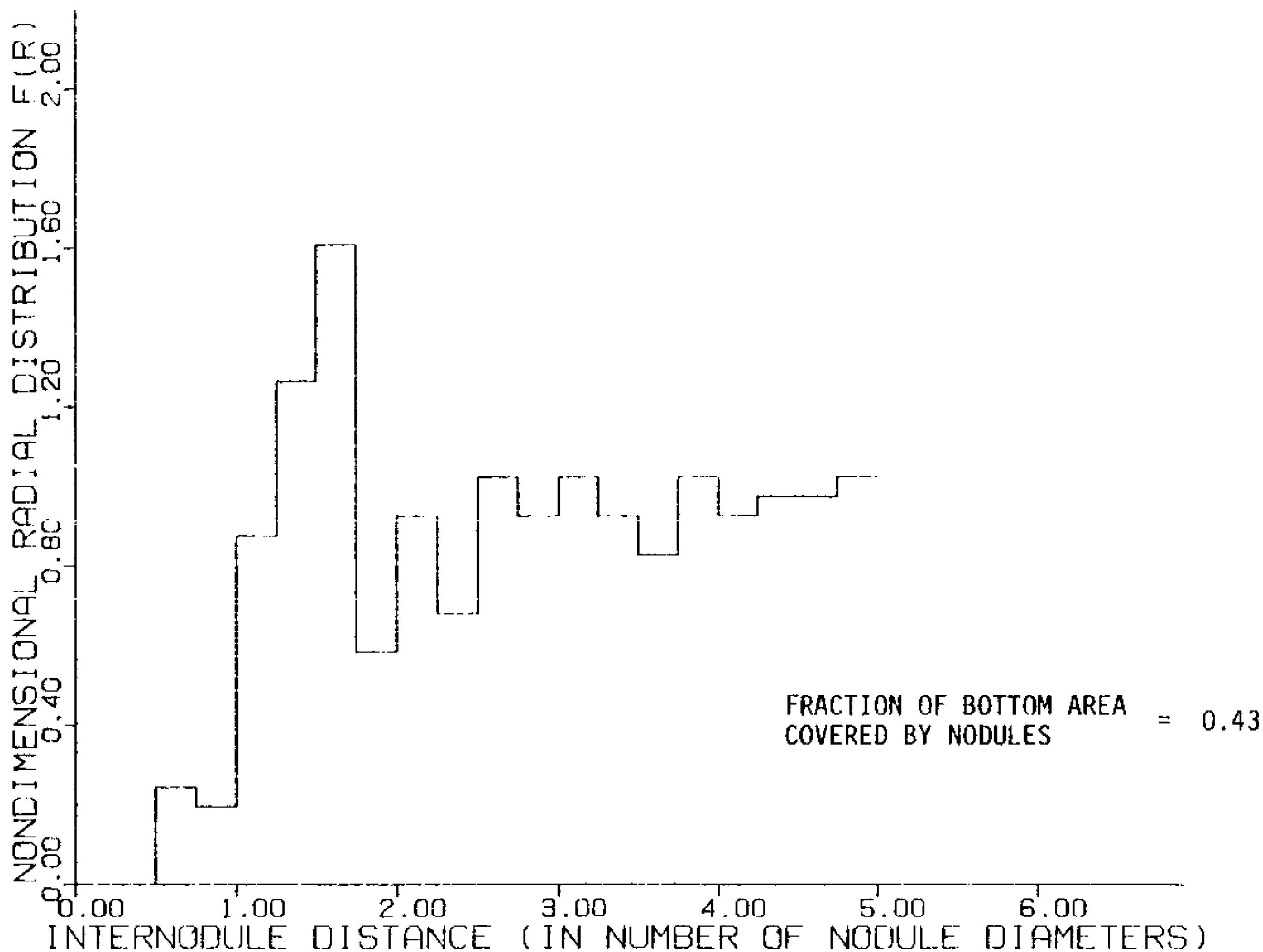

Figure 33. Radial Distribution Histogram for Data Source 1a

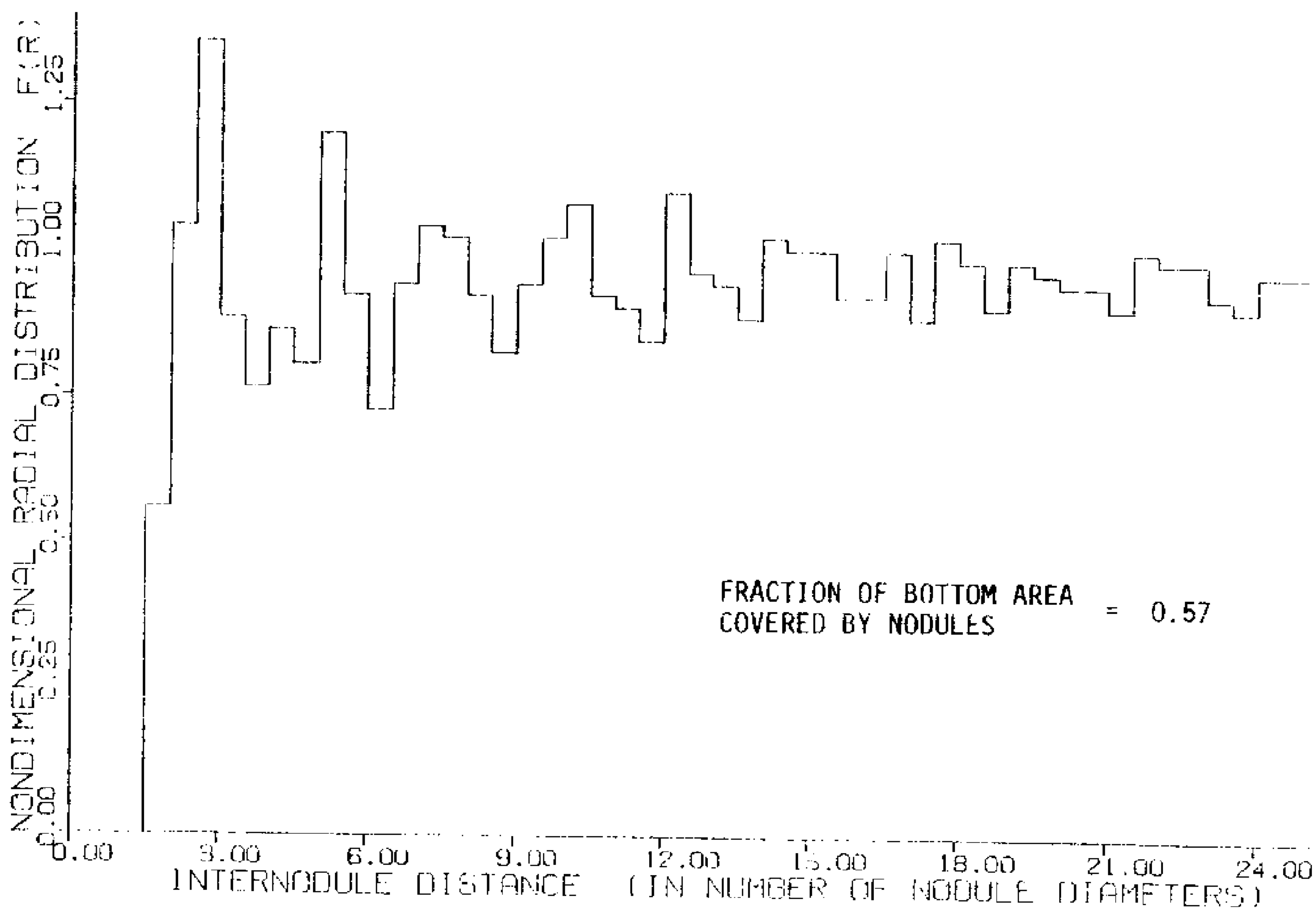

Figure 34. Radial Distribution Histogram for Data Source 2

Chapter VII

SUMMARY OF CONCLUSIONS

This thesis has experimentally examined three topics fundamental to the theoretical analysis of acoustical scattering from manganese nodule fields for the purpose of obtaining quantitative results from the theory. The three areas of interest are acoustical properties of manganese nodules, size distributions and spatial distributions in manganese nodule fields.

To quantitatively evaluate the scattered response of an acoustically excited manganese nodule, longitudinal and transverse wave speeds were measured in Pacific and Atlantic nodules. The major results are listed in Table 1. Average longitudinal wave speeds were found to be 2350m/s for the Pacific nodules and 2605m/s for the Atlantic nodules. Average transverse wave speeds were found to be between 2000 and 2050m/s for both the Pacific and the Atlantic nodules.

These measurements were performed under atmospheric pressures on nodules that had been saturated in fresh water. It is suggested that further measurements be performed under assimilated in situ conditions. This would require that the nodules remain in sea water after recovery from the ocean bottom, and also, that the measurements be performed in a pressure chamber capable of ocean deep pressures.

Examination of the distribution of nodule cross-sectional sizes in ocean bottom photographs reveals that the nodule radius squared distribution is described by the Rayleigh probability function. This function is given by equation (56) as

$$q(x) = \frac{x}{b^2}\, e^{\frac{-x^2}{2b^2}}$$

where x equals the nodule cross-sectional radius squared, and b is a function of the average square radius. Through some statistical manipulations, probability functions for other powers of the radius can be written, and averages of the radius to various powers can be related through the parameter b in the above equation. This latter capability is necessary when attempting to recover specific average powers of the radius, such as $\overline{a^3}$ (a measure of the average nodule volume), from any $\overline{a^n}$ that falls out of the Foldy-Lax equations (34a) and (34b).

Another important result of this analysis is the ability to size average any function of the radius, fn(a), over a field of nodules. This allows size averaging of an individual nodule scattering strength (as given by equation 20a, for example) over a nodule field, which results in an average field scattering strength (equation 48) for use in evaluating the Foldy-Lax equations. The size average of fn(a) is given by

$$\overline{fn(a)} = \int da\ 2\ \frac{a^3}{b^2}\ e^{\frac{-a^4}{2b^2}}\ fn(a)$$

Note that the predicted radius probability function is used here instead of the experimentally determined radius squared probability function.

Further investigation into the mass - radius relationship may be required because Pacific nodules are not spherical as assumed for this size distribution analysis. Also, the effect of nonspherical nodules in the scattering theory has not been considered.

Analysis of the locational distribution of nodules on the ocean bottom shows that several pair correlated features exist and may be important in the scattering theory when applied to densely populated nodule fields. Far away from some center nodule, the probability of finding nodules at a particular distance from the center nodule becomes a constant. This is a result of the random distribution of nodule locations in the far field. The probability function, f(R), is represented by the number of nodules, at some distance from the center nodule, divided by that distance. In the near field, however, nodule locations are correlated. Around any nodule there exists an exclusion region (in which no other nodule may be located), a favorable location region (in which the probability of finding other nodules is greater than the far field random probability), and finally, a shielded region (in which the probability of finding other nodules is less than that for the far field). The shielded region is caused by the exclusion lengths of nodules in the favorable location region.

Future examination of locational distributions should look into the following topics. How are the near field features (primarily the exclusion length and favorable location regions) related to the nodule number density δ? How significant is f(R) on the multiple scattering analysis and can a simplified expression for f(R) be employed? What is the effect of examining a very large bottom area (on the order of $10{,}000 m^2$) on the radial distribution function?

Appendix A

ACOUSTICAL PROPERTIES OF MANGANESE NODULES

Measured Wave Speeds for Pacific Ocean Manganese Nodules in Wet and Dry Conditions

NODULE SAMPLE ID	C_L wet m/s	C_T wet m/s	C_L dry m/s	C_T dry m/s	C_T/C_L wet
P1	–	1960 to 2078	1117 to 1343	–	–
P2	2274 to 2352	1940 to 2156	1852	1519 to 1764	0.85 to 0.92
P3	–	–	1529 to 1588	1186	–
P5	2558 to 2695	2391 to 2636	1705 to 1823	1607 to 1637	0.93 to 0.98
P6	1989 to 2156	1705 to 2058	1539 to 1646	1450 to 1470	0.86 to 0.95
P7	2607 to 2675	2450	1862 to 1980	1558 to 1747	0.93
P8	2323 to 2519	–	1578 to 1646	1372	–
P9	1950 to 2117	1617 to 1784	1950 to 1989	1617	0.83 to 0.84

Measured Densities and Porosities for Pacific Ocean Manganese Nodules

NODULE SAMPLE ID	WET DENSITY g/cm³	DRY DENSITY g/cm³	SOLID MATERIAL DENSITY g/cm³	WET MASS g	DRY MASS g	VOLUME cm³	POROSITY %
P1	1.99	1.47	3.05	38.8	28.7	19.5	51.8
P2	1.91	1.41	2.82	47.9	35.3	25.1	50.2
P3	1.99	1.48	3.05	70.8	52.5	35.5	51.5
P5	1.96	1.42	3.07	19.4	14.1	9.9	53.5
P6	—	1.35	—	—	32.3	23.9	—
P7	1.95	1.42	3.00	28.4	20.7	14.6	52.7
P8	—	—	—	—	12.2	—	—
P9	2.13	1.59	3.47	25.6	19.1	12.0	54.2

Measured Wave Speeds for Atlantic Ocean Manganese
Nodules in Wet and Dry Conditions

NODULE SAMPLE ID	C_L wet m/s	C_T wet m/s	C_L dry m/s	C_T dry m/s	C_T/C_L wet
A1	3038 to 3214	2274 to 2577	2548	2195	0.75 to 0.80
A2	2362 to 2391	1627 to 1754	1891	1842	0.69 to 0.73
A3	2450 to 2646	1744 to 1911	2646 to 2744	1411	0.71 to 0.72
A4	2127 to 2205	–	1695	–	–
CH58	1940	784 to 823	1490	862	–
DR15	1578 to 1705	–	1352	843	–

Measured Densities and Porosities for Atlantic Ocean Manganese Nodules

NODULE SAMPLE ID	WET DENSITY g/cm^3	DRY DENSITY g/cm^3	SOLID MATERIAL DENSITY g/cm^3	WET MASS g	DRY MASS g	VOLUME cm^3	POROSITY %
A1	2.07	1.59	3.04	355.6	273.2	172.2	47.8
A2	1.89	1.31	3.08	255.9	177.9	135.7	57.5
A3	1.97	1.45	3.03	276.8	203.7	140.3	52.1
A4	1.99	1.46	3.13	314.6	230.0	158.0	53.5
CH58	1.82	1.26	2.86	140.2	97.1	77.0	56.0
DR15	1.80	1.21	2.95	202.6	136.4	112.5	58.9

Appendix B

DATA SOURCES LIST AND DATA FOR SIZE DISTRIBUTION ANALYSIS

This appendix contains the sources of data utilized for the size distribution analysis and for the spatial distribution analysis. Also included, are data tables which present the discretized size distribution from each data source used to produce the histograms in Figures 9 through 30. Lastly, a table of average radius functions derived from each data source is included.

LIST OF DATA SOURCES

Data source 1a, 1b, and 1c

Bottom photograph of Pacific nodule field obtained from Deepsea Ventures, Inc. 1a refers to the entire photograph. 1b and 1c refer to contiguous portions that make up 1a.

Data source 2

Bottom photograph of Pacific nodule field obtained from Deepsea Ventures, Inc.

Data sources 3 - 8

Physical characteristics tables of central Pacific nodule sites (DOMES site C) compiled by Fewkes et al. (1979). Data sources are from camera run 1, frame numbers as follows:

3 No. 264

4 No. 266

5 No. 269

6 No. 271

7 No. 273

8 All five frames combined

Note that the distance between adjacent frames (e.g. No. 264 to No. 265) is about 20 feet.

Data source 9

Physical characteristics tables of central Pacific nodule sites (DOMES site A) compiled by Fewkes et al. (1980). Data source 9 is a combination of data from camera run 1, frame numbers 167, 170, 189, 232, 253, 349, 393, 522, and 538.

Data source 10

Physical characteristics tables of central Pacific nodule site (DOMES site A) compiled by Fewkes et al. (1980). Data is from camera run 3, frame number 464.

Discretized Size Distribution Information for
Data Sources 1a, 1b, and 1c

CROSS SECTIONAL AREA INTERVAL (cm^2)	NUMBER OF NODULES FOR DATA SOURCES		
	1c	1b	1a
0 - 2.4	3	5	8
2.4 - 4.9	5	4	9
4.9 - 7.3	7	11	18
7.3 - 9.7	4	7	11
9.7 - 12.2	7	12	19
12.2 - 14.6	8	16	24
14.6 - 17.0	10	12	22
17.0 - 19.5	9	16	25
19.5 - 21.9	11	19	30
21.9 - 24.3	7	14	21
24.3 - 26.8	8	8	16
26.8 - 29.2	4	10	14
29.2 - 31.6	10	13	23
31.6 - 34.1	9	14	23
34.1 - 36.5	8	14	22
36.5 - 39.0	8	10	18
39.0 - 41.4	3	4	7
41.4 - 43.8	3	8	11
43.8 - 46.3	3	12	15
46.3 - 48.7	2	4	6
48.7 - 51.1	1	6	7
51.1 - 53.6	3	3	6
53.6 - 56.0	2	6	8
56.0 - 58.4	0	4	4
58.4 - 60.9	1	3	4
60.9 - 63.3	1	1	2
63.3 - 65.7	1	3	4
65.7 - 68.2	0	2	2
68.2 - 70.6	1	1	2
70.6 - 73.0	1	1	2
73.0 - 75.5	1	2	3
75.5 - 77.9	0	1	1
77.9 - 80.3	1	0	1

Discretized Size Distribution Information for Data Source 2

CROSS SECTIONAL AREA INTERVAL (cm^2)	NUMBER OF NODULES
0 - 0.6	21
0.6 - 1.3	35
1.3 - 1.9	36
1.9 - 2.6	37
2.6 - 3.2	61
3.2 - 3.9	46
3.9 - 4.5	28
4.5 - 5.2	28
5.2 - 5.8	14
5.8 - 6.5	12
6.5 - 7.1	11
7.1 - 7.7	6
7.7 - 8.4	2
8.4 - 9.0	3
9.0 - 9.7	4
9.7 - 10.3	1
10.3 - 11.0	1
11.0 - 11.6	0
11.6 - 12.3	0
12.3 - 12.9	1
12.9 - 13.5	2
13.5 - 14.2	0
14.2 - 14.8	0
14.8 - 15.5	1

Discretized Size Distribution Information for
Data Sources 3 through 8

CROSS SECTIONAL AREA INTERVAL (cm^2)	NUMBER OF NODULES FOR DATA SOURCES					
	3	4	5	6	7	8
0 - 1	1	2	0	1	1	5
1 - 2	0	0	1	0	0	1
2 - 3	0	2	0	2	1	5
3 - 4	0	2	1	1	1	5
4 - 5	1	2	1	1	3	8
5 - 6	0	0	0	5	4	9
6 - 7	1	1	1	2	4	9
7 - 8	1	2	1	4	2	10
8 - 9	4	7	1	4	0	16
9 - 10	0	2	2	4	3	11
10 - 11	0	1	1	1	2	5
11 - 12	1	5	1	3	6	16
12 - 13	3	3	0	5	3	14
13 - 14	5	2	2	3	2	14
14 - 15	2	5	1	2	7	17
15 - 16	0	2	2	8	3	15
16 - 17	1	5	3	2	3	14
17 - 18	1	2	1	4	1	9
18 - 19	1	2	1	1	3	8
19 - 20	0	0	2	1	3	6
20 - 21	2	0	1	1	0	4
21 - 22	1	2	4	1	2	10
22 - 23	1	1	1	3	2	8
23 - 24	3	1	1	2	1	8
24 - 25	1	1	0	3	1	6
25 - 26	1	0	1	1	1	4
26 - 27	0	0	1	3	0	4
27 - 28	1	3	3	1	1	9
28 - 29	0	0	1	1	0	2
29 - 30	2	0	1	0	1	4

Discretized Size Distribution Information for
Data Sources 3 through 8 (con't)

CROSS SECTIONAL AREA INTERVAL (cm^2)	NUMBER OF NODULES FOR DATA SOURCES					
	3	4	5	6	7	8
30 - 31	1	1	0	2	0	4
31 - 32	0	1	2	0	1	4
32 - 33	2	1	0	0	0	3
33 - 34	0	1	1	0	0	2
34 - 35	0	1	1	0	1	3
35 - 36	0	0	2	0	1	3
36 - 37	2	0	0	0	1	3
37 - 38	1	0	2	1	0	4
38 - 39	0	0	1		1	2
39 - 40	0	0	0		0	0
40 - 41	0	0	0		0	0
41 - 42	0	0	0		0	0
42 - 43	1	0	1		0	2
43 - 44	2	2	0		0	4
44 - 45	1		0		0	1
45 - 46	1		0		0	1
46 - 47	1		1		0	2
47 - 48			0		0	0
48 - 49			1		2	3
49 - 50			1			1

Discretized Size Distribution Information for
Data Source 9

CROSS SECTIONAL AREA INTERVAL (cm^2)	NUMBER OF NODULES	CROSS SECTIONAL AREA INTERVAL (cm^2)	NUMBER OF NODULES
0 - 0.2	0	6.0 - 6.2	1
0.2 - 0.4	1	6.2 - 6.4	7
0.4 - 0.6	2	6.4 - 6.6	7
0.6 - 0.8	3	6.6 - 6.8	5
0.8 - 1.0	4	6.8 - 7.0	5
1.0 - 1.2	6	7.0 - 7.2	2
1.2 - 1.4	4	7.2 - 7.4	2
1.4 - 1.6	11	7.4 - 7.6	6
1.6 - 1.8	3	7.6 - 7.8	1
1.8 - 2.0	11	7.8 - 8.0	0
2.0 - 2.2	10	8.0 - 8.2	0
2.2 - 2.4	5	8.2 - 8.4	0
2.4 - 2.6	6	8.4 - 8.6	0
2.6 - 2.8	6	8.6 - 8.8	0
2.8 - 3.0	11	8.8 - 9.0	0
3.0 - 3.2	6	9.0 - 9.2	1
3.2 - 3.4	5	9.2 - 9.4	1
3.4 - 3.6	11	9.4 - 9.6	1
3.6 - 3.8	5	9.6 - 9.8	0
3.8 - 4.0	13	9.8 - 10.0	1
4.0 - 4.2	11	10.0 - 10.2	0
4.2 - 4.4	9	10.2 - 10.4	0
4.4 - 4.6	3	10.4 - 10.6	0
4.6 - 4.8	5	10.6 - 10.8	0
4.8 - 5.0	10	10.8 - 11.0	0
5.0 - 5.2	7	11.0 - 11.2	1
5.2 - 5.4	6		
5.4 - 5.6	8		
5.6 - 5.8	3		
5.8 - 6.0	7		

Discretized Size Distribution Information for
Data Source 10

CROSS SECTIONAL AREA INTERVAL (cm^2)	NUMBER OF NODULES
0 - 0.5	0
0.5 - 1.0	0
1.0 - 1.5	3
1.5 - 2.0	2
2.0 - 2.5	5
2.5 - 3.0	3
3.0 - 3.5	8
3.5 - 4.0	1
4.0 - 4.5	6
4.5 - 5.0	5
5.0 - 5.5	8
5.5 - 6.0	3
6.0 - 6.5	9
6.5 - 7.0	3
7.0 - 7.5	4
7.5 - 8.0	6
8.0 - 8.5	1
8.5 - 9.0	2
9.0 - 9.5	1
9.5 - 10.0	2
10.0 - 10.5	2
10.5 - 11.0	1
11.0 - 11.5	0
11.5 - 12.0	0
12.0 - 12.5	2
12.5 - 13.0	1
13.0 - 13.5	1
13.5 - 14.0	1
14.0 - 14.5	2

Measured Average Radius Functions

DATA SOURCE	$\overline{a}$ (cm)	$\overline{a^2}$ (cm^2)	$\overline{a^3}$ (cm^3)	$\overline{a^6}$ (cm^6)
1a	2.9	9.3	31.7	1670
1b	3.0	9.6	32.9	1770
1c	2.8	8.8	29.5	1490
2*	1.0	1.2	1.5	4.2
3	2.6	7.1	21.4	730
4	2.1	5.1	13.0	305
5	2.6	7.4	22.2	750
6	2.1	4.9	11.9	220
7	2.2	5.2	13.6	350
8	2.3	5.8	15.7	435
9	1.1	1.3	1.6	4.0
10	1.4	2.0	3.1	15

* unscaled data

Appendix C

DATA FOR SPATIAL DISTRIBUTIONS IN MANGANESE NODULE FIELDS

Radial Distribution Data for Figure 33
(from Data Source 1b)

Number of center nodules used - 31
Total number of nodules used - 247
Interval width equals one half the average radius

Interval Number	Number of Nodules / Distance to Center
1	0.0
2	0.0
3	5.3
4	3.8
5	17.8
6	26.1
7	33.3
8	12.4
9	18.8
10	13.7
11	21.0
12	19.1
13	20.8
14	19.3
15	16.6
16	21.1
17	19.2
18	19.6
19	20.0
20	21.0

Radial Distribution Data for Figure 34
(from Data Source 2)

Number of center nodules used - 40
Total number of nodules used - 764
Interval width equals one average radius

Interval Number	Number of Nodules / Distance to Center	Interval Number	Number of Nodules / Distance to Center
1	0.0	26	48.6
2	0.0	27	47.9
3	0.0	28	44.7
4	28.6	29	51.8
5	53.3	30	50.7
6	69.1	31	50.8
7	45.4	32	46.8
8	39.3	33	47.4
9	43.5	34	50.6
10	40.5	35	44.8
11	61.0	36	51.7
12	47.0	37	49.6
13	36.8	38	45.6
14	48.2	39	50.0
15	53.1	40	48.9
16	51.9	41	47.9
17	46.7	42	48.3
18	41.7	43	46.5
19	48.1	44	50.9
20	52.3		
21	55.4		
22	47.4		
23	46.0		
24	43.4		
25	55.5		

REFERENCES

Clay, C. S. and H. Medwin. 1977. Acoustical Oceanography: Principles and Applications, John Wiley & Sons, New York.

Davenport, W. B. and W. L. Root. 1958. Random Signals and Noise. McGraw-Hill Book Company, Inc., New York.

Fewkes, R. H., W. D. McFarland, W. R. Reinhart and R. K. Sorem. 1979. Development of a Reliable Method for Evaluation of Deep Sea Manganese Nodule Deposits. Final Report. Contract No. G-0274013-MAS, prepared for United States Department of the Interior Bureau of Mines, by Department of Geology, Washington State University.

Fewkes, R. H., W. D. McFarland, W. R. Reinhart and R. K. Sorem. 1980. Evaluation of Metal resources at and Near Proposed Deep Sea Mine Sites. Final Report. Grant No. G-284008-MAS, prepared for United States Department of the Interior Bureau of Mines, by Department of Geology, Washington State University.

Foldy, L. L. 1945. 'The Multiple Scattering of Waves', Phys. Rev. 67 (2), pp. 107-119.

Frazer, J. E. 1977. 'Manganese Nodule Reserves: An Updated Estimate', in Marine Mining, ed. Moore, J. R., Crane, Russak & Company, Inc., New York, Vol. I, p. 125.

Gladsby, G. P.(ed.). 1977. Marine Manganese Deposits. Elsevier Oceanography Series 15. Amsterdam, p. 359.

Greenslate, J. 1977. 'Manganese Concentration Wet Density: A Marine Geochemistry Constant', in Marine Mining, ed. Moore, J. R., Crane, Russak & Company, Inc., New York, Vol. I, p. 125.

Hong, K. M. 1980. 'Multiple Scattering of Electromagnetic Waves by a Crowded Monolayer of Spheres: Application to Migration Imaging Films', J. Opt. Soc. Am. 70 (7), pp. 821-826.

Lax, M. 1951. 'Multiple Scattering of Waves. II. The Effective Field in Dense Systems', Phys. Rev. 85 (4), pp. 621-629.

Ma, Y. and A. H. Magnuson. 1981. Acoustic Scattering from a Single Manganes Nodule, Technical Report, Dept. of Aerospace and Ocean Engineering, Virginia Polytechnic Institute and State University.

Magnuson, A. H. and K. Sundkvist. 1979. Acoustic Sounding for Manganese Nodules. NOAA Sea Grant Project Summary, Dept. of Aerospace and Ocean Engineering, Virginia Polytechnic Institute and State University.

Magnuson, A. H., K. Sundkvist, Y. Ma, and K. Smith. 1981. 'Acoustic Sounding for Manganese Nodules,' Submitted to Offshore Technology Conference, May 1981, Houston, TX. Dept. of Aerospace and Ocean Engineering, Virginia Polytechnic Institute and State University.

McFarland, W. D. 1980. Development of a Reliable Method for Resource Evaluation of Deep-Sea Manganese Nodule Deposits Using Bottom Photographs. M.S. Thesis, Department of Geology, Washington State University.

Mizuno, A. and T. Moritani. 1976. 'Manganese Nodule Deposits of the Central Pacific Basin', in World Mining and Metals Tecnology. pp. 267-281.

Moritani, T. and F. Murakami. 1979. 'Relation Between Manganese Nodule Abundance and Acoustic Stratigraphy in the GH77-1 Area', Paper XV, Cruise Report No. 12 'Deep Sea Mineral Resources Investigation in the Central Western Part of Central Pacific Basin', Geological Survey of Japan, Hisamoto, Takatsu-ku, Kawasaki-shi, Japan, pp. 218-221.

Speiss, F. N. 1980. Ocean Remote Acoustic Sensing of the Sea Floor. In Vol. II of NOAA Workshop on Ocean Acoustic Remote Sensing, Chairmen Murphey, S. R. and M. Schulkin. NOAA Office of Sea Grant. Rockville, MD, pp. 11-1; 11-38.